2017

Computational and Experimental Investigations Concerning Rare Gas and DPAL Lasers and a Relaxation Kinetics Investigation of the Br_2 + 2NO = 2BrNO Equilibrium

Joel R. Schmitz
Wright State University

COMPUTATIONAL AND EXPERIMENTAL INVESTIGATIONS CONCERNING RARE GAS AND DPAL LASERS AND A RELAXATION KINETICS INVESTIGATION OF THE $Br_2 + 2NO = 2BrNO$ EQUILIBRIUM

A thesis submitted in partial fulfillment

of the requirements for the degree of

Master of Science

BY

JOEL R. SCHMITZ

B.S., Wright State University, 2014

2017

Wright State University

WRIGHT STATE UNIVERSITY

GRADUATE SCHOOL

April 26, 2017

I HEREBY RECOMMEND THAT THE THESIS PREPARED UNDER MY SUPERVISION BY Joel R. Schmitz ENTITLED COMPUTATIONAL AND EXPERIMENTAL INVESTIGATIONS CONCERNING RARE GAS AND DPAL LASERS AND A RELAXATION KINETICS INVESTIGATION OF THE $Br_2 + 2NO = 2BrNO$ EQUILIBRIUM BE ACCEPTED IN PARTIAL FULFILLMENT OF THE REQUIRMENTS FOR THE DEGREE OF Master of Science.

_____

David A. Dolson, Ph.D.
Thesis Director

_____

David A. Grossie, Ph.D.
Chair, Department of Chemistry

Committee on
Final Examination

_____

David A. Dolson, Ph.D.

_____

Amit Sharma, Ph.D.

_____

Rachel Aga, Ph.D.

_____

Paul Seybold, Ph.D.

_____

Robert E. W. Fyffe, Ph.D.
Vice President for Research and
Dean of Graduate School

ABSTRACT

Schmitz, Joel R. M.S. Department of Chemistry, Wright State University, 2017. *Computational and Experimental Investigations Concerning Rare Gas and DPAL Lasers and a Relaxation Kinetics Investigation of the Br_2 + 2NO = 2BrNO Equilibrium*.

This research contains four different research projects, the first an educational project introducing hydrogen bromide and deuterium bromide (HBr/DBr) and carbon monoxide (CO) as viable options for infrared vibration-rotation spectroscopy at 0.125 cm^{-1} or 0.5 cm^{-1} resolution in the teaching laboratory. The second project involved determining the spectral shifts of lanthanide fibers for diode-pumped alkali laser (DPAL) applications. Spectral shifts of lanthanides were determined using UV-VIS-NIR absorbance spectroscopy and laser-induced fluorescence (LIF). The third project entailed computing Ar* atomic energy levels and the potential energy curves of Ar*+He laser systems arising from $3p^5 4s^1$ and $3p^5 4p^1$ Ar* electronic configurations using *ab initio* theory. The final project of this research determined rate coefficients and the equilibrium constant of the formation of nitrosyl bromide (BrNO) using relaxation kinetics. Integrated solution of the relaxation rate equation and third-order integrated rate law methodologies produced final values of k_f =1.50(6) x 10^{-5} $torr^{-2}s^{-1}$, k_r=5.8(8) x 10^{-5} $torr^{-1}s^{-1}$, and K_{eq} = 0.26(3) $torr^{-1}$, agreeing with literature within uncertainty.

TABLE OF CONTENTS

TABLE OF CONTENTS (Continued)

TABLE OF CONTENTS (Continued)

TABLE OF CONTENTS (Continued)

LIST OF FIGURES

LIST OF FIGURES (Continued)

LIST OF FIGURES (Continued)

LIST OF FIGURES (Continued)

LIST OF TABLES

LIST OF TABLES (Continued)

LIST OF TABLES (Continued)

ACKNOWLEDGMENTS

First and foremost, I would like to acknowledge my advisor Dr. David A. Dolson for all the assistance and support he has given me throughout my Master's work. I truly appreciate and am continually grateful for all his experience and knowledge that he has shared with me. I would also like to thank Dr. Amit Sharma for with giving me the opportunity to work with the Air Force Institute of Technology (AFIT) at Wright Patterson Air Force Base (WPAFB) on rare gas laser systems and I would also like to thank him for the assistance he provided me with the research. I would also like to acknowledge Dr. Greg Pitz and Dr. Tony Hostutler from Kirtland Air Force Base (KAFB) for their knowledge and assistance with the lanthanide fiber lasers project. I would also like to acknowledge Timothy Henthorne at Ohio State University (OSU) for fabricating reaction vessels for the BrNO kinetics experimentation. Finally, I would like to thank my partner Eric for his undying support in my career and for encouraging me every step of the way.

Chapter 1: Expanded Choices for Infrared Vibration-Rotation Spectroscopy in the Teaching Laboratory

1.1 Introduction

I. Vibrational-Rotational Spectroscopy in the Teaching Laboratory

Most undergraduate chemistry majors encounter quantum mechanics and chemical spectroscopy in third-year physical chemistry lecture classes. In the teaching laboratory, quantum mechanics and spectroscopic theory is reinforced through atomic and molecular spectroscopy. With the common introduction of the infrared vibration-rotation spectroscopy of small linear molecules, the harmonic oscillator and rigid rotor models are experientially reinforced to the student.

The first published use of IR vibrational-rotational spectroscopy in a teaching lab seems to be that of F. E. Stafford *et. al.* in 1963[1]. Stafford used a Beckman IR-5 and a Baird AB-2 infrared spectrophotometer at 3.3 μm and a Cary 14 spectrophotometer at 1.7 μm to obtain, respectively, the fundamental (1-0) and first overtone (2-0) band spectra of HCl vapor. While Stafford was able to observe rotational detail, isotopic rotational splitting was only fully resolved in the 2-0 spectrum obtained with the Cary spectrophotometer. Since Stafford, improvements were made in IT grating instruments, FTIR spectrometers were introduced and spectral resolution has increased to 1/8 wavenumber (0.125 cm^{-1}) with recent spectrometers available in some teaching laboratories. Other molecules for study such as HBr/DBr, CO, HCN/DCN, N_2O, C_2H_2/C_2D_2 and CO_2 have been demonstrated in teaching labs [2-10]. HCl, however, has remained the popular choice, due its simple synthesis, simple rotational structure, isotopic

variance, and strong IR absorbance. Various deuteration methods for HCl and HBr have also been proposed[4,11,12].

Various methods have been suggested to analyze the obtained data. Schwenz *et. al.* compared different analysis methods, which include successive and combination differences along with a multiple regression[4]. The conclusion was made that the multiple regression yielded experimental parameter values closer to literature values than did the successive and combination differences method. Iaonne[13] proposed to use multiple linear fits of the spectroscopic data while Joel Tellinghuissen[14] used a global fit of multiple isotopologues.

II. Vibration-Rotation Spectroscopy of a Diatomic

Rovibronic Energy Expression

The classical model of a ball and a spring can be used to illustrate the forces acting upon and the energy of a vibrating molecule [15]. When the bond of the molecule is stretched or compressed, a force *F* acts to restore that bond to equilibrium. This force can be defined as

$$F = -\frac{dV(x)}{dx} = -kx \tag{1}$$

where *V(x)* is the potential energy of the molecule with a dependency on the displacement *x* of the bond and where *k* is the force constant. Integration allows *V*(x) to be defined as

$$V(x) = \frac{1}{2}kx^2 \tag{2}$$

Equation (2) is known as the harmonic oscillator model. Plotting the potential energy as a function of the displacement (which for a molecule can be defined as the difference of the

bond length r and the equilibrium bond length r_e) results in a parabolic function. In this function, all vibrational energy levels, as labeled with the vibrational quantum number v, are equally spaced and the potential energy function increases without limit as the magnitude of the displacement (r-r_e) increases. The energy of a vibrating molecule can then be defined as

$$E_{vib} = h\nu_0 \left(v + \frac{1}{2}\right) \tag{3}$$

where h is Planck's constant and ν_0 is the vibrational frequency, which is defined as

$$\nu_0 = \frac{1}{2\pi}\sqrt{\frac{k}{\mu}} \tag{4}$$

where k is the force constant of the vibrating bond and μ is the reduced mass of the molecule. In order to express the vibrational energy in wavenumbers (cm^{-1}), (3) can be rewritten as

$$\frac{E_{vib}}{hc} = G(v) = \omega_e \left(v + \frac{1}{2}\right) \tag{5}$$

where

$$\omega_e = \nu_0 / c \tag{6}$$

A true molecular potential energy function does not parabolically increase as the displacement increases, as the harmonic oscillator model suggests, but rather rises exponentially at negative displacements and reaches an asymptotic limit at large positive displacements. Also, vibrational energy levels are not equally spaced but rather the spacing between vibrational energy levels decreases as v increases [16]. To account for this

anharmonicity in real molecules, terms with higher dependencies on $\left(v+\frac{1}{2}\right)$ must be included in (5). This results in

$$G(v)=\omega_e\left(v+\frac{1}{2}\right)-\omega_e x_e\left(v+\frac{1}{2}\right)^2+\omega_e y_e\left(v+\frac{1}{2}\right)^3\ldots \tag{7}$$

where ω_e, $\omega_e x_e$, and $\omega_e y_e$ are vibrational parameters with wavenumber (cm^{-1}) units. The negative second term assures that all values of $\omega_e x_e$ will be positive.

If it is to be assumed that the bond between two atoms is fixed length as the molecule rotates about its center of mass, the angular momentum P_J of the molecule can be defined as

$$P_J=\hbar[J(J+1)]^{\frac{1}{2}} \tag{8}$$

where J is the rotational quantum number with a zero or positive integer value. Solving the Schrödinger equation with the rigid rotor Hamiltonian results in a rotational energy of

$$E_{rot}=\frac{h^2}{8\pi^2 I}J(J+1) \tag{9}$$

where I is the moment of inertia of the molecule around a center of mass. For a diatomic molecule, I is defined as the product of the reduced mass μ and the square of the bond length r.

$$I=\mu r^2 \tag{10}$$

The projection of the angular momentum J on the z-axis results in a magnetic quantum number M_J such that

$$-J\leq M_J\leq J \tag{11}$$

resulting in a $2J+1$ degeneracy of rotational energy levels [17].

To determine the rotational energy in wavenumbers, (9) is rewritten as

$$\frac{E_{rot}}{hc} = F(J) = B[J(J+1)] \tag{12}$$

where

$$B = \frac{h}{8\pi^2 cI} = \frac{h}{8\pi^2 c\mu r^2} \tag{13}$$

Equation (13) will result in a wavenumber value for B_v, as long as the speed of light c is reported in cm/s. As in the case of the harmonic oscillator, deviations from the rigid rotor must be taken into account. A major distortion of the rigid rotor model is centrifugal distortion, in which the bond length if not truly rigid but rather elongates as the bond rotation occurs [17]. An additional power term is therefore added to (12) to account for the reduction in rotational energy as the bond elongates..

$$F(J) = B[J(J+1)] - D[J(J+1)]^2 \tag{14}$$

The rotational parameter D is known as the *centrifugal distortion constant*. As with (7), addition terms can be included in (14) if needed, each term increasing in on the exponential order of $[J(J+1)]$ and oscillating in negative/positive signs.

Rotational parameters have a dependence on the vibrational quantum number v and the bond length r. When the molecule occupies higher vibrational states, the value of r increases within that vibration state, giving B and other rotational parameters a dependency on both v and r. Therefore B_v and D_v can be written as

$$B_v = B_e - \alpha_e\left(v+\frac{1}{2}\right) + \gamma_e\left(v+\frac{1}{2}\right)^2 - \cdots \tag{15}$$

$$D_v = D_e - \beta_e \left(v + \frac{1}{2}\right) + \cdots \tag{16}$$

The total vibrational and rotational, or *rovibronic*, energy of the molecule can be defined as the summation of the vibrational energy and the rotational energy.

$$E(v,J) = G(v) + F(J) \tag{17}$$

$$E(v,J) = \omega_e \left(v + \frac{1}{2}\right) - \omega_e x_e \left(v + \frac{1}{2}\right)^2 + \omega_e y_e \left(v + \frac{1}{2}\right)^3 - \cdots$$

$$+ \ [B_e - \alpha_e \left(v + \frac{1}{2}\right) + \gamma_e \left(v + \frac{1}{2}\right)^2][J(J+1)]$$

$$-[D_e - \beta_e \left(v + \frac{1}{2}\right)]\,[J(J+1)]^2 + \cdots \tag{18}$$

Therefore, if the energy of a rovibronic transition is known, along with the vibrational and rotational quantum numbers, the rovibronic parameters can be determined.

Each rovibrational transition results in a vibrational band (v"←v') with a band center v_0. The vibrational band that corresponds to a transition from the v=0 ground state to the first vibration excited state (1←0) is often noted as the *fundamental band* while transitions from the vibrational ground state to higher vibrational levels are noted as *overtones*, with the vibrational transition 2←0 labelled as the *first overtone* [16]. Each vibrational band can be rotational resolved into two branches, the *P* branch and the *R* branch. The *P* branch includes all rotational transitions in which ΔJ = -1 while the *R* branch includes those in which ΔJ = +1. Due to anharmonic behavior, the *P* branch expands at lower frequency as *J* increases and the *R* branch compresses at higher frequency as *J* increases. Molecules with isotopic variance present similar spectra, the difference being an isotopic shift per the reduced mass in (4). When this shift is small,

vibration-rotation lines lie close to one another and lines near the band center have a separation close to the difference in the fundamental vibrational frequencies.

The rovibronic energy can also be expressed as a polynomial function[18] of the variable *m*

$$\nu = \nu_0 + (B_v' + B_v")m + (B_v' - B_v")m^2 - 2(D_v' + D_v")m^3 - (D_v' - D_v")m^4 \qquad (19)$$

where $m = J + 1$ for the *R* branch and $m = J - 1$ for the *P* branch. Parameters for the upper vibrational state have a single prime notation while the parameters of the lower vibrational state have a double prime notation. The rotational parameters B_v and D_v of both the upper and lower vibrational states can be determined from a fourth-order polynomial fit of ν vs. *m*. The fourth-order term can often be excluded if the resolution is insufficient to resolve the effects of the small differences in D_v' and D_v'' and (19) can be reduced to a cubic equation. The third term can further be simplified to $-4D_v$, assuming that $D_v' \approx D_v''$. The need to include a fourth-order term in (19) is determined experimentally by a plot of the residuals (cm^{-1}) vs. *m*. If the residuals of the cubic fit have no functionality, then a cubic fit to the data suffices and a fourth-order term is not needed.

Dunham Coefficients

In order to simply the expression for rovibronic energy of molecule, Dunham rewrote the energy equation in the following form[19]

$$E(v,J) = \sum_{lm} Y_{lm}\left(v + \frac{1}{2}\right)^l [J(J+1)]^m \qquad (20)$$

where Y_{lm} is now called a Dunham coefficient with an *l* power dependency for $\left(v + \frac{1}{2}\right)$ and an *m* dependency for $[J(J+1)]$. Table 1.1.1 shows previously derived rovibronic

energy parameters with their corresponding Dunham coefficients. Whereas Eqs. (7) and (14-15) have alternating signs for successive terms, the Dunham coefficients carry positive signs in Eq. (20).

Table 1.1.1 Rovibronic energy parameters with corresponding Dunham coefficients.

Parameter	Dunham Coefficient
ω_e	Y_{10}
$\omega_e x_e$	$-Y_{20}$
$\omega_e y_e$	Y_{30}
B_e	Y_{01}
α_e	$-Y_{11}$
γ_e	Y_{21}
D_e	$-Y_{02}$
β_e	Y_{12}

Equation (20) allows determination of energy parameters for a single isotopic species. Dunham coefficients for different isotopes can be related to their respective reduced mass μ as the following

$$\left(\frac{Y_{lm}^*}{Y_{lm}}\right) = \left(\frac{\mu}{\mu^*}\right)^{m+\frac{l}{2}} \tag{21}$$

where the asterisk refers to a single isotope. Equation (20) can then be rewritten as

$$E^{\alpha}(v,J) = \sum_{lm}\left(\frac{\mu}{\mu_\alpha}\right)^{m+\frac{l}{2}} Y_{lm}\left(v+\frac{1}{2}\right)^l [J(J+1)]^m \tag{22}$$

where the α notation refers to the standard *isotope*. Typically, the most naturally abundant isotope is used as the standard isotope.

III. Purpose

Typically, HCl is the standard molecule for third-year chemistry teaching laboratories when performing infrared vibrational-rotation spectroscopy of a heteronuclear diatomic. This research shows that HBr/DBr and CO are other viable choices, where students can see typical *P* and *R* branch rotational structure within vibrational bands along with isotopic variance. Infrared scans will be collected at varying spectroscopic resolution in order to determine if these molecules may be used in teaching laboratories having instrumentation with lower spectral resolution than 0.125 cm^{-1}.

1.2 Experimental

I. HBr/DBr Synthesis

HBr and DBr were synthesized in a fume hood by reacting a halide salt with sulfuric or d_2-sulfuric acid, respectively.

$$NaBr(s) + H_2SO_4(l) = HBr(g) + NaHSO_4(s) \quad (23)$$

$$NaBr(s) + D_2SO_4(l) = DBr(g) + NaHSO_4(s) \quad (24)$$

In generating 0.5L of the desired gas, an Erlenmeyer flask was filled with sodium bromide (NaBr, 2.15g, 21.0 mmol), which was then reacted with either sulfuric acid or d_2-sulfuric acid in excess (3-5 mL). The flask was stoppered while allowing the generated gas to flow through glass and Tygon® tubing into a set of two spectroscopic cells in series: a longer cell (22 cm) made of PVC pipe with sapphire (Al_2O_3) windows and a shorter glass cell (15 cm) with salt (KBr) windows. As sulfuric acid can act as an oxidizing agent, some bromine (Br_2) gas was generated in the synthesis. The reaction was relatively quick, as gas generation subsided after a couple minutes. After enough gas was generated and collected, gases were dispersed from the flask by removing the stopper and allowing it to remain in the hood. The solution was then neutralized with sodium bicarbonate ($NaHCO_3$).

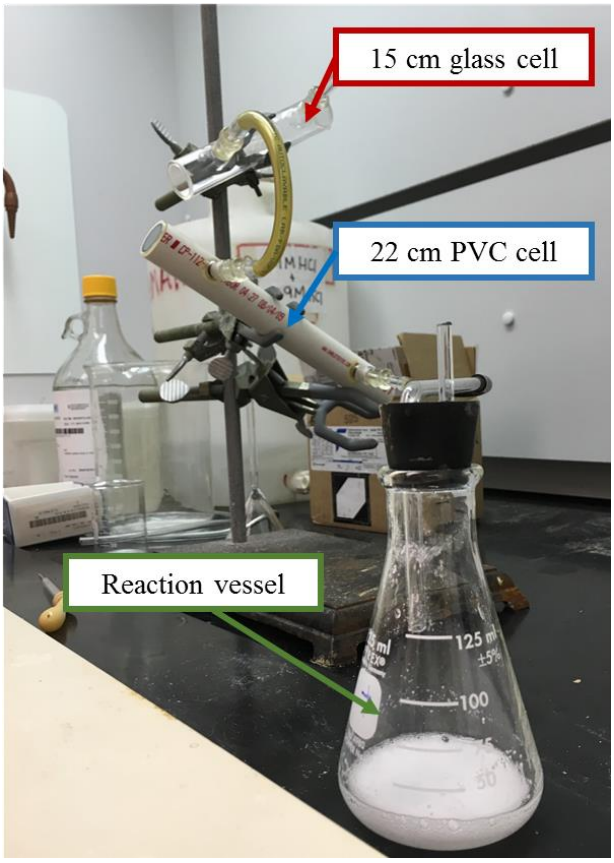

Figure 1.2.1 Experimental set up of HBr/DBr and CO synthesis.

II. CO Synthesis

Carbon monoxide (CO) was synthesized by reacting sodium formate (NaCOOH) with sulfuric acid (H_2SO_4).

$$NaCOOH(s) + H_2SO_4(l) = CO(g) + H_2O(g) + NaHSO_4(s) \quad (25)$$

The desired 0.5 L of CO was generated by reacting formic acid (21.0 mmol) in the apparatus in Figure 1.2.1 with sulfur acid in excess (3-5 mL). The generated CO gas, as with the HBr/DBr gas, was allowed to flow into a series of cells: a longer PVC cell (22 cm) with sapphire windows and a shorter glass cell (15 cm) with salt (KBr) windows. Gas generation was observed for five-ten minutes. It should be noted that there were

obstructions to gas flow in the path from the flask to the cells in either the HBr/DBr or CO synthesis. The path was ensured to be open by passing nitrogen (N_2) through the tubing at a low positive pressure.

III. Collection of the Data

Once the cells were filled with the desired gas, they were placed independently in a model iS-50 Nicolet Fourier Transform Infrared (FTIR) spectrometer. The frequency range scanned for HBr/DBR and CO was 1600-5200 cm^{-1}. For HBr/DBr, 32 scans at 0.25 and 0.125 cm^{-1} were obtained while for CO, 32 scans at 1.00, 0.50, 0.25, and 0.125 cm^{-1} were obtained. For all scans Boxcar apodization and two level filling were chosen. Table 1.2.1 shows the point separation in the various instrumental resolutions with two level filling.

Table 1.2.1 Wavenumber per point with two level filling at various resolution.

Resolution (cm^{-1})	Point Separation (cm^{-1})
0.125	0.015
0.25	0.030
0.50	0.060
1.00	0.120

The first overtones of the gases were observable using the long cell but in order to obtain the fundamental bands on scale, some gas was shaken out of the short cell.

IV. Data Analysis

Peaks corresponding to rotational transitions within the vibrational fundamental and overtone bands were picked with Origin® software and their frequency values were

recorded along with their respective v', v'', J', J'', and m values. Cubic and quartic fits were applied to separate isotopic bands and the average and maximum absolute residuals were determined, in order to note if a quartic fit improved the average and absolute maximum residuals. Measured line positions were then fit to ΔE energy differences using a non-linear regression tool in SigmaPlot®, allowing determination of the Dunham coefficients for the standard isotope ($H^{81}Br$ for HBr/DBr and for ^{12}CO).

1.3 Results

I. HBr/DBr Results

Figures 1.3.1 and 1.3.2 show the acquired infrared spectra of the scaled fundamental and first overtone band of HBr at a spectral resolution of 0.125 cm^{-1}. In order to determine accurate frequencies for line positions with low *J* values of the fundamental band, the pressure of gas in the short glass cell was adjusted in order to put the line positions with low *J* values on scale while the longer cell with a higher gas pressure was used to pick line positions with high *J* values of the fundamental and all lines in the overtone. A total of fifteen line positions in the *P* branch and sixteen line positions in the R branch were observed in the fundamental band of HBr and 11 line positions in both the *P* and *R* branches were observed in the overtone band. In Figure 1.3.1, splitting of the $H^{79}Br/H^{81}Br$ lines is not observed due to the small separation of the lines.

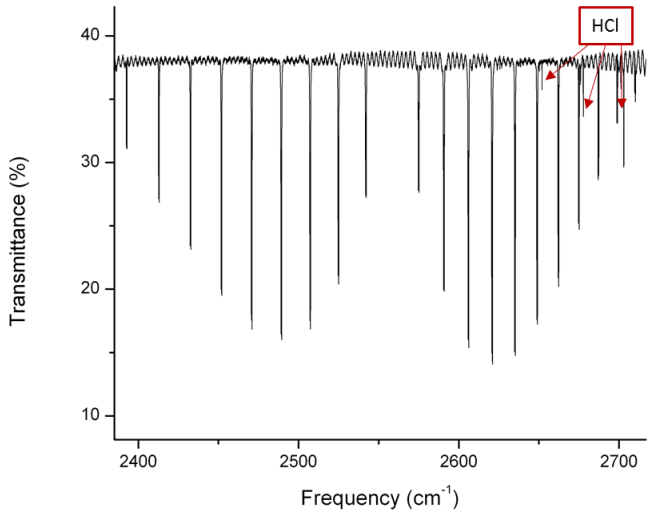

Figure 1.3.1 Scaled fundamental band of HBr.

The far end of the *P* branch of HCl is able to be seen in Figure 3.1 due to the presence of HCl in the reaction mixture. When HBr is synthesized, HCl is inevitably formed in the reaction process from chloride salt impurities.

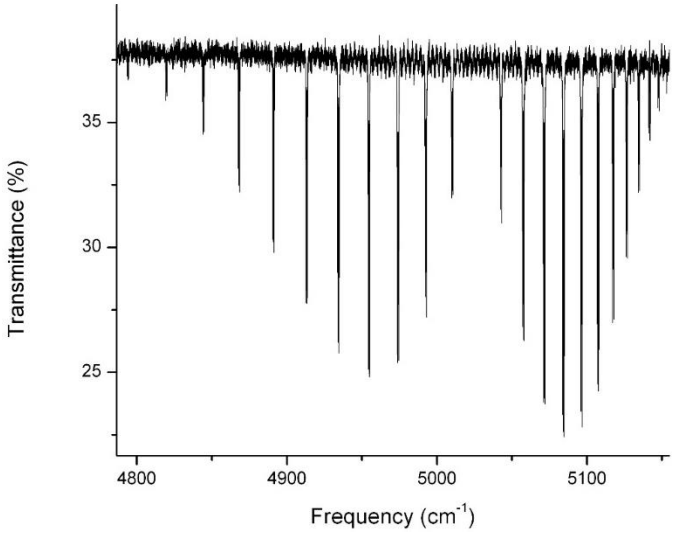

Figure 1.3.2 First overtone band of HBr.

The respective expansion and compression of the *P* and *R* branch lines is more easily noted in the overtone band (because the difference between B' and B" is greater than in the fundamental) and can be seen in Figure 1.3.2. Scans were taken at different spectroscopic resolution in order to observe the isotopic splitting at different resolutions. Figure 1.3.3 shows the isotopic splitting of the R(1) line of HBr at 0.25 cm^{-1} and 0.125 cm^{-1} resolution.

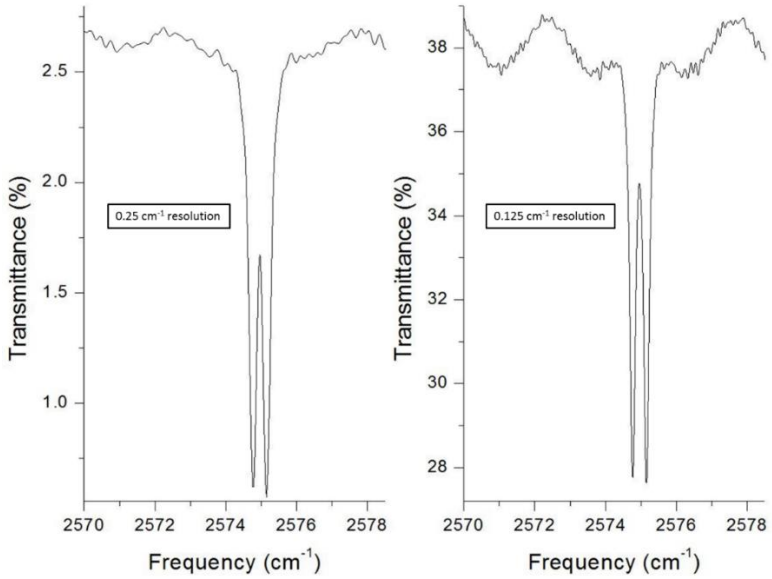

Figure 1.3.3 R(1) line of the HBr fundamental at 0.25 cm^{-1} and 0.125 cm^{-1} spectral resolutions.

Figure 1.3.4 shows the fundamental band of DBr. There is notable interference from vibration-rotation lines of the water bending mode; however, only a few DBr line positions are compromised.

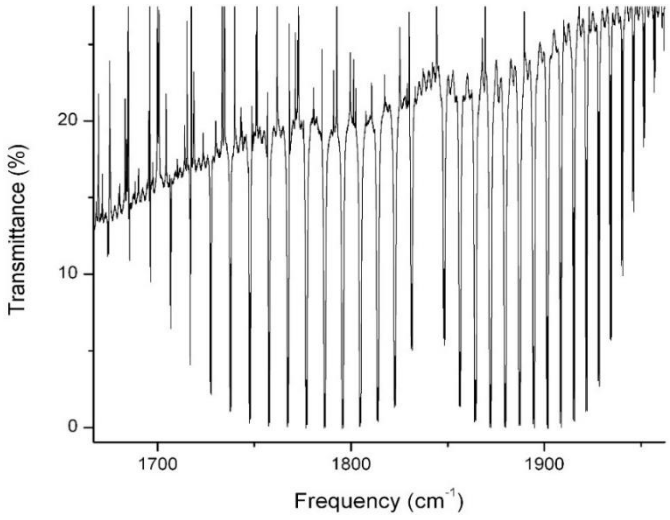

Figure 1.3.4 Fundamental band of DBr with some interference from water bending mode lines.

Below is presented the overtone band of DBr. Interference from the a_1 symmetric stretch of water is observed, increasing the difficulty in measuring line positions in both branches but particularly in the *R* branch. While lines positions for ten J values were determined for the *P* branch, only five were able to be determined for the *R* branch.

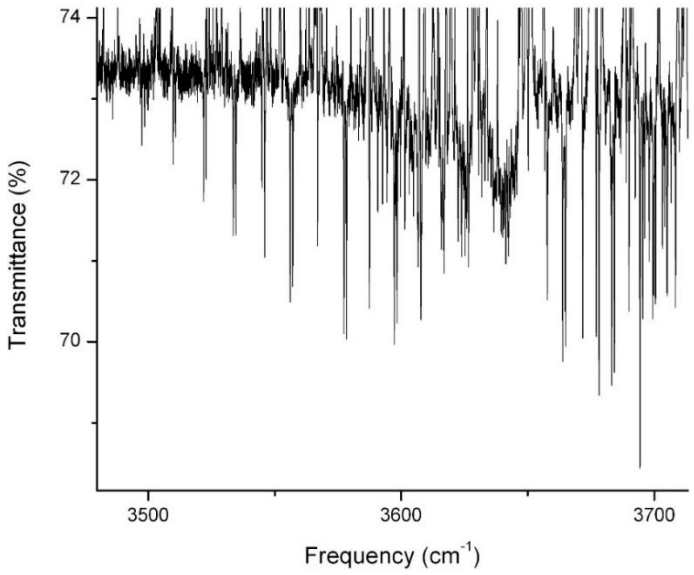

Figure 1.3.5 First overtone band of DBr with interference from water stretching mode lines.

After the frequencies of the rovibronic transitions of the fundamental and overtone branches of HBr/DBr were determined, separate cubic and quartic fits of *v* vs. *m* of each isotopic band were executed and the average and absolute maximum residuals were calculated. A decrease in the average and absolute maximum residuals from the cubic fit to the quartic fit were observed in all the isotopic bands, except for the overtone bands of $D^{81}Br$ and $D^{79}Br$. While an increase of the average residuals from the cubic to quartic fit for the $D^{81}Br$ and $D^{79}Br$ overtone was observed, the maximum absolute residual still decreased from the cubic to quartic fit.

Table 1.3.1 Average and maximum residuals of the cubic and quartic polynomial fits of HBr/DBr vibration-rotation line positions.

Polynomial Fit	Isotopic Band	Average Residual (cm^{-1})	Maximum Residual (cm^{-1})
Cubic	$H^{79}Br$ (1←0)	0.014	0.032
	$H^{81}Br$ (1←0)	0.013	0.037
	$H^{79}Br$ (2←0)	0.007	0.020
	$H^{81}Br$ (2←0)	0.011	0.030
	$D^{79}Br$ (1←0)	0.008	0.027
	$D^{81}Br$ (1←0)	0.008	0.022
	$D^{79}Br$ (2←0)	0.013	0.034
	$D^{81}Br$ (2←0)	0.018	0.043
Quartic	$H^{79}Br$ (1←0)	0.010	0.032
	$H^{81}Br$ (1←0)	0.007	0.026
	$H^{79}Br$ (2←0)	0.006	0.016
	$H^{81}Br$ (2←0)	0.007	0.013
	$D^{79}Br$ (1←0)	0.004	0.013
	$D^{81}Br$ (1←0)	0.005	0.019
	$D^{79}Br$ (2←0)	0.014	0.032
	$D^{81}Br$ (2←0)	0.018	0.038

Using a non-linear regression, the Dunham Coefficients of $H^{81}Br$ were determined from line positions in six of the vibrational bands, omitting the two DBr overtone bands. The code used for the regression was based on (22) and can be found in Appendix A along with frequencies and appropriate quantum numbers of line positions. Table 1.3.2 shows the results of the non-linear regression and the literature values of the determined Dunham coefficients. The peak values from the DBr overtone were not used in the non-linear regression, as values for the Dunham coefficients were closer to literature values with the exclusion of the DBr overtone data. The determined parameters from fits excluding both the DBr fundamental and overtone, excluding only the DBr overtone, and including both the DBr fundamental and overtone can be viewed in

Appendix A. The average and maximum results of the non-linear regression were 0.0085 cm^{-1} and 0.0410 cm^{-1}, respectively. Errors reported in Table 1.3.2 are one standard deviation of the parameter as determined by the non-linear regression.

Table 1.3.2 Dunham coefficients of $H^{81}Br$, determined by the non-linear regression.

Dunham Coefficient	**Parameter**	**Value (cm^{-1})**	**Literature Value (cm^{-1})**[20]
Y_{10}	ω_e	2649.39(2)	2649.3698(88)
$-Y_{20}$	$\omega_e x_e$	45.55(1)	45.5795(70)
Y_{01}	B_e	8.4643(1)	8.464877(37)
$-Y_{11}$	α_e	0.23257(8)	0.233254(88)
$-Y_{02}$	D_e	$3.434(5) \times 10^{-4}$	$3.4579(18) \times 10^{-4}$
Y_{12}	β_e	$3.4(2) \times 10^{-6}$	$3.99 (24) \times 10^{-6}$

Students in a third-year laboratory course should be successfully determine the rovibration constants of $H^{81}Br$ through FTIR spectra, even if 0.125 cm^{-1} resolution is not available them. Even 0.25 cm^{-1} spectra resolution is sufficient to resolve isotopic splitting in HBr and DBr infrared transitions. Prior to 2010 WSU students were able to obtain vibration-rotation spectra with a best resolution of 0.5 cm^{-1}. This was not sufficient to resolve the bromine isotopes of HBr/DBr; however, 1-0 and 2-0 spectra were obtained and spectroscopic constants from regression analyses were compared to literature $H^{81}Br$ constants.

II. CO Results

Figure 1.3.6 below presents the spectrum of the fundamental band of ^{12}CO at a spectral resolution of 0.125 cm^{-1}. The lines are free from interference and readily assigned by students.

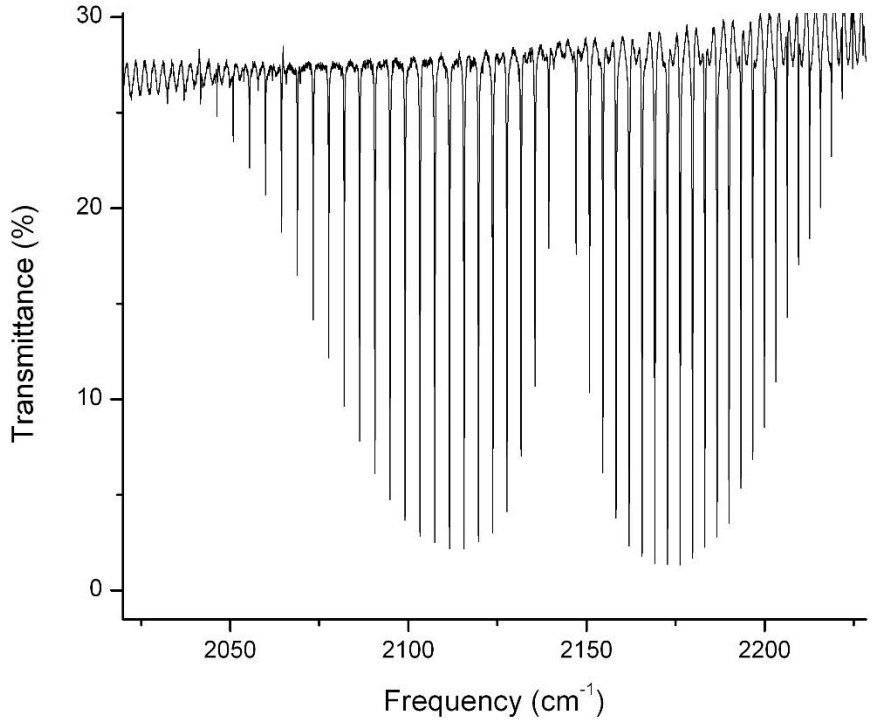

Figure 1.3.6 Fundamental band of ^{12}CO.

Overexposure of the ^{12}CO spectrum results in observable ^{13}CO transitions, although many others are overlapped by ^{12}CO transitions, limiting the number of determinable ^{13}CO frequencies. Only fifteen line positions in the *P* branch of ^{13}CO were able to be determined, along with eight line positions in the *R* branch. Some of the peak assignments were determined with the assistance of Guelachvili and Rao[21].

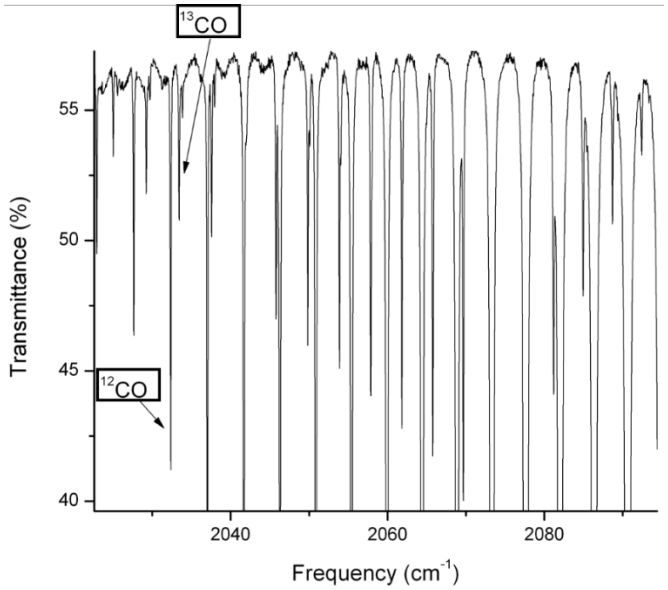

Figure 1.3.7. Some of ^{13}CO lines the fundamental band of ^{12}CO.

While the ^{12}CO overtone was observed in Figure 1.3.8 below, ^{13}CO overtone lines were not able to be observed, due to insufficient sample path length and instrumental sensitivity. Line positions of the three ^{12}CO/^{13}CO bands are presented in Appendix A.

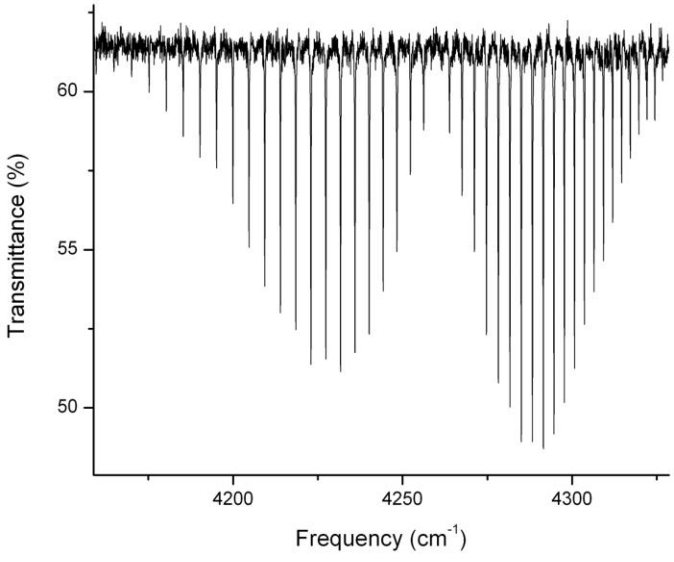

Figure 1.3.8 First overtone band of ^{12}CO.

As with the HBr/DBr data, cubic and quartic fits of *v* vs. *m* of the three individual bands were performed and in all cases, the average residual decreased from the cubic fit to the quartic fit. In the case of the ^{12}CO overtone data, the quartic fit increased the maximum residual, but only by 4.8%. The ^{12}CO and ^{13}CO fundamental fits saw a decrease in the maximum residual, as expected.

Table 1.3.3 Average and maximum residuals from cubic and quartic fits of ^{12}CO and ^{13}CO bands.

Band	Fit	Average Residual (cm^{-1})	Maximum Residual (cm^{-1})
^{12}CO v(1-0)	Cubic	3.3596×10^{-3}	0.0161
	Quartic	3.3298×10^{-3}	0.0150
^{12}CO v(2-0)	Cubic	$7.5052 \times 10^{-3-}$	0.0228
	Quartic	7.2725×10^{-3}	0.0239
^{13}CO v(1-0)	Cubic	0.0259	0.0649
	Quartic	0.0258	0.0612

The same non-linear regression in SigmaPlot® was applied to the ^{12}CO and ^{13}CO data, determining the Dunham coefficients of the ^{12}CO isotope and comparing them to literature values. The average and maximum residuals were 0.009 cm^{-1} and 0.066 cm^{-1}, respectively. A non-linear regression also was performed on solely the data from the ^{12}CO fundamental and overtone bands and the resulting Dunham coefficients are located in Appendix A.

Table 1.3.4 Dunham coefficients for ^{12}CO obtained from the 1-0 and 2-0 bands of ^{12}CO and the 1-0 band of ^{13}CO.

Dunham Coefficient	Parameter	Value (cm^{-1})	Literature Value (cm^{-1})[22]
Y_{10}	ω_e	2169.745(5)	2169.812670(13)
$-Y_{20}$	$\omega_e x_e$	13.237(2)	13.28787634(774)
Y_{01}	B_e	1.93134(7)	1.931280985(18)
$-Y_{11}$	α_e	$1.7505(3) \times 10^{-2}$	$1.75043923(130) \times 10^{-2}$
$-Y_{02}$	D_e	$6.14(5) \times 10^{-6}$	$6.121615183(892) \times 10^{-6}$

The results shown suggest that CO is also a viable choice for infrared rovibronic spectroscopy of a diatomic molecule. Isotopic variance is able to be seen in the fundamental band but students may need assistance with assigning a few ^{13}CO lines, if those line positions are not supplied. Though observation of the ^{13}CO lines may suffer, the ^{12}CO line positions in both bands may be determined from much lower resolution spectra from 1600-5200 cm^{-1} because adjacent line separations are greater than 3.5 cm^{-1} for the low J lines.

1.4 References

1. Stafford, F. E.; Holt, C. W.; Paulson, G. L. Vibration-rotation spectrum of HCl. Physical chemistry experiment. *J. Chem. Educ.* **1963**, *40*, 245-9.

2. Rieck, D. F.; Kundell, F. A.; Clements, P. J. The generation of heteronuclear diatomic gases for determination of rotational spectra. A variation of a classic physical chemistry experiment. *J. Chem. Educ.* **1989**, *66*, 682.

3. Mina-Camilde, N.; Manzanares I., C.; Caballero, J. F. Molecular constants of carbon monoxide at v = 0, 1, 2, and 3: a vibrational spectroscopy experiment in physical chemistry. *J. Chem. Educ.* **1996**, *73*, 804-807.

4. Schwenz, R. W.; Polik, W. F. Analysis of the infrared spectra of diatomic molecules. *J. Chem. Educ.* **1999**, *76*, 1302-1307.

5. Keedy, C. R. The Rotation-Vibration Spectra of HCN and DCN. *J. Chem. Educ.* **1992**, *69*, A296.

6. Little, R. Molecular Structure and Thermodynamic Properties of HCN and DCN. *J. Chem. Educ.* **1966**, *43*, 2.

7. Bryant, M.; Reeve, S. W.; Burns, W. A. Observation of Analysis of N_2O Rotation-Vibration Spectra. *J. Chem. Educ.* **2008**, *85*, 121.

8. Richards, L. W. The Infrared Spectra of C_2H_2 and C_2D_2. *J. Chem. Educ.* **1966**, *43*, 644.

9. Castle, K. J. High Resolution Vibration-Rotation Spectroscopy of CO_2: Understanding the Boltzmann Distribution. *J. Chem. Educ.* **2007**, *84*, 459.

10. Dolson, D. A.; Anders, C. B. FTIR vibration-rotation spectrum and analysis of the $^{13}CO_2$ asymmetric stretch fundamental band. *Chem. Educator* **2015**, *20*, 53-59.

11. Ganapathisubramanian, N. Vibrational-rotational spectra: simultaneous generation of HCl, DCl, HBr and DBr. *J. Chem. Educ.* **1993**, *70*, 1035.

12. Lehmann, E. L.; Sabadini, E. Roto-Vibrational Spectroscopy: A Hint for DCl Generation. *J. Chem. Educ.* **2010**, *87*, 1402.

13. Iannone, M. Using Excel Solver: An Addendum to the HCl Infrared Spectrum Experiment. *J. Chem. Educ.* **1998**, *75*, 1188.

14. Tellinghuisen, J. Global least-squares analysis of the IR rotation-vibration spectrum of HCl. *J. Chem. Educ.* **2005**, *82*, 150-156.

15. Hollas, J. M. *Modern Spectroscopy;* John Wiley & Sons, Inc.: West Sussex, 2004; , pp 452.

16. Bernath, P. F. *Spectra of Atoms and Molecules;* Oxford University Press, Inc.: New York, 1995; .

17. Steinfeld, J. I. Rotation and Vibration of Diatomic Molecules. In *Molecules and Radiation: An Introduction To Modern Molecular Spectroscopy*; Woods, J. A., Wernick, L., Eds.; Harper & Row, Publishers, Inc.: New York, 1974; pp 92.

18. Herzberg, G. Interpretation of the Finer Details of Infrared and Raman Spectra. In *Molecular Spectra and Molecular Structure: I. Spectra of Diatomic Molecules*D. Van Nostrand Company, Inc.: Princeton, 1950; pp 90.

19. Dunham, J. L. The Energy Levels of a Rotating Vibrator. *Phys. Rev.* **1932**, *41*, 721.

20. Stocker, R. N.; Goldman, A. Infrared Spectral Line Parameters of HBr and DBr at Elevated Temperatures. *J. Quant. Spectrosc. and Radiat. Transfer* **1976**, *66*, 335.

21. Guelachvili, G.; Rao, K. R. Spectral Maps, Wavenumber Tables, and Transition Assignments: CO. In *Handbook of Infrared Standards With Spectral Maps and Tranistion Assignments between 3 and 2600 μm;* Academic Press, Inc.: London, pp 504-505, 534.

22. Farrenq, R.; Guelachvili, G.; Sauval, A. J.; Grevesse, N.; Farmer, C. B. Improved Dunham coefficients for carbon monoxide from infrared solar lines of high rotational excitation. *J. Mol. Spectrosc.* **1991**, *149*, 375-90.

Appendix A

A.1 Reduced mass values used in non-linear regressions.

Isotope	μ (amu)
$H^{79}Br$	0.995116912
$H^{81}Br$	0.995426835
$D^{79}Br$	1.963978415
$D^{81}Br$	1.965185984
^{12}CO	6.856208638
^{13}CO	7.17241250221

A.2. Observed line positions of HBr/DBr transitions, along with the appropriate parameters used to complete the non-linear regression in SigmaPlot®. While only four significant figures for the reduced mass are shown, values were expressed to the number of significant figures shown in **A.1**.

P(J")/R(J")	ν (cm^{-1})	m	J'	J"	v'	μ (amu)	Isotopomer
P(15)	2264.1320	-15	14	15	1	0.9954	H81Br
P(14)	2286.4300	-14	13	14	1	0.9954	H81Br
P(13)	2308.3820	-13	12	13	1	0.9954	H81Br
P(12)	2329.9870	-12	11	12	1	0.9954	H81Br
P(11)	2351.2160	-11	10	11	1	0.9954	H81Br
P(10)	2372.0830	-10	9	10	1	0.9954	H81Br
P(9)	2392.5805	-9	8	9	1	0.9954	H81Br
P(8)	2412.6860	-8	7	8	1	0.9954	H81Br
P(7)	2432.3930	-7	6	7	1	0.9954	H81Br
P(6)	2451.6855	-6	5	6	1	0.9954	H81Br
P(5)	2470.5640	-5	4	5	1	0.9954	H81Br
P(4)	2489.0355	-4	3	4	1	0.9954	H81Br
P(3)	2507.0700	-3	2	3	1	0.9954	H81Br
P(2)	2524.6600	-2	1	2	1	0.9954	H81Br
P(1)	2541.8430	-1	0	1	1	0.9954	H81Br

R(0)	2574.7710	1	1	0	1	0.9954	H81Br
R(1)	2590.4850	2	2	1	1	0.9954	H81Br
R(2)	2605.8150	3	3	2	1	0.9954	H81Br
R(3)	2620.5950	4	4	3	1	0.9954	H81Br
R(4)	2634.8630	5	5	4	1	0.9954	H81Br
R(5)	2648.6710	6	6	5	1	0.9954	H81Br
R(6)	2661.9525	7	7	6	1	0.9954	H81Br
R(7)	2674.7210	8	8	7	1	0.9954	H81Br
R(8)	2686.9550	9	9	8	1	0.9954	H81Br
R(9)	2698.6610	10	10	9	1	0.9954	H81Br
R(10)	2709.8185	11	11	10	1	0.9954	H81Br
R(11)	2720.4320	12	12	11	1	0.9954	H81Br
R(12)	2730.4820	13	13	12	1	0.9954	H81Br
R(13)	2739.9730	14	14	13	1	0.9954	H81Br
R(14)	2748.8930	15	15	14	1	0.9954	H81Br
R(15)	2757.2400	16	16	15	1	0.9954	H81Br
P(11)	4793.9305	-11	10	11	2	0.9954	H81Br
P(10)	4819.3780	-10	9	10	2	0.9954	H81Br
P(9)	4844.0260	-9	8	9	2	0.9954	H81Br
P(8)	4867.8010	-8	7	8	2	0.9954	H81Br
P(7)	4890.7470	-7	6	7	2	0.9954	H81Br
P(6)	4912.8340	-6	5	6	2	0.9954	H81Br
P(5)	4934.0180	-5	4	5	2	0.9954	H81Br
P(4)	4954.3530	-4	3	4	2	0.9954	H81Br
P(3)	4973.7630	-3	2	3	2	0.9954	H81Br
P(2)	4992.3100	-2	1	2	2	0.9954	H81Br
P(1)	5009.9070	-1	0	1	2	0.9954	H81Br
R(0)	5042.3985	1	1	0	2	0.9954	H81Br
R(1)	5057.2160	2	2	1	2	0.9954	H81Br
R(2)	5071.1070	3	3	2	2	0.9954	H81Br
R(3)	5084.0490	4	4	3	2	0.9954	H81Br
R(4)	5096.0270	5	5	4	2	0.9954	H81Br
R(5)	5107.0560	6	6	5	2	0.9954	H81Br
R(6)	5117.0900	7	7	6	2	0.9954	H81Br
R(7)	5126.1600	8	8	7	2	0.9954	H81Br
R(8)	5134.2350	9	9	8	2	0.9954	H81Br
R(9)	5141.3010	10	10	9	2	0.9954	H81Br
R(10)	5147.3880	11	11	10	2	0.9954	H81Br
P(15)	2264.4180	-15	14	15	1	0.9951	H79Br
P(14)	2286.7170	-14	13	14	1	0.9951	H79Br
P(13)	2308.6830	-13	12	13	1	0.9951	H79Br
P(12)	2330.2880	-12	11	12	1	0.9951	H79Br
P(11)	2351.5320	-11	10	11	1	0.9951	H79Br
P(10)	2372.3990	-10	9	10	1	0.9951	H79Br
P(9)	2392.9115	-9	8	9	1	0.9951	H79Br

P(8)	2413.0180	-8	7	8	1	0.9951	H79Br
P(7)	2432.7400	-7	6	7	1	0.9951	H79Br
P(6)	2452.0400	-6	5	6	1	0.9951	H79Br
P(5)	2470.9180	-5	4	5	1	0.9951	H79Br
P(4)	2489.4040	-4	3	4	1	0.9951	H79Br
P(3)	2507.4165	-3	2	3	1	0.9951	H79Br
P(2)	2525.0520	-2	1	2	1	0.9951	H79Br
P(1)	2542.2120	-1	0	1	1	0.9951	H79Br
R(0)	2575.1470	1	1	0	1	0.9951	H79Br
R(1)	2590.8920	2	2	1	1	0.9951	H79Br
R(2)	2606.1540	3	3	2	1	0.9951	H79Br
R(3)	2620.9640	4	4	3	1	0.9951	H79Br
R(4)	2635.2470	5	5	4	1	0.9951	H79Br
R(5)	2649.1080	6	6	5	1	0.9951	H79Br
R(6)	2662.3660	7	7	6	1	0.9951	H79Br
R(7)	2675.1430	8	8	7	1	0.9951	H79Br
R(8)	2687.3770	9	9	8	1	0.9951	H79Br
R(9)	2699.0830	10	10	9	1	0.9951	H79Br
R(10)	2710.2480	11	11	10	1	0.9951	H79Br
R(11)	2720.8540	12	12	11	1	0.9951	H79Br
R(12)	2730.9040	13	13	12	1	0.9951	H79Br
R(13)	2740.3950	14	14	13	1	0.9951	H79Br
R(14)	2749.3300	15	15	14	1	0.9951	H79Br
R(15)	2757.6770	16	16	15	1	0.9951	H79Br
P(11)	4794.5180	-11	10	11	2	0.9951	H79Br
P(10)	4820.0410	-10	9	10	2	0.9951	H79Br
P(9)	4844.6890	-9	8	9	2	0.9951	H79Br
P(8)	4868.4940	-8	7	8	2	0.9951	H79Br
P(7)	4891.4560	-7	6	7	2	0.9951	H79Br
P(6)	4913.5280	-6	5	6	2	0.9951	H79Br
P(5)	4934.7410	-5	4	5	2	0.9951	H79Br
P(4)	4955.0585	-4	3	4	2	0.9951	H79Br
P(3)	4974.5010	-3	2	3	2	0.9951	H79Br
P(2)	4993.0180	-2	1	2	2	0.9951	H79Br
P(1)	5010.6300	-1	0	1	2	0.9951	H79Br
R(0)	5043.1140	1	1	0	2	0.9951	H79Br
R(1)	5057.9540	2	2	1	2	0.9951	H79Br
R(2)	5071.8600	3	3	2	2	0.9951	H79Br
R(3)	5084.8020	4	4	3	2	0.9951	H79Br
R(4)	5096.7800	5	5	4	2	0.9951	H79Br
R(5)	5107.8090	6	6	5	2	0.9951	H79Br
R(6)	5117.8505	7	7	6	2	0.9951	H79Br
R(7)	5126.9280	8	8	7	2	0.9951	H79Br
R(8)	5134.9890	9	9	8	2	0.9951	H79Br
R(9)	5142.1000	10	10	9	2	0.9951	H79Br

R(10)	5148.1720	11	11	10	2	0.9951	H79Br
P(20)	1641.2430	-20	19	20	1	1.9640	D79Br
P(18)	1663.6310	-18	17	18	1	1.9640	D79Br
P(17)	1674.6450	-17	16	17	1	1.9640	D79Br
P(16)	1685.5230	-16	15	16	1	1.9640	D79Br
P(15)	1696.2800	-15	14	15	1	1.9640	D79Br
P(14)	1706.8870	-14	13	14	1	1.9640	D79Br
P(13)	1717.3580	-13	12	13	1	1.9640	D79Br
P(12)	1727.6940	-12	11	12	1	1.9640	D79Br
P(11)	1737.8940	-11	10	11	1	1.9640	D79Br
P(10)	1747.9420	-10	9	10	1	1.9640	D79Br
P(9)	1757.8560	-9	8	9	1	1.9640	D79Br
P(8)	1767.6040	-8	7	8	1	1.9640	D79Br
P(7)	1777.2160	-7	6	7	1	1.9640	D79Br
P(6)	1786.6780	-6	5	6	1	1.9640	D79Br
P(5)	1795.9890	-5	4	5	1	1.9640	D79Br
P(4)	1805.1190	-4	3	4	1	1.9640	D79Br
P(3)	1814.0990	-3	2	3	1	1.9640	D79Br
P(2)	1822.9280	-2	1	2	1	1.9640	D79Br
P(1)	1831.5910	-1	0	1	1	1.9640	D79Br
R(0)	1848.4210	1	1	0	1	1.9640	D79Br
R(1)	1856.5870	2	2	1	1	1.9640	D79Br
R(2)	1864.5560	3	3	2	1	1.9640	D79Br
R(3)	1872.3910	4	4	3	1	1.9640	D79Br
R(4)	1880.0215	5	5	4	1	1.9640	D79Br
R(5)	1887.4720	6	6	5	1	1.9640	D79Br
R(6)	1894.7490	7	7	6	1	1.9640	D79Br
R(7)	1901.8600	8	8	7	1	1.9640	D79Br
R(8)	1908.7610	9	9	8	1	1.9640	D79Br
R(9)	1915.4950	10	10	9	1	1.9640	D79Br
R(10)	1922.0340	11	11	10	1	1.9640	D79Br
R(11)	1928.3780	12	12	11	1	1.9640	D79Br
R(12)	1934.5400	13	13	12	1	1.9640	D79Br
R(13)	1940.5060	14	14	13	1	1.9640	D79Br
R(14)	1946.2770	15	15	14	1	1.9640	D79Br
R(15)	1951.8510	16	16	15	1	1.9640	D79Br
R(16)	1957.2150	17	17	16	1	1.9640	D79Br
R(17)	1962.3830	18	18	17	1	1.9640	D79Br
R(18)	1967.3550	19	19	18	1	1.9640	D79Br
R(19)	1972.1160	20	20	19	1	1.9640	D79Br
R(20)	1976.6810	21	21	20	1	1.9640	D79Br
P(20)	1640.8060	-20	19	20	1	1.9652	D81Br
P(18)	1663.1940	-18	17	18	1	1.9652	D81Br
P(17)	1674.1930	-17	16	17	1	1.9652	D81Br
P(16)	1685.0860	-16	15	16	1	1.9652	D81Br

P(15)	1695.7980	-15	14	15	1	1.9652	D81Br
P(14)	1706.4200	-14	13	14	1	1.9652	D81Br
P(13)	1716.8910	-13	12	13	1	1.9652	D81Br
P(12)	1727.2260	-12	11	12	1	1.9652	D81Br
P(11)	1737.4110	-11	10	11	1	1.9652	D81Br
P(10)	1747.4600	-10	9	10	1	1.9652	D81Br
P(9)	1757.3590	-9	8	9	1	1.9652	D81Br
P(8)	1767.1220	-8	7	8	1	1.9652	D81Br
P(7)	1776.7040	-7	6	7	1	1.9652	D81Br
P(6)	1786.1660	-6	5	6	1	1.9652	D81Br
P(5)	1795.4540	-5	4	5	1	1.9652	D81Br
P(4)	1804.5920	-4	3	4	1	1.9652	D81Br
P(3)	1813.5570	-3	2	3	1	1.9652	D81Br
P(2)	1822.3925	-2	1	2	1	1.9652	D81Br
P(1)	1831.0480	-1	0	1	1	1.9652	D81Br
R(0)	1847.8780	1	1	0	1	1.9652	D81Br
R(1)	1856.0140	2	2	1	1	1.9652	D81Br
R(2)	1863.9990	3	3	2	1	1.9652	D81Br
R(3)	1871.8180	4	4	3	1	1.9652	D81Br
R(4)	1879.4420	5	5	4	1	1.9652	D81Br
R(5)	1886.8990	6	6	5	1	1.9652	D81Br
R(6)	1894.1770	7	7	6	1	1.9652	D81Br
R(7)	1901.2580	8	8	7	1	1.9652	D81Br
R(8)	1908.1730	9	9	8	1	1.9652	D81Br
R(9)	1914.9080	10	10	9	1	1.9652	D81Br
R(10)	1921.4470	11	11	10	1	1.9652	D81Br
R(11)	1927.7750	12	12	11	1	1.9652	D81Br
R(12)	1933.9370	13	13	12	1	1.9652	D81Br
R(13)	1939.9040	14	14	13	1	1.9652	D81Br
R(14)	1945.6590	15	15	14	1	1.9652	D81Br
R(15)	1951.2340	16	16	15	1	1.9652	D81Br
R(16)	1956.5970	17	17	16	1	1.9652	D81Br
R(17)	1961.7800	18	18	17	1	1.9652	D81Br
R(18)	1966.7370	19	19	18	1	1.9652	D81Br
R(19)	1971.4980	20	20	19	1	1.9652	D81Br
R(20)	1976.0480	21	21	20	1	1.9652	D81Br
P(13)	3498.5970	-13	12	13	2	1.9640	D79Br
P(12)	3510.9070	-12	11	12	2	1.9640	D79Br
P(11)	3522.9000	-11	10	11	2	1.9640	D79Br
P(10)	3534.6510	-10	9	10	2	1.9640	D79Br
P(9)	3546.0570	-9	8	9	2	1.9640	D79Br
P(8)	3557.1300	-8	7	8	2	1.9640	D79Br
P(6)	3578.3740	-6	5	6	2	1.9640	D79Br
P(4)	3598.3370	-4	3	4	2	1.9640	D79Br
P(3)	3607.7840	-3	2	3	2	1.9640	D79Br

P(2)	3616.9290	-2	1	2	2	1.9640	D79Br
R(0)	3642.4060	1	1	0	2	1.9640	D79Br
R(3)	3664.9000	4	4	3	2	1.9640	D79Br
R(5)	3678.1590	6	6	5	2	1.9640	D79Br
R(6)	3684.2910	7	7	6	2	1.9640	D79Br
R(7)	3690.0310	8	8	7	2	1.9640	D79Br
P(13)	3497.5130	-13	12	13	2	1.9652	D81Br
P(12)	3509.8970	-12	11	12	2	1.9652	D81Br
P(11)	3521.8900	-11	10	11	2	1.9652	D81Br
P(10)	3533.6270	-10	9	10	2	1.9652	D81Br
P(9)	3545.0020	-9	8	9	2	1.9652	D81Br
P(8)	3556.1060	-8	7	8	2	1.9652	D81Br
P(6)	3577.3500	-6	5	6	2	1.9652	D81Br
P(4)	3597.2820	-4	3	4	2	1.9652	D81Br
P(3)	3606.7140	-3	2	3	2	1.9652	D81Br
P(2)	3615.8440	-2	1	2	2	1.9652	D81Br
P(2)	3641.3670	1	1	0	2	1.9652	D81Br
R(0)	3663.8310	4	4	3	2	1.9652	D81Br
R(3)	3677.0515	6	6	5	2	1.9652	D81Br
R(5)	3683.1610	7	7	6	2	1.9652	D81Br
R(6)	3688.9460	8	8	7	2	1.9652	D81Br

A.3 Code used to generate the non-linear regression on HBr/DBr data. The same code was used for the CO data, using the reduced mass of ^{12}CO as the standard isotope.

```
[Variables]
freq = col(1)
vup = col(5)
jdown = col(4)
jup = col(3)
ua = col(6)
[Parameters]
we = 2650
wexe = 45
weye = 0
Be = 8.47
ae = 0
ge = 0
De = 0
beta = 0
[Equation]
Gup=we*(u/ua)^0.5*(vup+0.5)-wexe*(u/ua)*(vup+0.5)^2+weye*(u/ua)^1.5*(vup
+0.5)^3
```

Gdown=we*(u/ua)^0.5*(0.5)-wexe*(u/ua)*(0.25)+weye*(u/ua)^1.5*(1/8)
Bup=Be*(u/ua)-ae*(u/ua)^1.5*(vup+0.5)+ge*(u/ua)^2*(vup+0.5)^2
Bdown=Be*(u/ua)-ae*(u/ua)^1.5*(1/2)+ge*(u/ua)^2*(1/4)
Dup=De*(u/ua)^2-beta*(u/ua)^2.5*(vup+0.5)
Ddown=De*(u/ua)^2-beta*(u/ua)^2.5*(1/2)
Fup=Bup*jup*(jup+1)-Dup*(jup*(jup+1))^2
Fdown=Bdown*jdown*(jdown+1)-Ddown*(jdown*(jdown+1))^2
u = 0.995426835
f=Gup-Gdown+Fup-Fdown
fit f to freq

A.4 Vibration-rotation constants for $H^{81}Br$ from isotopic global fits of selected data of the HBr and DBr fundamental and overtone bands.

Parameter	Value obtained from HBr fundamental and overtone (cm^{-1})	Value obtained from HBr fundamental, HBr overtone and DBr fundamental (cm^{-1})	Value obtained from HBr and DBr fundamental and overtone bands (cm^{-1})	Literature Value (cm^{-1})[20]
ω_e	2648.933(7)	2649.39(2)	2649.30(3)	2649.3698
$\omega_e x_e$	45.210(2)	45.55(1)	45.46(2)	45.5795
B_e	8.4644(3)	8.4643(1)	8.4639(2)	8.464877
α_e	2.3163(7) x 10^{-1}	2.3257(8) x 10^{-1}	2.325(1) x 10^{-1}	2.33254 x10^{-1}
D_e	3.47(2) x10^{-4}	3.434(5) x 10^{-4}	3.418(9) x 10^{-4}	3.4579 x 10^{-4}
β_e	3.0(6) x 10^{-6}	3.4(2) x 10^{-6}	2.7(3) x 10^{-6}	3.99 x 10^{-6}

A.5 Observed line positions of CO transitions, along with the appropriate parameters used to complete the non-linear regression in SigmaPlot®.

P(J")/R(J")	ν (cm^{-1})	m	J"	J'	v'	μ (amu)	Isotopomer
P(33)	1998.7830	-33	33	32	1	6.8562	^{12}CO
P(32)	2003.6650	-32	32	31	1	6.8562	^{12}CO
P(31)	2008.5310	-31	31	30	1	6.8562	^{12}CO
P(30)	2013.3520	-30	30	29	1	6.8562	^{12}CO
P(29)	2018.1430	-29	29	28	1	6.8562	^{12}CO
P(28)	2022.9040	-28	28	27	1	6.8562	^{12}CO
P(27)	2027.6500	-27	27	26	1	6.8562	^{12}CO
P(26)	2032.3510	-26	26	25	1	6.8562	^{12}CO

P(25)	2037.0220	-25	25	24	1	6.8562	^{12}CO
P(24)	2041.6470	-24	24	23	1	6.8562	^{12}CO
P(23)	2046.2720	-23	23	22	1	6.8562	^{12}CO
P(22)	2050.8530	-22	22	21	1	6.8562	^{12}CO
P(21)	2055.3955	-21	21	20	1	6.8562	^{12}CO
P(20)	2059.9070	-20	20	19	1	6.8562	^{12}CO
P(19)	2064.3910	-19	19	18	1	6.8562	^{12}CO
P(18)	2068.8420	-18	18	17	1	6.8562	^{12}CO
P(17)	2073.2635	-17	17	16	1	6.8562	^{12}CO
P(16)	2077.6485	-16	16	15	1	6.8562	^{12}CO
P(15)	2081.9950	-15	15	14	1	6.8562	^{12}CO
P(14)	2086.3190	-14	14	13	1	6.8562	^{12}CO
P(13)	2090.6130	-13	13	12	1	6.8562	^{12}CO
P(12)	2094.8620	-12	12	11	1	6.8562	^{12}CO
P(11)	2099.0800	-11	11	10	1	6.8562	^{12}CO
P(10)	2103.2690	-10	10	9	1	6.8562	^{12}CO
P(9)	2107.4270	-9	9	8	1	6.8562	^{12}CO
P(8)	2111.5400	-8	8	7	1	6.8562	^{12}CO
P(7)	2115.6230	-7	7	6	1	6.8562	^{12}CO
P(6)	2119.6760	-6	6	5	1	6.8562	^{12}CO
P(5)	2123.6990	-5	5	4	1	6.8562	^{12}CO
P(4)	2127.6760	-4	4	3	1	6.8562	^{12}CO
P(3)	2131.6315	-3	3	2	1	6.8562	^{12}CO
P(2)	2135.5410	-2	2	1	1	6.8562	^{12}CO
P(1)	2139.4280	-1	1	0	1	6.8562	^{12}CO
R(0)	2147.0820	1	0	1	1	6.8562	^{12}CO
R(1)	2150.8630	2	1	2	1	6.8562	^{12}CO
R(2)	2154.6000	3	2	3	1	6.8562	^{12}CO
R(3)	2158.2910	4	3	4	1	6.8562	^{12}CO
R(4)	2161.9670	5	4	5	1	6.8562	^{12}CO
R(5)	2165.5980	6	5	6	1	6.8562	^{12}CO
R(6)	2169.1990	7	6	7	1	6.8562	^{12}CO
R(7)	2172.7550	8	7	8	1	6.8562	^{12}CO
R(8)	2176.2800	9	8	9	1	6.8562	^{12}CO
R(9)	2179.7760	10	9	10	1	6.8562	^{12}CO
R(10)	2183.2260	11	10	11	1	6.8562	^{12}CO
R(11)	2186.6385	12	11	12	1	6.8562	^{12}CO
R(12)	2190.0210	13	12	13	1	6.8562	^{12}CO
R(13)	2193.3585	14	13	14	1	6.8562	^{12}CO
R(14)	2196.6650	15	14	15	1	6.8562	^{12}CO
R(15)	2199.9350	16	15	16	1	6.8562	^{12}CO
R(16)	2203.1590	17	16	17	1	6.8562	^{12}CO
R(17)	2206.3530	18	17	18	1	6.8562	^{12}CO
R(18)	2209.5020	19	18	19	1	6.8562	^{12}CO
R(19)	2212.6210	20	19	20	1	6.8562	^{12}CO

R(20)	2215.7090	21	20	21	1	6.8562	^{12}CO
R(21)	2218.7380	22	21	22	1	6.8562	^{12}CO
R(22)	2221.7510	23	22	23	1	6.8562	^{12}CO
R(23)	2224.7040	24	23	24	1	6.8562	^{12}CO
R(24)	2227.6420	25	24	25	1	6.8562	^{12}CO
R(25)	2230.5190	26	25	26	1	6.8562	^{12}CO
R(26)	2233.3745	27	26	27	1	6.8562	^{12}CO
R(27)	2236.1840	28	27	28	1	6.8562	^{12}CO
R(28)	2238.9570	29	28	29	1	6.8562	^{12}CO
R(29)	2241.6840	30	29	30	1	6.8562	^{12}CO
R(30)	2244.3800	31	30	31	1	6.8562	^{12}CO
R(31)	2247.0320	32	31	32	1	6.8562	^{12}CO
R(32)	2249.6390	33	32	33	1	6.8562	^{12}CO
R(33)	2252.2150	34	33	34	1	6.8562	^{12}CO
R(34)	2254.7460	35	34	35	1	6.8562	^{12}CO
R(35)	2257.2320	36	35	36	1	6.8562	^{12}CO
P(27)	4132.1390	-27	27	26	2	6.8562	^{12}CO
P(26)	4137.7890	-26	26	25	2	6.8562	^{12}CO
P(25)	4143.3180	-25	25	24	2	6.8562	^{12}CO
P(24)	4148.8030	-24	24	23	2	6.8562	^{12}CO
P(23)	4154.2110	-23	23	22	2	6.8562	^{12}CO
P(22)	4159.5600	-22	22	21	2	6.8562	^{12}CO
P(21)	4164.8490	-21	21	20	2	6.8562	^{12}CO
P(20)	4170.0620	-20	20	19	2	6.8562	^{12}CO
P(19)	4175.2290	-19	19	18	2	6.8562	^{12}CO
P(18)	4180.3070	-18	18	17	2	6.8562	^{12}CO
P(17)	4185.2780	-17	17	16	2	6.8562	^{12}CO
P(16)	4190.2350	-16	16	15	2	6.8562	^{12}CO
P(15)	4195.1170	-15	15	14	2	6.8562	^{12}CO
P(14)	4199.9380	-14	14	13	2	6.8562	^{12}CO
P(13)	4204.6690	-13	13	12	2	6.8562	^{12}CO
P(12)	4209.3540	-12	12	11	2	6.8562	^{12}CO
P(11)	4213.9650	-11	11	10	2	6.8562	^{12}CO
P(10)	4218.5000	-10	10	9	2	6.8562	^{12}CO
P(9)	4222.9590	-9	9	8	2	6.8562	^{12}CO
P(8)	4227.3590	-8	8	7	2	6.8562	^{12}CO
P(7)	4231.6830	-7	7	6	2	6.8562	^{12}CO
P(6)	4235.9470	-6	6	5	2	6.8562	^{12}CO
P(5)	4240.1350	-5	5	4	2	6.8562	^{12}CO
P(4)	4244.2630	-4	4	3	2	6.8562	^{12}CO
P(3)	4248.3320	-3	3	2	2	6.8562	^{12}CO
P(2)	4252.2940	-2	2	1	2	6.8562	^{12}CO
P(1)	4256.2260	-1	1	0	2	6.8562	^{12}CO
R(0)	4263.8500	1	0	1	2	6.8562	^{12}CO
R(1)	4267.5410	2	1	2	2	6.8562	^{12}CO

R(2)	4271.1870	3	2	3	2	6.8562	^{12}CO
R(3)	4274.7430	4	3	4	2	6.8562	^{12}CO
R(4)	4278.2380	5	4	5	2	6.8562	^{12}CO
R(5)	4281.6730	6	5	6	2	6.8562	^{12}CO
R(6)	4285.0180	7	6	7	2	6.8562	^{12}CO
R(7)	4288.3020	8	7	8	2	6.8562	^{12}CO
R(8)	4291.5120	9	8	9	2	6.8562	^{12}CO
R(9)	4294.6460	10	9	10	2	6.8562	^{12}CO
R(10)	4297.7190	11	10	11	2	6.8562	^{12}CO
R(11)	4300.7170	12	11	12	2	6.8562	^{12}CO
R(12)	4303.6250	13	12	13	2	6.8562	^{12}CO
R(13)	4306.4880	14	13	14	2	6.8562	^{12}CO
R(14)	4309.2600	15	14	15	2	6.8562	^{12}CO
R(15)	4311.9720	16	15	16	2	6.8562	^{12}CO
R(16)	4314.6080	17	16	17	2	6.8562	^{12}CO
R(17)	4317.1700	18	17	18	2	6.8562	^{12}CO
R(18)	4319.6480	19	18	19	2	6.8562	^{12}CO
R(19)	4322.0960	20	19	20	2	6.8562	^{12}CO
R(20)	4324.3970	21	20	21	2	6.8562	^{12}CO
R(21)	4326.6910	22	21	22	2	6.8562	^{12}CO
R(22)	4328.8760	23	22	23	2	6.8562	^{12}CO
R(23)	4331.0160	24	23	24	2	6.8562	^{12}CO
R(24)	4333.0650	25	24	25	2	6.8562	^{12}CO
R(25)	4335.0390	26	25	26	2	6.8562	^{12}CO
R(26)	4336.9220	27	26	27	2	6.8562	^{12}CO
P(18)	2025.0440	-18	18	17	1	7.1724	^{13}CO
P(17)	2029.2630	-17	17	16	1	7.1724	^{13}CO
P(16)	2033.4210	-16	16	15	1	7.1724	^{13}CO
P(15)	2037.5790	-15	15	14	1	7.1724	^{13}CO
P(13)	2045.7150	-13	13	12	1	7.1724	^{13}CO
P(12)	2049.8130	-12	12	11	1	7.1724	^{13}CO
P(11)	2053.8510	-11	11	10	1	7.1724	^{13}CO
P(10)	2057.8890	-10	10	9	1	7.1724	^{13}CO
P(9)	2061.8660	-9	9	8	1	7.1724	^{13}CO
P(8)	2065.7830	-8	8	7	1	7.1724	^{13}CO
P(7)	2069.6400	-7	7	6	1	7.1724	^{13}CO
P(4)	2081.2110	-4	4	3	1	7.1724	^{13}CO
P(3)	2084.9840	-3	3	2	1	7.1724	^{13}CO
P(2)	2088.6840	-2	2	1	1	7.1724	^{13}CO
P(1)	2092.3610	-1	1	0	1	7.1724	^{13}CO
R(3)	2110.5000	4	3	4	1	7.1724	^{13}CO
R(4)	2113.9360	5	4	5	1	7.1724	^{13}CO
R(5)	2117.4310	6	5	6	1	7.1724	^{13}CO
R(6)	2120.8660	7	6	7	1	7.1724	^{13}CO
R(10)	2134.3660	11	10	11	1	7.1724	^{13}CO

R(11)	2137.6200	12	11	12	1	7.1724	^{13}CO
R(12)	2140.8140	13	12	13	1	7.1724	^{13}CO
R(13)	2144.0080	14	13	14	1	7.1724	^{13}CO

A.6 Vibrational-rotational parameters obtained from global fits of the ^{12}CO and ^{13}CO fundamental and overtone bands.

Parameter	Value obtained from fundamental and overtone bands of ^{12}CO and fundamental band of ^{13}CO (cm^{-1})	Value obtained from fundamental and overtone bands of ^{12}CO (cm^{-1})	Literature Value (cm^{-1})[22]
ω_e	2169.745(5)	2169.740(3)	2169.812670
$\omega_e x_e$	13.237(2)	13.235(1)	13.28787634
B_e	1.93134(7)	1.9313(4)	1.931280985
α_e	1.7505(3) x 10^{-2}	1.7503(2) x 10^{-2}	1.750439229 x 10^{-2}
D_e	6.14(5) x 10^{-6}	6.15(3) x 10^{-6}	6.121615183 x 10^{-6}

Chapter 2: Spectral Shift Determination of Lanthanide-Doped Fibers

2.1 Introduction

I. Fiber Lasers as DPAL Pump Sources

The following research was performed under the Air Force Research Laboratory (AFRL) Summer Scholar Program in the summer of 2016. Special interest has been taken in diode-pumped alkali lasers (DPALs), due to their high-power scalability and efficiency. Alternative pump sources to alkali laser systems, such as lanthanide-doped fiber lasers, have been pursued due to the cost of diode pumps. This research investigates the spectral shifts of lanthanide-doped fiber lasers with the ultimately goal of finding a lanthanide solution that can be used to pump cesium lasers.

Within the past decade, diode-pumped alkali lasers (DPALs) have been of interest to the scientific community. DPALs utilize a three-level laser system, in which the vaporized alkali metal medium is optically pumped from the ground state ($^2S_{1/2}$) to a high energy level ($^2P_{3/2}$), from which it collisionally relaxes to the lower spin-orbit energy level ($^2P_{1/2}$). From this level, the active medium lases down to the ground state. The first DPAL was demonstrated in 2003 by Krupe *et. al.* [1] and used rubidium (Rb) as the active medium, Figure 2.1.1 illustrates the energetic transitions in the Rb laser.

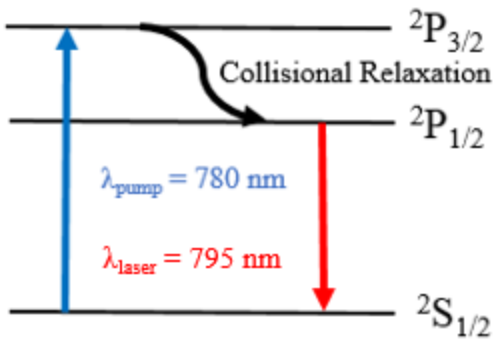

Figure 2.1.1 Energy level diagram for the rubidium (Rb) DPAL.

In 2004, Beach *et. al.*[2] developed a cesium (Cs) DPAL, lasing at 852 nm. Since then, potassium (K) DPALs have also been reported[3].

Due to the small energy difference between the spin-orbit levels, DPALs have small quantum defects, that is, the energy of the lasing photon is slightly less than the energy of the pump photon. This small energy difference which lead to quantum efficiencies of 95% and higher[4]. For example, in a potassium DPAL, the quantum defect is 0.0044, corresponding to a spin-orbit coupling of 57.7 cm^{-1} and a quantum efficiency of 99.56% percent. As the spin-orbit energy gap increases, the quantum defect increase, resulting in a decrease in the quantum efficiency. DPALs also have high output powers[5], typically on the order of 100 mW. Due to the gaseous medium, DPAL systems have excellent beam quality, due to the homogeneity of the alkali gas. Another advantage of these systems is these systems reduced the amount of hazardous materials chemicals used. Many chemical laser systems involve the use of large quantities of hazardous chemicals in order to make the medium lase, such as the chemical oxygen iodine laser (COIL) which employs basic hydrogen peroxide and chlorine gas[6]. DPALs, however, simply use grams of alkali metals, reducing the amount of hazardous materials from a

pound scale down to a gram scale. One big disadvantage of DPAL systems is that they require a very narrow-banded diode pump sources, which are quite costly. In order to solve this problem, fiber lasers have been utilized, as they have the ability to possess spectral widths less than one GHz (corresponding to spectral width of 0.002 nm)[7].

Fiber lasers use an active core embedded in a fiber as the medium of the laser system. Often, the active core being surrounded by multiple layers of cladding. The cladding is employed to ensure that the generated light from the pump is restricted to the smaller active core, resulting in a laser output with higher intensity. To create an optical cavity, dichroic mirrors are placed on either end of the fiber, with a high reflector and an output coupler on the end of the mirrors. The dichroic mirrors serve the purpose of reflecting the laser pump into the fiber and directing the pump outside of the laser system once it passes through the fiber, if the fiber does not possess cladding. Often, internal fiber Bragg gratings are used in replacement of mirrors to reduce the bulk of the laser system [8].

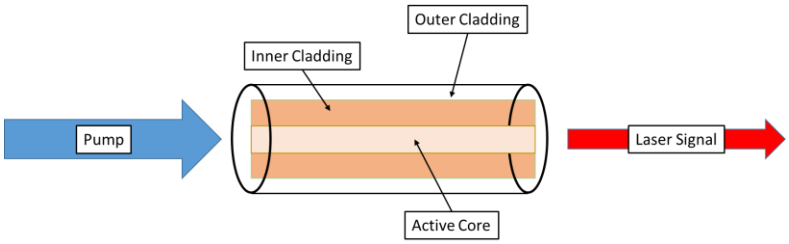

Figure 2.1.2 Diagram of a fiber laser system with cladding.

Fibers have been doped with rare earth metals, as the doping agent improves the laser efficiency, broadens the gain bandwidth, and allows lasing in the near infrared (NIR) region[9]. Common choices for the dopant have included lanthanides such as

ytterbium (Yb), erbium (Er), thulium (Tm), and neodymium (Nd). Mears *et. al.* [10] in 1985 demonstrated the first usage of lanthanides as fiber laser dopants, by developing a Nd-doped fiber laser. For every milliwatt of pump power, the Nd-doped laser was able to achieve decible-level gain profiles. Later, Mears demonstrated an Er-doped fiber laser [11] for the application of optical telecommunication amplification in the mid-infrared (IR) region (1.55μm).

II. Lanthanides

Electronic Configuration and Lanthanide Contraction

Lanthanides (Ln), also referred to as *rare-earth metals*[12], comprise the first period of the *f*-block with valence electrons occupying the 4*f* orbital. Lanthanum (La), as an exception, has the ground state electronic configuration [Xe] $6s^2 5d^1$ and has been the subject of much debate, along with lutetium (Lu), on whether to be included in the lanthanide series, due to lanthanum's lack of 4*f* valence electrons and lutetium's irregularity in periodic trends with the lanthanides[13]. After La, the lanthanides fill the 4*f* orbitals regularly, with some exceptions due to stability of half-filled orbitals, such as gadolium (Gd) and lutetium [14]. As the effective nuclear charge Z_{eff} increases, the 4*f* orbitals become more stable than the 5*d* orbitals, due to nucleus penetration, resulting in placement of the 5*d* electron into the 4*f* orbital. This results in [Xe] $6s^2\ 4f^3$ and [Xe] $6s^2\ 4f^9$ electronic configurations for praseodymium (Pr) and terbium (Tb), respectively[15].

The 4*f* electrons can be considered as part of the inner core of the lanthanide, as they lie closer to the nucleus than the 5*s*, 5*p*, and 6*s* electrons, as determined by their radial distribution functions[16]. In the case of ionization, the 6*s* electrons are lost first as

they are the most weakly bound to the inner core. Due to core penetration from the 5*s* and 5*p* electrons, the 4*f* electrons are lost next in ionization. With each 4*f* electron that is lost, Z_{eff} increases greatly, resulting in increased attraction of 4*f* electrons to the core. This limits the oxidation state of free-ion lanthanides to 3+. All of the Ln^{3+} ions therefore have [Xe] $4f^n$ electronic configurations. Most lanthanides favor the 3+ oxidation state, an exception being Ce, which favors 2+ or 4+ oxidation states[12].

As the 4*f* electrons penetrate the core more deeply than the 5*d* and 6*s* electrons, they are not readily available for bonding, due to insufficient overlap with bonding orbitals. However, since 5*d* and 5*p* orbitals are not shielded from the increasing Z_{eff}, they contract as Z_{eff} increases[15]. This is known as *lanthanide contraction*, resulting in decreasing atomic and ionic radii [12]. Therefore, the trivalent lutetium (Lu) cation has the shortest atomic radius of 98 pm of the lanthanides[17]. Lanthanide contraction also results in contraction of the $4f^n$ subshell.

<u>Nd^{3+} and Tm^{3+} Energy Levels</u>

Trivalent neodymium (Nd^{3+}) has the electronic configuration [Xe] $4f^3$, which results in the following term symbols[18]:^{4}I, ^{4}G, ^{4}F, ^{4}D, ^{4}S, ^{2}L, ^{2}K, ^{2}H(2), ^{2}G (2), ^{2}F (2), ^{2}D (2), and ^{2}P, with their corresponding expansion into multiple *J* states. According to Hund's Rules, the term with the highest angular momentum *L* and the lowest total angular momentum *J* will be lowest in energy, as the *f* orbital is less than half-filled[19]. Therefore, the $^4I_{9/2}$ term will be the ground state. A transition of importance is the 1.064μm $^4I_{11/2} \leftarrow {}^4F_{3/2}$ lasing wavelength of Nd^{3+} lasers. Figure 2.1.3 shows selected energy levels of Nd^{3+} arising from the $4f^3$ electronic configurations[20].

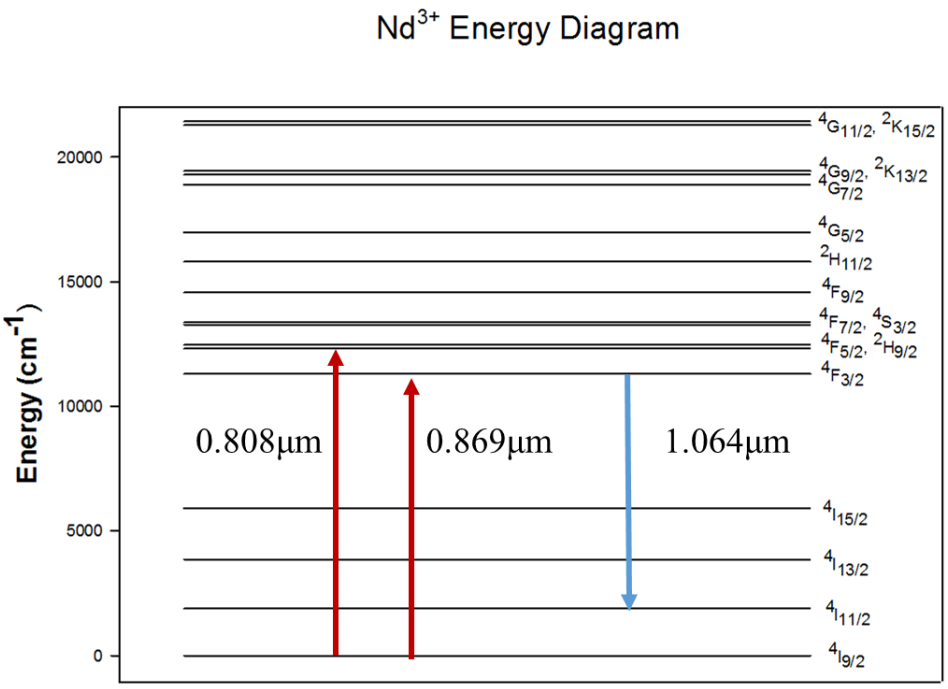

Figure 2.1.3 Energy level diagram for the [Xe] $4f^3$ electronic configuration of trivalent neodymium (Nd^{3+}). Common pumping and lasing transitions of Nd^{3+} lasers are shown.

Trivalent thulium (Tm^{3+}) has a ground state electronic configuration of [Xe] $4f^{12}$, resulting in the following term symbols[18]:$^3H_{6,5,4}$, $^3F_{4,3,2}$, $^3P_{2,1,0}$, $^1I_6$, $^1G_4$, $^1D_2$, and $^1S_0$, with $^3H_6$ as the ground state[19]. Tunable Tm-doped silica fiber lasers[21] use the $^3H_6 \leftarrow {}^3F_4$ transition to lase from 1.7-2.1 µm. The 800 nm $^3H_4 \leftarrow {}^3H_6$ absorbance transition has also been used as another lasing transition for Tm-doped fiber amplifiers[22]. Both of these transitions are included in Figure 2.1.4, which shows the energy diagram of Tm^{3+}.

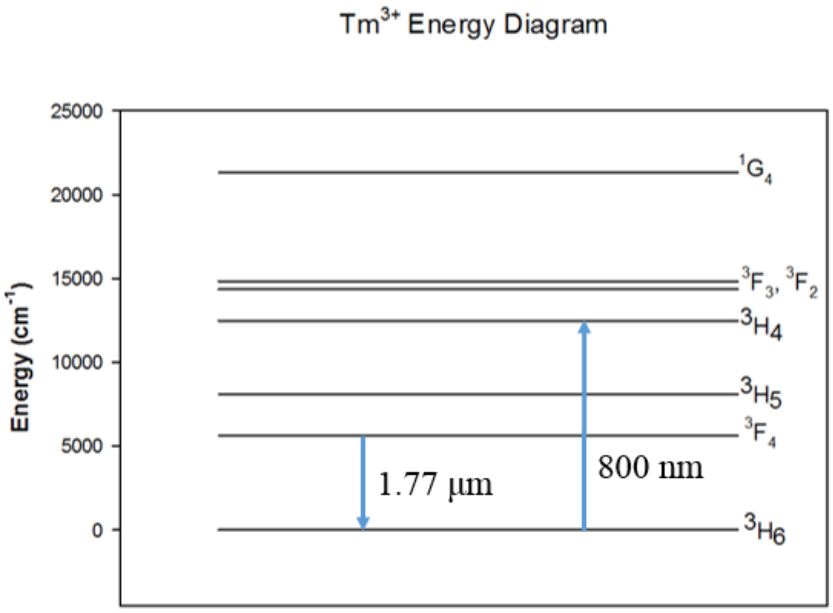

Figure 2.1.4 Energy diagram of the [Xe] $4f^{12}$ electronic configuration of Tm^{3+}. Included are common lasing and absorbance features used in fiber lasers and amplifiers.

III. Crystal Field Theory

Introduction

In 1929, in order to understand the effects of surroundings ions on the electronic distribution in the ions of a sodium chloride (NaCl) lattice, Bethe[23 24] concluded that the ions in the lattice were spheres that were unable to be deformed and that the interactions between the spheres were the result of electrostatic potential of the spheres, created by their charge. In the case of NaCl, the positive sodium ion was surrounded by six negative chloride ions, creating at the point (*x*,*y*,*z*) an electrostatic potential

$$\vec{v}_{(i;x,y,z)} = \frac{e}{r_{(i;x,y,z)}} \quad (1)$$

where $\vec{v}_{(i;x,y,z)}$ is the potential caused by the i^{th} ion and $r_{(i;x,y,z)}$ is the distance from the point *(x,y,z)* to the i^{th} ion[24]. The total potential near the central atom, in this case the sodium cation, can be expressed as the sum of the individual potentials from the individual surrounding ions.

$$\vec{v}_{(x,y,z)} = \sum_{i=1}^{6} \vec{v}_{(i;x,y,z)} \quad (2)$$

This discussion of the interaction potentials between ions became known as *crystal field theory*, as it was believed that such potentials exists in lattices, which were found only in crystals. Crystal field theory is often employed, as it is simple and easy to visualize. However, crystal field theory only considers ionic charge interactions and ignores any covalent interactions between the central atom and the surround atoms, also known as *ligands*. Due to its insufficiency for covalent interactions, crystal field theory is often replaced by *ligand field theory*, which seeks to explain those covalent interactions[25]. As lanthanide halides, the compounds of interest, occupy crystalline environment, crystal field theory will be used to analyze the interactions between the lanthanides and their surrounding ligands.

Coordination Numbers

Crystal field theory employs *coordination numbers*, describing the number of ligands that surround the central atom. A coordination number of two describes two ligands surrounding a central atom, resulting in linear geometry. A coordination number of three infers a trigonal planar or less commonly a trigonal pyramidal geometry whereas a coordination number of four represents a tetrahedral or square planar geometry and so

on. Table 2.1.1 shows common coordination numbers and the molecular geometries associated with them[17].

Table 2.1.1 Coordination numbers and their respective molecular geometries.

Coordination Number	Common Molecular Geometry
2	Linear
3	Trigonal planar; Trigonal pyramidal
4	Tetrahedral; Square planar
5	Trigonal bipyramidal; Square-based pyramidal
6	Octahedral; Trigonal Prismatic
7	Pentagonal bipyramidal; Monocapped trigonal prismatic; Monocapped octahedral
8	Dodecahedral; Square antiprismatic; Hexagonal bypyramidal; Cube; bi-capped trigonal prismatic
9	Tri-capped trigonal prismatic

Due to the large radii of the lanthanides (r_{Ln}= 173-199 pm), coordination numbers equal to or greater than six are often observed in lanthanide complexes[17]. When monodentate ligands, ligands that donate a single pair of electrons to the central atom, surround lanthanides, a maximum coordination number of nine is observed. Examples would be complexes that contain water (H_2O) or halides (X^-) as the surrounding ligands. Typically lanthanides with monodentate ligands possess geometries based on trigonal prismatic or octahedral geometries. As the coordination number increases, ligands can be added to the lanthanide by capping the geometry. It is quite common to observed bi/tri-capped trigonal prismatic geometries for high coordination number lanthanide complexes. In the case of lanthanide halides, the coordination number decreases with the increasing radius of the halide and the lanthanide, due to electronic repulsion between the halide ligands

and the inability for larger lanthanides to sustain higher geometries[26]. Table 2.1.2 gives the coordination number and molecular geometries for select lanthanide halides.

Table 2.1.2 Coordination number and geometry for chosen lanthanide halides.

Compound	Coordination Number	Geometry
$NdCl_3$	9	Tri-capped trigonal prism
$NdBr_3$	8	Bi-capped trigonal prism
$TmCl_3$	6	Octahedral
$TmBr_3$	6	Octahedral

Energy Level Splitting

In crystal field theory, the *d* orbitals of transition metals in metal-ligand complexes are not five-fold degenerate but rather split into different energy levels, due to the interaction between the *d*-electrons of the central metal and the electrostatic field from the surrounding ligands. The energy levels are split above and below the center of gravity, or *barycenter*, of the unsplit, five-fold degenerate energy levels[27]. The splitting of energy levels is dependent on the geometry of the metal-ligand complex and therefore dependent on the coordination number of the complex itself. The separation of orbitals is known as the *ligand-field splitting parameter*, Δ_0.

In an octahedral environment, electrons in *d* orbitals that lie directly on Cartesian axes experience a greater repulsion from the ligands, as the orbitals are pointed directly at the ligands. This results in an increase in the energy of the $d_{x^2-y^2}$ and d_{z^2} orbitals, splitting the *d* orbitals in a lower triply degenerate set and an upper double generate set. In an octahedral arrangement (O_h), the doubly degenerate $d_{x^2-y^2}$ and d_{z^2} orbitals maintain an e_g

symmetry while the triply degenerate d_{zxy}, d_{yz}, and d_{xz} orbitals occupy a t_{2g} symmetry. The lower and upper sets of *d* orbitals are located $2/5\Delta_o$ and $3/5\Delta_o$ below and above the barycenter, respectively. Generally, the ligand-field splitting parameter increases with the increasing oxidation number of the central metal and increases down a group. Figure 2.1.5 shows the energy level diagram of the *d* orbitals in an O_h symmetry [25].

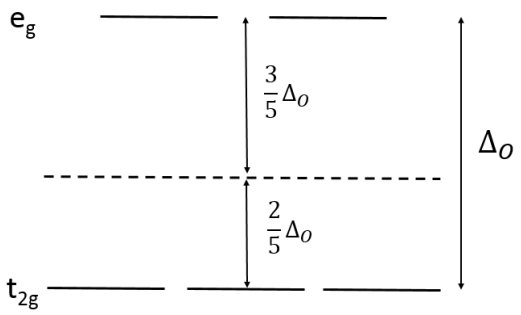

Figure 2.1.5 Energy diagram of the *d* orbitals in an octahedral crystal field splitting.

In a tetrahedral crystal environment, electrons in *d* orbitals that lie on Cartesian axes lie furthest away from the ligands, which can be considered as occupying alternative vertices of a cube with the metal ion lying at the center of the cube. This results in an increase in energy of the d_{xy}, d_{yz}, and d_{xz} orbitals. The triply degenerate d_{xy}, d_{yz}, and d_{xz} orbitals occupy a t_2 symmetry while the double degenerate $d_{x^2-y^2}$ and d_{z^2} orbitals occupy a e_g symmetry, the subscript of "2" being omitted due to the lack of a center of symmetry in a tetrahedral arrangement[27]. The distance between the t_2 and e orbitals is equal to the tetrahedral ligand-field splitting parameter Δ_T, with the distance from the barycenter being $2/5\Delta_T$ and $3/5\Delta_T$ for the t_2 and e orbitals, respectively [25]. Figure 2.1.6 shows the energy diagram of the *d* orbitals in a tetrahedral environment.

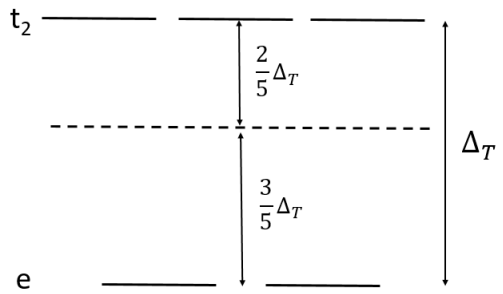

Figure 2.1.6 Energy diagram of the *d* orbitals in a tetrahedral crystal field splitting.

Lanthanides in their ground state $4f^n$ configuration as well as transitions between the $4f^n$ levels do not experience much of crystal field splitting, due to the shielding of the 4*f* electrons from outer electrons. As a result, the energy levels of the $4f^n$ configurations are invariant within a few hundred wavenumbers (cm^{-1}) in different crystalline environments [28] [29]. The crystal field interaction with 4*f* electrons does result in splitting each multiplet energy level into $2J+1$ levels, where *J* is the total angular momentum. This crystal field splitting is considerably less that spin-orbit coupling, resulting in a good approximation of each energy level in terms in Russel-Sanders (*L*-*S*) coupling[30].

In contrast, the $4f^{n-1}5d$ energy levels experience a greater crystal field splitting, due to the interaction of the 5*d* electron with the surrounding ligands. This crystal field splitting is generally on the order of ten thousand wavenumbers. For example, when Ce^{3+} is surrounded by $LiYF_4$ ligands, the 5d→4f($^2F_{5/2}$, $^2F_{7/2}$) transition is located around 310 nm (corresponding to 32,300 cm^{-1}). When sulfide compounds such as Lu_2S_3 are employed as the ligand, the emission line is shifted to 600 nm (16,600 cm^{-1}) [28]. The crystal field splitting in lanthanides is also dependent on the coordination number of the lanthanide. Dorenbos *et. al.* [31] calculated the crystal field splitting of numerous Ce^{3+} and Eu^{3+} complexes. Dorenbos concluded that octahedral complexes exhibited the greatest crystal

field splitting, followed by cubal, and dodecahedral coordinations, with tri-capped trigonal prism and cuboctahedral coordinations exhibiting the smallest crystal field splitting. It was also observed that crystal field splitting decreases with increasing distance of the metal ion to the ligands[31].

IV. Lanthanide Absorbance and Emission Spectra

Electronic Transitions

Lanthanide absorbance and emission transitions between the $4f^n$ and $4f^{n-1}5d$ energy levels to the ground state are located in the ultraviolet/visible (UV-VIS) to near-infrared (NIR) region. Generally, $4f^n \leftrightarrow 4f^n$ transitions are spectrally sharp, due to shielding of the 4*f* electrons, and have weak intensities, as $f \leftrightarrow f$ transitions are electron-dipole forbidden. These transitions can be attributed to higher electronic states with opposite parity mixing with $4f^n$ levels, the mixing resulting from an odd parity crystal field which can be viewed as causing a perturbation in the $4f^n$ energy levels[17,32,33]. Because the crystal field splitting of $4f^n \leftrightarrow 4f^n$ transitions is quite weak (~100 cm^{-1}), the Russel-Sanders (*L*-*S*) coupling scheme is used for the corresponding energy levels. The crystal field is therefore seen as a perturbation of the Russel-Sanders energy levels, splitting individual *J* states. As a coupling-scheme, Russel-Sanders coupling only holds for light (less-than half filled) lanthanides but it is still used to label energy states for all lanthanides for the sake of convenience[30].

Transitions arising from $4f^{n-1}5d$ levels are spectrally much wider than $4f^n$ transitions, as interaction of the 5*d* electron with lattice phonons results in spectral broadening. As opposed to the $4f^n$ levels, the $4f^{n-1}5d$ multiplet level splitting in a crystal

field is not resolved but rather adds to the broadening of the transition band[28]. As mentioned before, the $4f^{n-1}5d$ energy levels depend on the crystal environment of the lanthanide, resulting in a large spectral shift of the transition.

There are some transitions of lanthanides that are extremely sensitive to the strength of the crystal field and to the change in the symmetry of the complex. As a result, the absorbance bands usually shift to higher wavelengths, with varying intensity and band splitting[15]. The intensities have been known to differ by factors of 10-100 and obey a selection rule of $\Delta J \leq 2$. Judd has named such transitions as *hypersensitive transitions*[34,35]. The variation in intensity and wavelength shift has been attributed to the polarizability of the solvent, as the polarization vector of the solvent can be seen as increasing the electric vector component of the electromagnetic radiation that passes through the lanthanide, resulting in an increase in intensity of the transition. Typically, aqueous lanthanide solutions are used as the reference for solution spectral shifts[30].

Theoretical Treatment of Transition Intensity

The molar extinction coefficient ε_i of an atomic transition is defined as[36]

$$\varepsilon_i = \frac{\pi N e^2}{2303 c m_e} P\varphi(\nu) \tag{3}$$

where N is Avogadro's number, e is the charge of the electron, c is the speed of light, m_e is the mass of the electron, P is the oscillator strength of the vibrational mode, and $\varphi(\nu)$ is a function such that $\varphi(\nu)d\nu_i$ is the fraction of atoms present with a frequency of the i^{th} mode that lies between ν_i and $\nu_i + d\nu_i$. By definition,

$$\int \varphi(\nu) d\nu = 1 \tag{4}$$

Integration of (3) allows ε_i to be determined experimentally.

$$\int \epsilon_i d\nu = \frac{\pi N e^2}{2303 c m_e} P \int \varphi(\nu) d\nu = \frac{\pi N e^2}{2303 c m_e} P \tag{5}$$

Solving for *P* yields

$$P = \frac{2303 m_e c}{\pi N e^2} \int \epsilon_i d\nu \tag{6}$$

To account for the refractive index of the solution, (6) becomes

$$P = \frac{2303 m_e c}{\pi N e^2} \frac{9 n_0}{\left(n_0^2+2\right)^2} \int \epsilon_i d\nu \tag{7}$$

where n_0 is the refractive index of the medium. As the refractive index of the solution approaches n_o=1, (7) approaches (6). In the case of absorption lines, the lines correspond to transitions from the ground state to an excited state. Therefore, the oscillator strength of the line can be calculated from the sum of the oscillator strength of the various components of the transition, weighted to account for the probability of occupation in the ground level. In the case of lanthanide $f \leftrightarrow f$ transitions, the probability of occupation in the highest level to the lowest level rarely exceeds 0.3 at 298K. Therefore, it can be assumed that all ground level components are equally occupied without introducing much error[35].

Judd[35] concluded that oscillator strength *P* of an induced electric-dipole transition can be written as

$$P = \sum_{\lambda=2,4,6} T_\lambda \nu (l^N \psi_J || U^{(\lambda)} || l^N \psi'_{J'})^2 \tag{8}$$

where l^N is the angular momentum of the initial and final state, ψ_J and $\psi'_{J'}$ are the total angular momentum *J*-dependent wavefunctions of the initial and final states, and $U^{(\lambda)}$ is a

unit tensor operator which connects the initial and final states by the parameter T_λ. Any value of λ greater than 6 resulted in negligible matrix elements so Judd limited his values of λ to 2,4, and 6. In order to generalize Judd's oscillator strength definition for any ions in any solutions, Carnall *et. al.* [30] introduced a weighting factor of $(2J+1)^{-1}$, which Judd had included in his definition of T_λ. Eq (8) is then rewritten as

$$P = \sum_{\lambda\ even} \tau_\lambda \nu \left(l^N \psi J \left|\left| U^{(\lambda)} \right|\right| l^N \psi' J' \right)^2 / (2J+1) \tag{9}$$

where

$$\tau_\lambda = (2J+1) T_\lambda \tag{10}$$

In the case of trivalent lanthanide transitions, the total oscillator strength of an absorbance transition is the sum of the electric dipole, magnetic dipole and quadrupole oscillator strengths. The quadrupole oscillator strength is considered negligible, however, as it is 2-4 orders of magnitude smaller than the electric dipole and magnetic dipole oscillator strengths[37,38].

The oscillator strength of a magnetic dipole transition is defined as

$$P_{mag} = \frac{8\pi^2 m_e c}{3he^2} \nu n_0 \left[\frac{S\left(\psi_J ; \psi'_{J'}\right)}{2J+1} \right] \tag{11}$$

where h is Planck's constant and S is the line strength defined as

$$S\left(\psi_J ; \psi'_{J'}\right) = \left(\frac{e^2}{4m_e^2 c^2}\right) \left(\psi J || \vec{L} + 2\vec{S} || \psi' J'\right)^2 \tag{12}$$

Magnetic dipole transitions are limited by the $\Delta J \leq 1$, $\Delta L=0$, $\Delta S=0$, and $\Delta l=0$ selection rules in the pure Russel-Sanders coupling extreme. Therefore, magnetic transitions in

lanthanides will be limited to absorption from the ground state to the first excited state of the ground multiplet i.e. in Tm^{3+}, the only magnetic dipole transition will be the $^3H_6 \rightarrow {}^3H_5$ transition.

In states with negligible magnetic dipole oscillator strengths, the electric dipole oscillator strength *P* can be calculated from experimental data using (7). The matrix tensor $U^{(\lambda)}$ can then be expanded by introducing eigenparameters and by transforming matrix elements into physical Russel-Sanders coupling elements[39]. Once $U^{(\lambda)}$ is determined, optimized values for the parameter τ_λ can be determined for varying even values of λ using a least-squares analysis[38,39]. For states with appreciable magnetic dipole oscillating strengths, (11) and (12) were used to calculate P_{mag}, which was then subtracting from the experimental intensity of the transition, attributing the remainder value as the electric dipole oscillating strength *P*.

Experimentally, it has been found that τ_2 considerably varies with the chemical environment of the lanthanide while τ_4 and τ_6 remain consistent in different environments. In condensed and vapor phases of trihalide lanthanides, τ_4 and τ_6 were nearly equal while τ_2 varied by an order of magnitude or more. It was determined that it was in hypersensitive transitions in which τ_2 varied[32].

V. Motivation and Purpose of Research

Lanthanide-doped fiber lasers have the potential to serve as pumps for alkali lasers. In 2005, a Tm^{3+}-doped fiber amplifier having a gain profile near the 852 nm cesium pump line was demonstrated by Watekar *et. al.*[22]. In order to be an efficient pumping source for a cesium laser, a thulium-doped fiber laser would ideally have

pumping and lasing transitions at 785 nm and 852 nm, respectively. A pumping transition at 785 nm would operate on the $^3H_4 \leftarrow {}^3H_6$ Tm^{3+} absorbance transition. However, due to crystal field splitting, the spectral profile of the 795 and 850 nm absorbance and emission lines has been observed to shift when different doping agents are used. Carter *et. al.*[40] reported that when thulium-fluorozirconate was used, the 850 nm emission profile of Tm^{3+} was shifted to 810-830 nm.

In order to create an efficient pump source for alkali lasers, the spectral shifts of the absorption and emission transition of the lanthanide-doped fiber lasers must be understood and investigated. The need to know these spectral shifts motivated the experimental work conduction during the AFRL Summer Scholars program. Broadly-state, the experimental goals were to determine the spectral shifts from experimentally obtained absorption and emission spectra of lanthanide-halide solutions in different organic solvents. Altering the concentration of the lanthanide halide as well as the concentration of ions by addition of alkali halides salts was also employed to note the influence of lanthanide or halide concentration on spectral shifts. Absorbance and emission spectra were obtained by UV/VIS/NIR spectroscopy and laser-induced fluorescence (LIF), respectively.

2.2 Experimental

In order to determine lanthanide spectral shifts due to solvent crystal field splitting, lanthanide halide solutions were prepared. The chosen lanthanide halides were thulium chloride ($TmCl_3$), thulium bromide ($TmBr_3$), neodymium chloride ($NdCl_3$), and neodymium bromide ($NdBr_3$). Thulium (Tm^{3+}) powder along with neodymium TRIS (2,2,6,6-tetramethyl-3,5-heptanedionato-neodymium) were also dissolved in solution. Polar protic solvents were chosen and included deuterated water (D_2O), acetone ($O(CH_3)_2$), methanol (CH_3OH), and ethanol (CH_3CH_2OH). Tetrachloromethane (CCl_4) was also used as an aprotic solvent for the lanthanide compounds. A few drops of nitric acid (HNO_3) or deuterium chloride (DCl) were added to solutions to improve solubility, if needed. Once all solutions were prepared, absorbance spectra were taken with a PerkinElmer Lambda 950 UV/VIS/NIR spectrophotometer from 400 nm-2.0 μm. Spectral shifts were calculated using the transition in D_2O as a reference. Alkali halides were also added to Tm^{3+}/D_2O and $NdBr_3/D_2O$ solutions to create 1%, 5%, and 10% halide by weight solutions in order to note if the increase of halide ions had any effect on spectral shifts. Chosen alkali halide salts were sodium chloride (NaCl), sodium bromide (NaBr), potassium chloride (KCl), and potassium bromide (KBr). Concentrations of $NdBr_3$ in D_2O were varied from 0.25M to 1.23M to note any spectral shift based on lanthanide concentration.

Emission spectra were determined using laser-induced fluorescence (LIF). Diode lasers at lasing wavelengths of either 785 nm or 808 nm were chosen for fluorescence

excitation.. The diode laser at 785 nm was chosen for all the thulium-containing solutions while the 808 nm diode was used for the neodymium-containing solutions. The output of the fiber laser was placed next to the entrance window of a 1.2 cm plastic or glass cuvette, which contained the lanthanide solution. At the far end of the cell, a beam dump or power meter was placed to catch the diode laser beam or to measure the beam power. To the side of the cell, a 1" diameter, 75mm focusing lens was placed 25mm from the cell to collect lanthanide emission and focus it onto the detector, placed 75mm away from the focusing lens . For the Tm or Nd samples, an InGaAs 1.2-2.6 μm detector connected to an oscilloscope or a SpectraPro-300i 0.300 meter Triple Grating Monochromator was employed, respectively. For the 808 nm diode laser, the water cooler was run at 12 C and 10 A of current were supplied to the diode, resulting in 3.19 W of cw laser output power. For the Nd solutions, an exposure time of 60 seconds was used. Lanthanide solutions absorbed approximately 3 W of the 3.19 W of laser output power, resulting in a rise of solution temperature.

2.3 Results

Table 2.3.1 reports the solutes, solvents, and concentrations of choice and whether these combinations were soluble, insoluble, or soluble with the addition of HNO_3 or DCl. Concentrations were chosen based on the available quantity of the solute.

Table 2.3.1 Chosen solutes, solvents, concentrations, and solubility of Tm/Nd solutions.

Solute	Solvent	Concentration (M)	Solubility
$NdBr_3$	D_2O	1.23	Soluble
	acetone		
	methanol		
	ethanol		
$NdCl_3$	D_2O	1.23	Soluble
	acetone		**Insoluble**
	methanol		
	ethanol		Soluble
NdTRIS	D_2O	0.01	Soluble
	acetone		
	methanol		
	ethanol		
Tm^{3+}	D_2O	0.12	Soluble with HNO_3
	acetone		Soluble with DCl
	methanol		Soluble with HNO_3
	ethanol		
$TmBr_3$	D_2O	0.20	Soluble
	acetone		
	methanol		
	ethanol		
$TmCl_3$	D_2O	1.23	Soluble
	acetone		**Insoluble**
	methanol		
	ethanol		Soluble

UV/VIS/NIR spectra of the $TmBr_3$ and $NdBr_3$ solutions are shown below. Peaks have been labeled with the upper energy level of the atomic transition corresponding to the peak. The absorbance spectra of the other lanthanide solutions can be found in Appendix B. Spectral resolution was 0.05 nm and 0.2 nm for UV-VIS and NIR transitions, respectively.

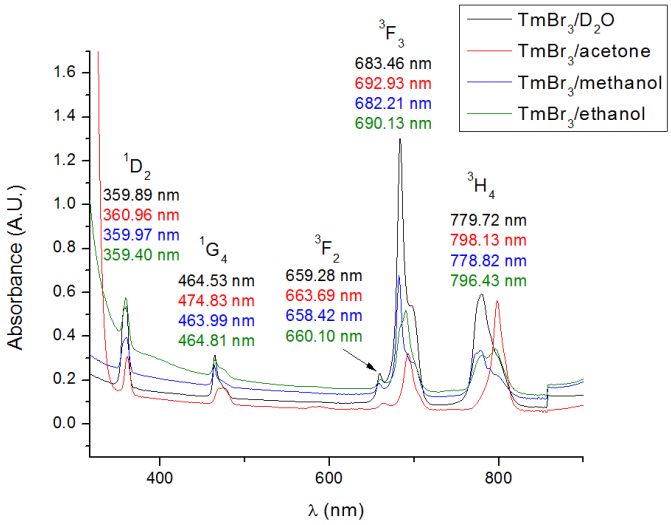

Figure 2.3.1 Absorbance spectrum of $TmBr_3$.

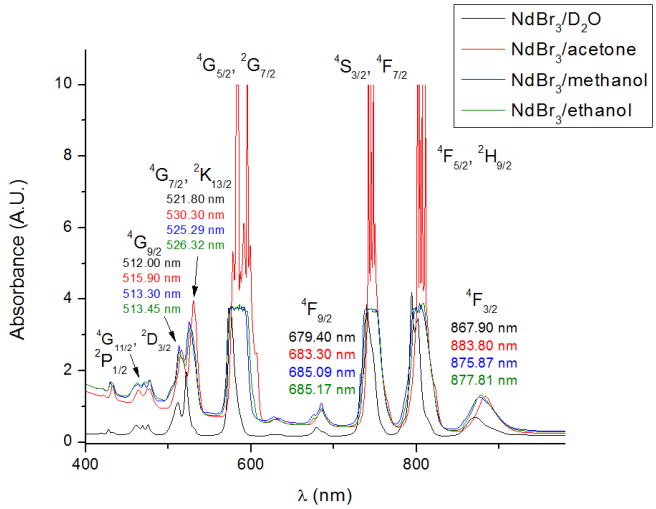

Figure 2.3.2 Absorbance spectrum of $NdBr_3$.

Spectral shifts were calculated using the peak in D_2O as a reference, subtracting the peak value in D_2O from the peak value in the chosen solvent. Energy levels are denoted by their Russel-Sanders coupling term symbols.

Table 2.3.2. Spectral shifts of Tm/Nd solutions.

Solute	Upper Energy Level	Shift in acetone (nm)	Shift in methanol (nm)	Shift in ethanol (nm)
$NdBr_3$	$^4G_{9/2}$	4.90	1.03	1.45
	$^4G_{7/2}$, $^2K_{13/2}$	8.50	3.30	4.52
	$^4F_{9/2}$	3.90	5.69	5.77
	$^4F_{3/2}$	15.9	7.97	9.91
$NdCl_3$	$^4G_{9/2}$	--	--	2.11
	$^4G_{7/2}$, $^2K_{13/2}$	--	--	4.26
	$^4F_{9/2}$	--	--	6.08
	$^4F_{3/2}$	--	--	10.79
NdTRIS	$^4G_{9/2}$	8.00	6.67	6.91
	$^4G_{5/2}$, $^2G_{7/2}$	10.18	6.69	6.52
	$^4S_{3/2}$, $^4F_{7/2}$	7.95	8.34	8.49
	$^4F_{5/2}$,$^2H_{9/2}$	10.00	9.98	10.05
Tm^{3+}	$^3F_3$	7.13	6.27	-3.58
	$^3H_4$	16.58	12.08	15.09
$TmBr_3$	$^1D_2$	1.07	0.08	-0.49
	$^1G_4$	10.30	-0.54	0.28
	$^3F_2$	4.44	-0.86	0.82
	$^3F_3$	9.47	-1.25	6.67
	$^3H_4$	18.41	-0.90	16.71
$TmCl_3$	$^1D_2$	--	--	-0.07
	$^1G_4$	--	--	2.36
	$^3F_2$	--	--	1.96
	$^3F_3$	--	--	7.45
	$^3H_4$	--	--	16.99

From the data obtained, a general trend of $\Delta\lambda_{methanol} < \Delta\lambda_{ethanol} < \Delta\lambda_{acetone}$ can be established. This can be attributed to the number of vibrational modes of the solvent. As the number of vibrational modes of the solvent increases, the crystal field splitting of the lanthanide energy level increases, resulting in greater spectral shift. Generally, the

spectral shifts in the solvents are red shifts but occasionally some transitions are blue shifted, such as $^3F_3$ in Tm^{3+}/ethanol. Another possibility for the magnitude of the spectral shifts is that some solvent frequencies may have higher efficiencies than others, resulting in different shifts for the same lanthanide transition in different solvents. Such dependencies have been noted for the collisional deactivation of the $^1\Delta_g$ state of molecular oxygen[41]. If the magnitude of the shift is due to specific solvent frequencies rather than the number of vibrational modes, this may explain why certain transitions were blue shifted, as some solvent frequencies may increase the energy of the upper energy level in the absorbance transition.

Laser-induced fluorescence emission spectra were obtained for the Nd samples. Figure 2.3.3 shows the emission spectrum of $NdBr_3$ in differing solvents. Fluorescence emission spectra for $NdCl_3$ and NdTRIS can be found in Figure A.5 and Figure A.6.

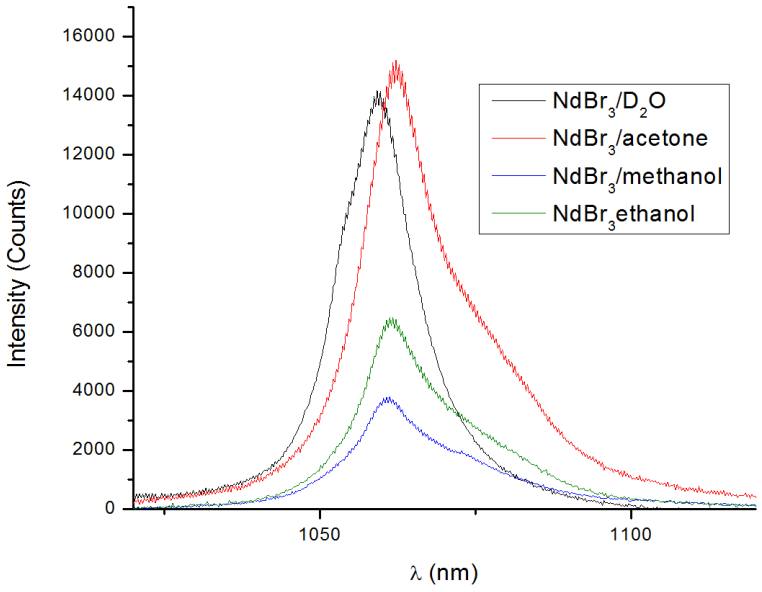

Figure 2.3.3 Laser-induced fluorescence (LIF) emission spectra of $NdBr_3$ in D_2O, acetone, and methanol.

The same spectral shifting and trend apparent in absorbance spectra is seen in the fluorescence emission spectra. As with the absorbance data, as the number of vibrational modes of the solvent increases, the spectra shifting of the lanthanide transition in the solvent increases. Laser-induced Tm fluorescence at 1.8μm was unable to be obtained in the Tm solutions. It is believed that the 1.8μm fluorescence was unable to be observed due to solvent hydroxyl quenching. Further research would investigate Tm fluorescence, using aprotic solvents, in hopes of creating a Tm-doped fiber laser for alkali laser pumping applications.

Adding alkali halide salts and increasing the concentration of the lanthanide halide resulted in minimal spectral shifts. This indicates that the spectral shift of the lanthanide in solution is largely independent of the concentration of the halide or lanthanide. The solvent-solute interaction can be concluded to be between the solvent itself and the trivalent lanthanide and totally independent of the concentration. This confirms that the spectral shift is a result of crystal field splitting caused by the solvent energy.

Traditionally, a diode pump operating at 852 nm is used to pump cesium lasers. While it was not observed, Tm^{3+} emission from $^3H_6 \leftarrow ^3H_4$ could be used to pump cesium, if the proper solvent was used to shift this transition to 852 nm. Observed Nd^{3+} fluorescence at 1.06μm allows a more efficient laser source at this wavelength to be used in alternative to traditional 1.06μm sources.

2.4 References

1. Krupke, W. F.; Beach, R. J.; Kanz, V. K.; Payne, S. A. Resonance transition 795-nm rubidium laser. *Opt. Lett.* **2003**, *28*, 2336-2338.

2. Beach, R. J.; Krupke, W. F.; Kranz, V. K.; Payne, S. A. End-pumped continuous-wave alkali vapor lasers: experiment, model, and power scaling. *J. Opt. Soc. Am. B.* **2004**, *21*, 2151.

3. Krupke, W. F. Diode pumped alkali lasers (DPALs)-A review (rev 1). *Progress in Quantum Electronics* **2012**, *36*, 4-28.

4. Hager, G. D.; Perram, G. P. A three-level analytic model for alkali metal vapor lasers: part I. Narrowband optical pumping. *Appl. Phys. B.* **2010**, *101*, 45.

5. Zhdanov, B. V.; Knize, R. J. Advanced diode=pumped Alkali lasers. *Proc. SPIE* **2007**, *7022*, 7022J-1.

6. McDermott, W. E.; Pchelkin, N. R.; Benard, D. J.; Bousek, R. R. An electronic transition chemical laser. *App. Phys. Lett.* **1978**, *32*, 469.

7. Dianov, E. M. Bismuth-doped optical fibers: a new active medium for NIR lasers and amplifiers. *Proc. of SPIE* **2013**, *8601*, 86010H-1.

8. Zervas, M. N.; Codemard, C. A. High Power Fiber Lasers: A Review. *IEEE. J. Sel. Topics Quantum Electron.* **2014**, *20*, 0904123.

9. Richardson, D. J.; Nilsson, J.; Clarkson, W. A. High power fiber lasers: current status and future perspectives [Invited]. *J. Opt. Soc. Am. B* **2010**, *27*, B63.

10. Mears, R. J.; Reekie, L.; Poole, S. B.; Payne, D. N. Neodymium-doped silica single-mode fiber lasers. *Electron. Lett.* **1985**, *21*, 738-740.

11. Mears, R. J.; Reekie, L.; Jauncey, I. M.; Payne, D. N. Low-noise erbium-doped fibre amplifier operating at 1.54 μm. *Electron. Lett.* **1987**, *23*, 1026.

12. Shriver, D.; Atkins, P. Lanthanides. In *Inorganic Chemistry*W.H. Freeman and Company: New York, 1999; pp 321.

13. Jensen, W. B. The Positions of Lanthanum (Actinium) and Lutetium (Lawrencium) in the Periodic Table. *J. Chem. Educ.* **1982**, *59*, 634.

14. House, J. E. The Lanthanides. In *Inorganic Chemistry*Elsevier Inc.: Oxford, 2013; pp 367.

15. Cotton, S. *Lanthanide and Actinide Chemistry;* John Wiley & Sons, Ltd: West Sussex, 2006; , pp 9-14,68-69.

16. Friedmann Jr., H. G.; Choppin, G. R.; Feuerbacher, D. G. The Shapes of the *f* Orbitals. *J. Chem. Educ.* **1964**, *41*, 357.

17. Housecroft, C. E.; Sharpe, A. G. The *f*-block metals: lanthaniudes and actinoids; *d*-Block metal chemistry:general considerations. In *Inorganic Chemistry*Pearson Education Limited: Harlow, 2012; pp 1002-646.

18. McDaniel, D. H. Spin Factoring as an Aid in the Determination of Spectroscopic Terms. *J. Chem. Educ.* **1977**, *54*, 147.

19. Herzberg, G. *Atomic Spectra and Atomic Structure;* Dover: New York, 1994; , pp 38-96,135.

20. Martin, W. C.; Zalubas, R.; Hagan, L. Atomic Energy Levels - The Rare-Earth Elements. *Nat. Stand. Ref. Data. Ser.* **1978**, *20*, 149.

21. Jackson, S. D. The spectroscopic and energy transfer characteristics of rare earth ions used for silicate glass fibre lasers operating in the shortwave infrared. *Laser Photonics Rev.* **2009**, *3*, 466.

22. Watekar, P. R.; Ju, S.; Han, W. A Small-Signal Power Model for Tm-Doped Silica-Glass Optical Fiber Amplifier. *IEEE Photon. Technol. Lett.* **2006**, *18*, 2035-2037.

23. Bethe, H. Splitting of terms in crystals. *Ann. Phys.* **1929**, *3*, 133.

24. Figgis, B. N.; Hitchman, M. A. Introduction. In *Ligand Field Theory and Its Applications*Wiley-VCH: Canada, 2000; pp 1.

25. Shriver, D.; Atkins, P. Bonding and Electronic Structure. In *Inorganic Chemistry*W.H. Freeman and Company: New York, 1999; pp 227.

26. Karraker, D. G. Coordination of Trivalent Lanthanide Ions. *J. Chem. Educ.* **1970**, *47*, 424.

27. Burns, R. G. Outline of crystal field theory. In *Mineralogical Applications of Crystal Field Theory*Cambridge University Press: Cambridge, 2005; pp 7.

28. Dorenbos, P. The 4fnâ†"4f n-15d transitions of the trivalent lanthanides in halogenides and chalcogenides. *J. Lumin.* **2000**, *91*, 91-106.

29. Dorenbos, P. The 5d level positions of the trivalent lanthanides in inorganic compounds. *J. Lumin.* **2000**, *91*, 155-176.

30. Carnall, W. T. The near-infrared transitions of the trivalent lanthanides in solution. II. Tb^{3+}, Dy^{3+}, Ho^{3+}, Er^{3+}, Tm^{3+}, and Yb^{3+}. *J. Phys. Chem* **1962**, *67*, 1206-1211.

31. Dorenbos, P. Crystal field splitting of lanthanide 4f(n-1)5d-levels in inorganic compounds. *J. Alloys Compounds* **2002**, *341*, 156-159.

32. Carnall, W. T.; Fields, P. R. Lanthanide and Actinide Absorption Spectra in Solution. *Adv. Chem. Ser.* **1967**, *71*, 86-101.

33. Hatanaka, M.; Yabushita, S. Theoretical Study on the f-f Transition Intensities of Lanthanide Trihalide Systems. *J. Phys. Chem. A* **2009**, *113*, 12615.

34. Judd, B. R. Hypersensitive Transitions in Rare-Earth Ions. *J. Chem. Phys.* **1966**, *44*, 839.

35. Judd, B. R. Optical Absorption Intensities of Rare-Earth Ions. *Phys. Rev.* **1962**, *127*, 750.

36. Kauzmann, W. The adsorption of light by bound electrons. In *Quantum Chemistry: An Introduction*Academic Press Inc.: London, 1957; pp 577.

37. Broer, L. J. F.; Gorter, C. J.; Hoogschagen, J. On the Intensities and the Multipole Character in the Spectra of the Rare Earth Ions. *Physica* **1945**, *11*, 231.

38. Gruen, D. M.; DeKock, C. W.; McBeth, R. L. Electronic Spectra of Lanthanide Compounds in the Vapor Phase. *Adv. Chem. Ser.* **1967**, *71*, 102-121.

39. Carnall, W. T.; Fields, P. R.; Wybourne, B. G. Spectral Intensities of the Trivalent Lanthanides and Actinides in Solution. I. Pr^{3+}, Nd^{3+}, Er^{3+}, Tm^{3+}, and Yb^{3+}. *J. Chem. Phys.* **1962**, *42*, 3797.

40. Cartner, J. N.; Smart, R. G.; Hanna, D. C.; Tropper, A. C. Lasing and amplication in the 0.8 μm region in thulium-doped fluorozirconate fibers. *Electron. Lett.* **1990**, *26*, 1759.

41. Seybold, P. G. QSPR Analysis of Solvent Effects on the Decay of the $^1\Delta_g$ State of Molecular Oxygen. *Internet Electron. J. Mol. Des.* **2006**, *5*, 479.

APPENDIX B

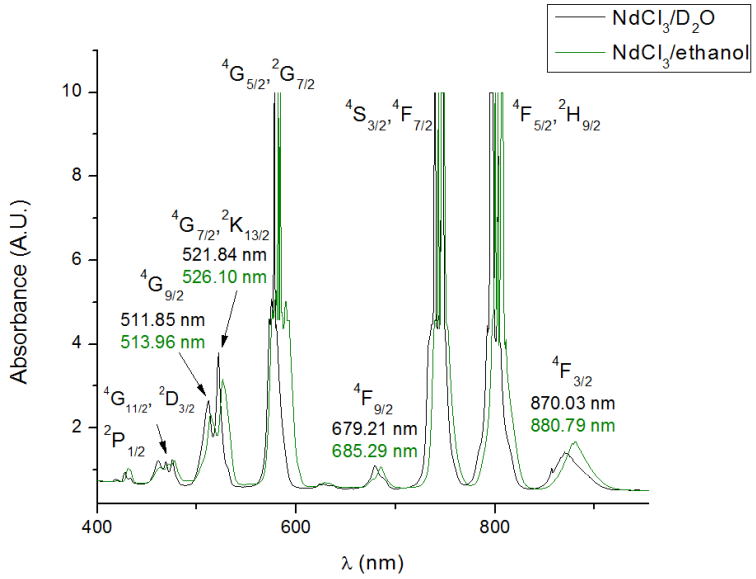

Figure B.1 Absorbance spectrum of $NdCl_3$.

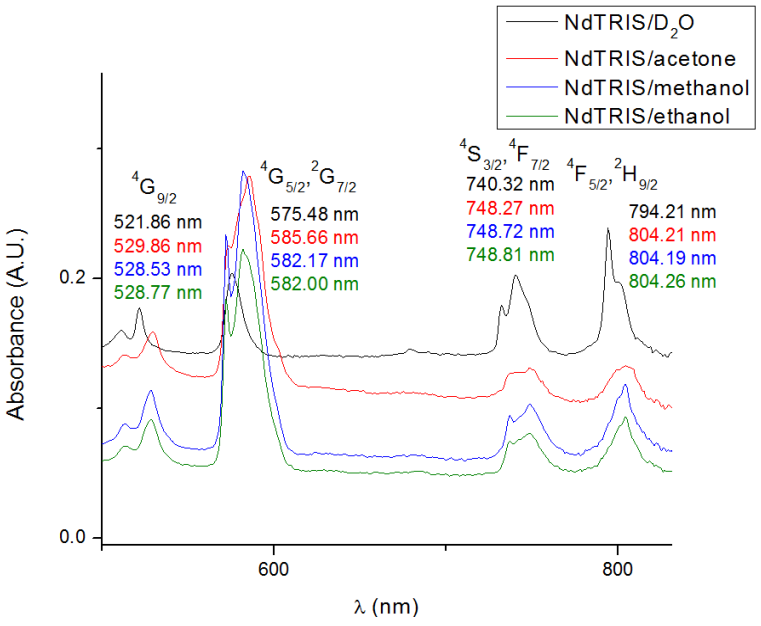

Figure B.2 Absorbance spectrum of NdTRIS.

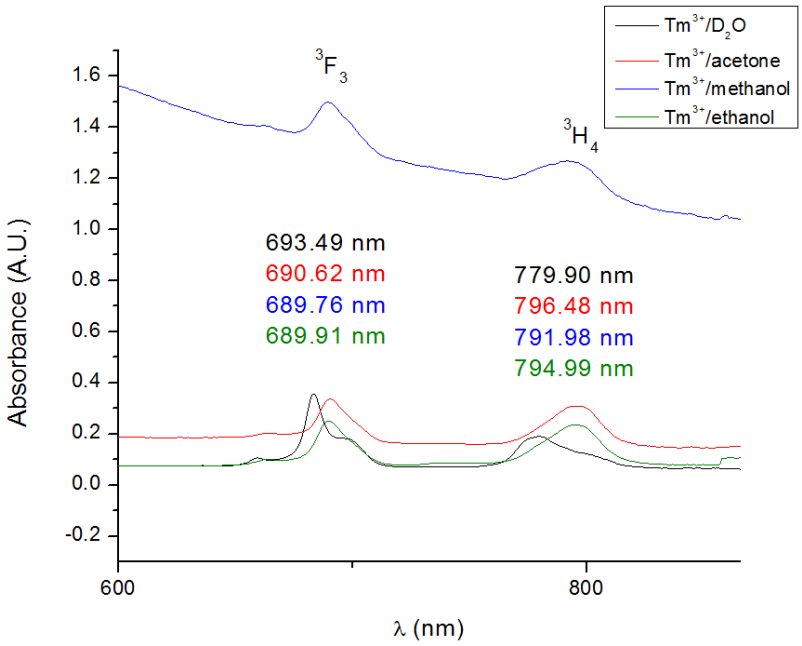

Figure B.3 Absorbance spectrum of Tm^{3+}.

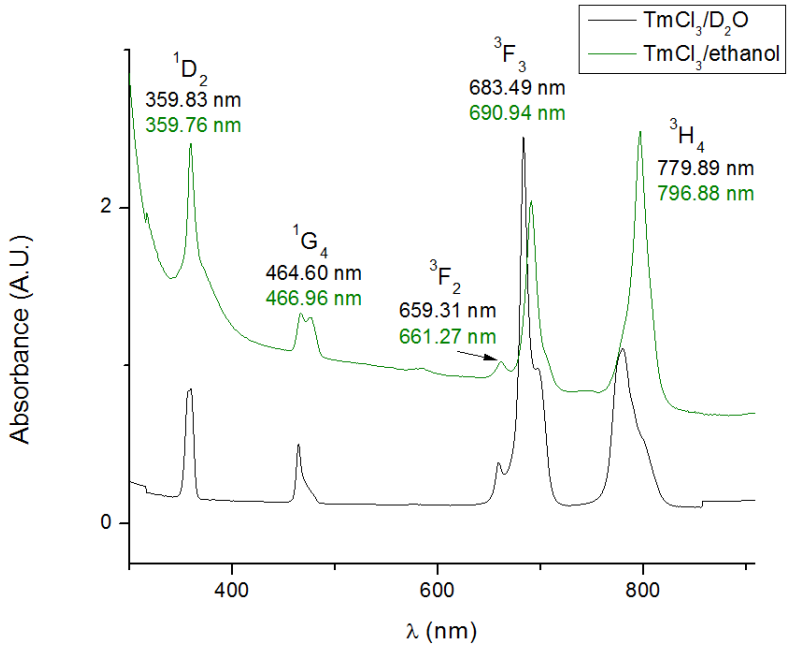

Figure B.4 Absorbance spectrum of $TmCl_3$.

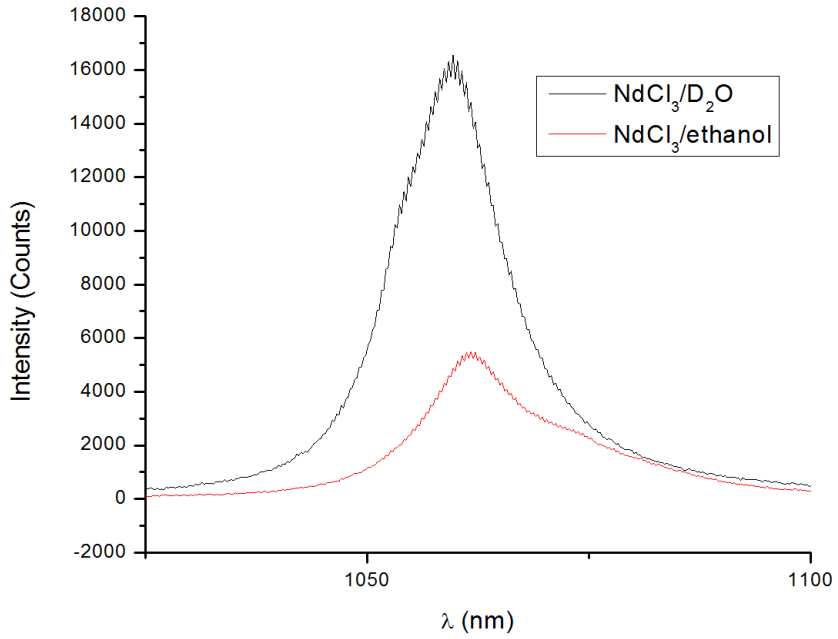

Figure B.5 Fluorescence spectrum of $NdCl_3$.

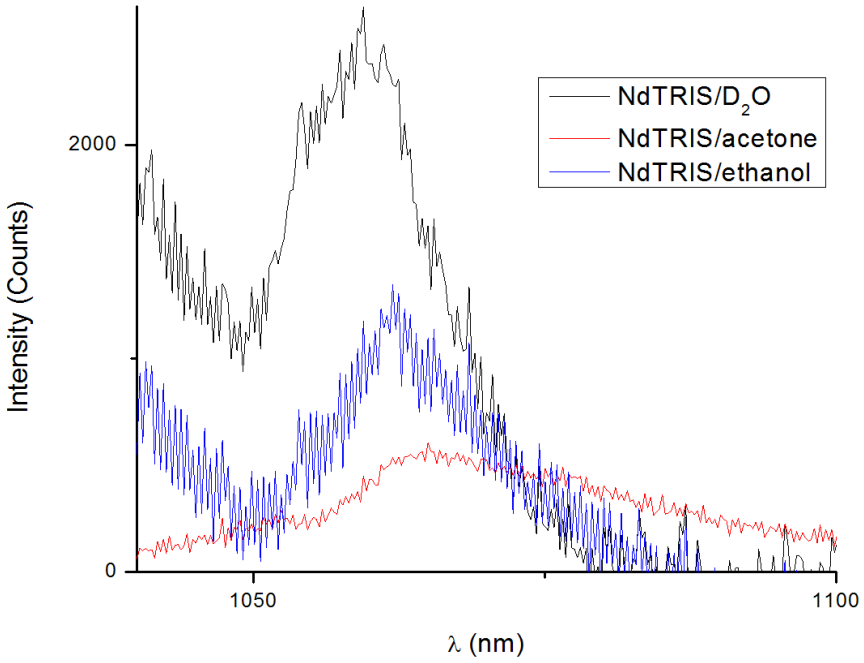

Figure B.6 Fluorescence spectrum of NdTRIS.

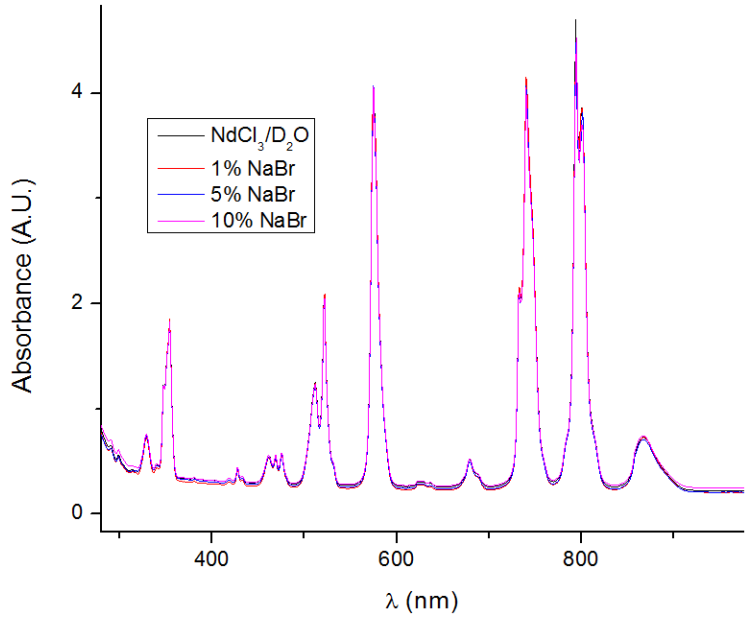

Figure B.7 Absorbance spectrum of NaBr $NdCl_3/D_2O$ solution.

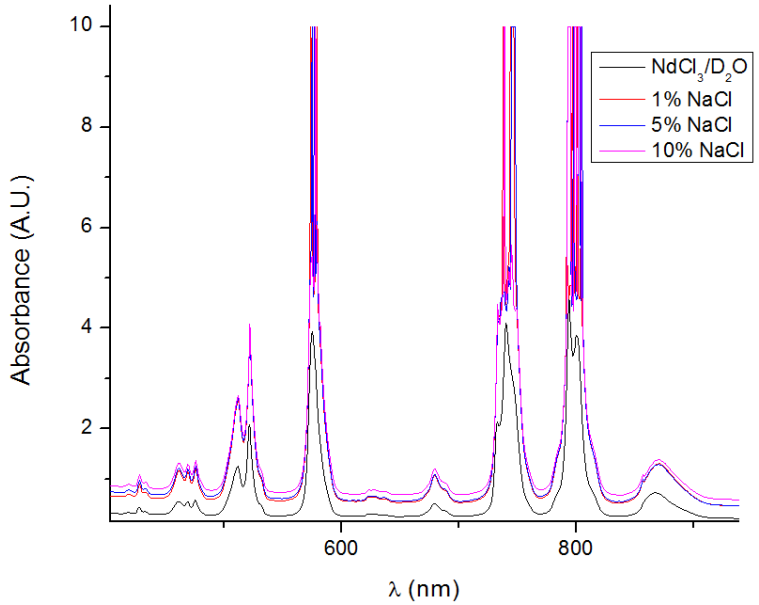

Figure B.8 Absorbance spectrum of NaCl $NdCl_3/D_2O$ solution.

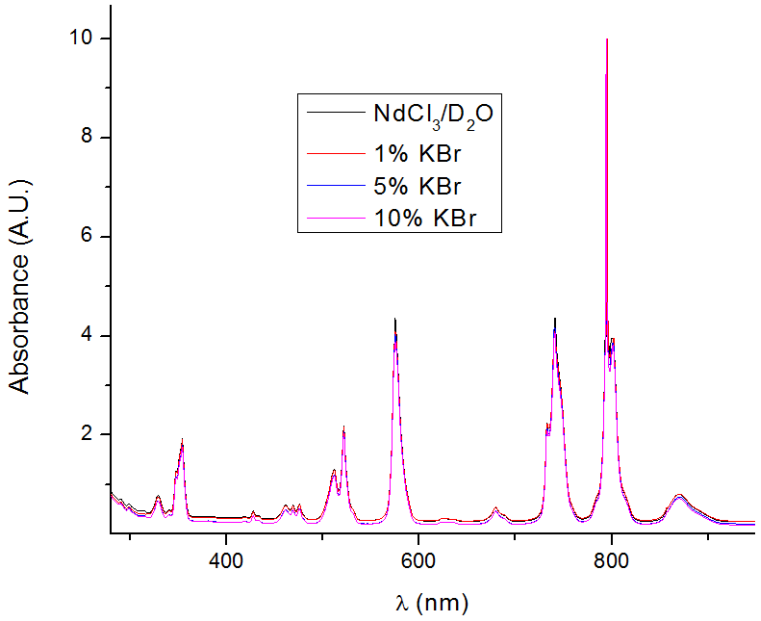

Figure B.9 Absorbance spectrum of KBr $NdCl_3/D_2O$ solution.

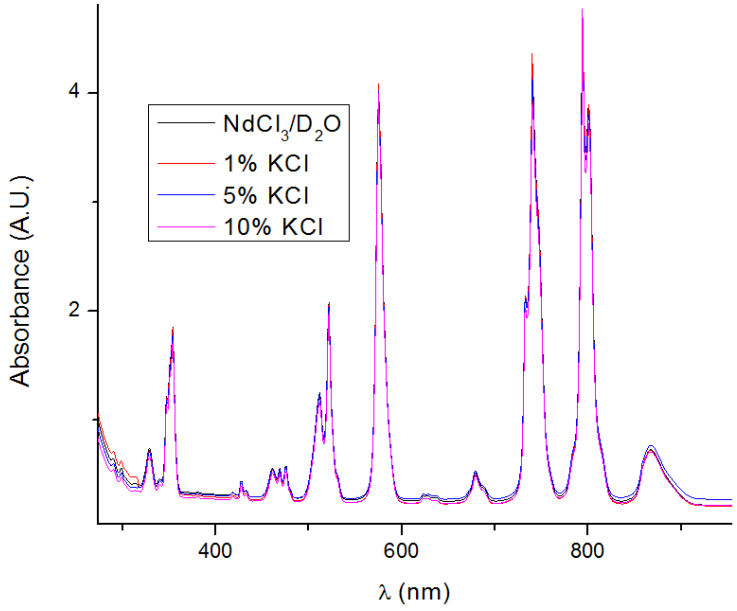

Figure B.10 Absorbance spectrum of KCl $NdCl_3/D_2O$ solution.

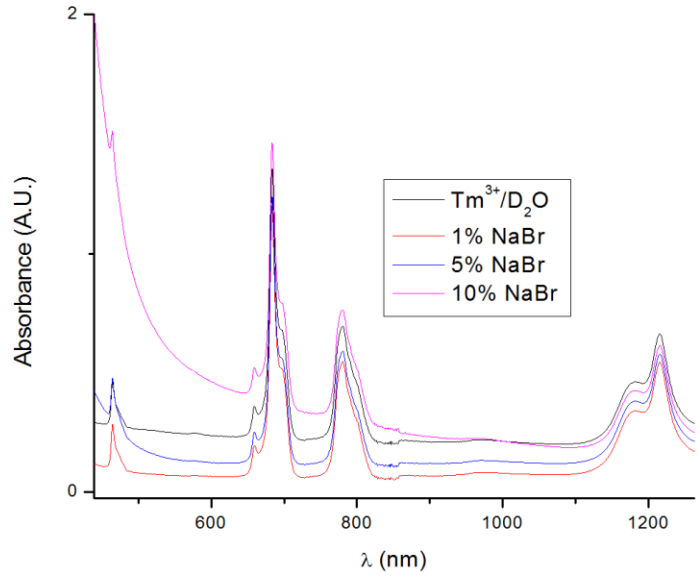

Figure B.11 Absorbance spectrum of NaBr Tm^{3+}/D_2O solution.

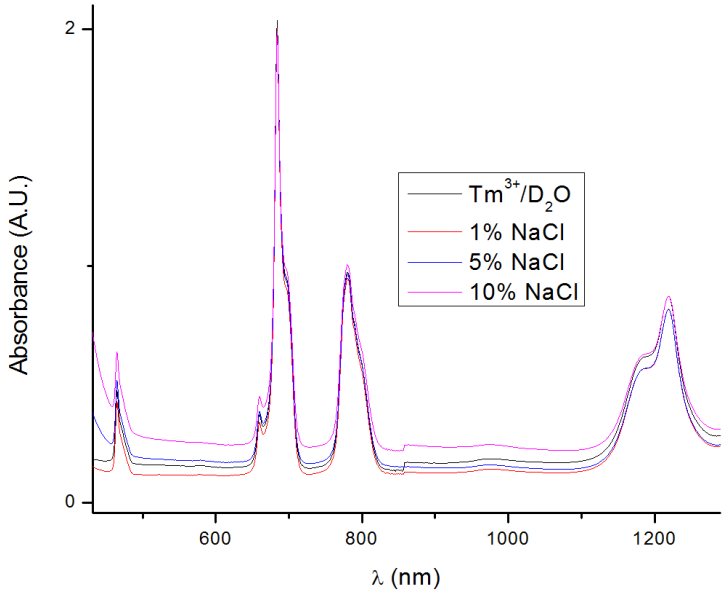

Figure B.12 Absorbance spectrum of NaCl Tm^{3+}/D_2O solution.

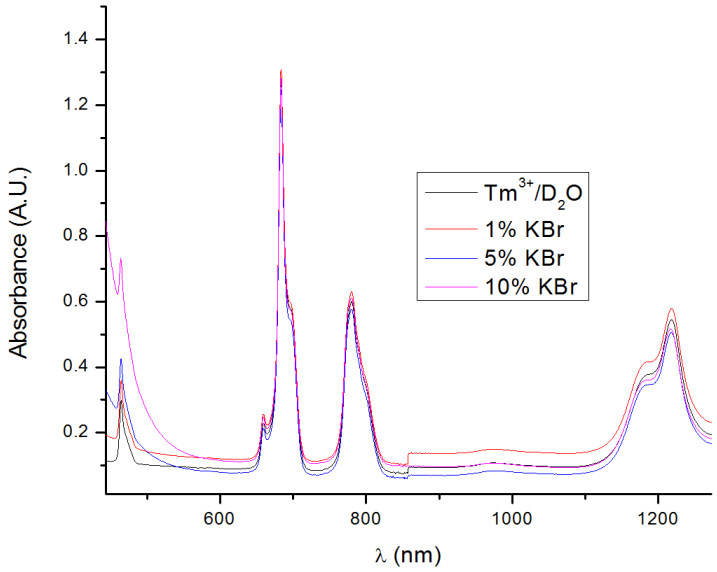

Figure B.13 Absorbance spectrum of KBr Tm^{3+}/D_2O solution.

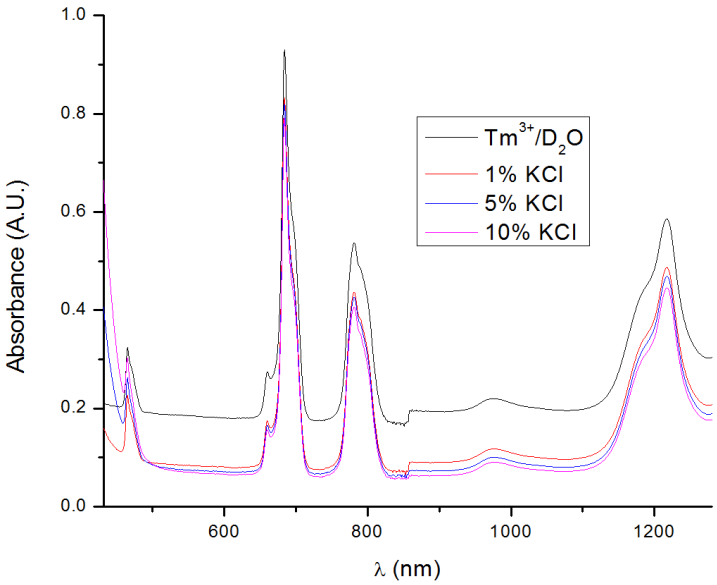

Figure B.14 Absorbance spectrum of KCl Tm^{3+}/D_2O solution.

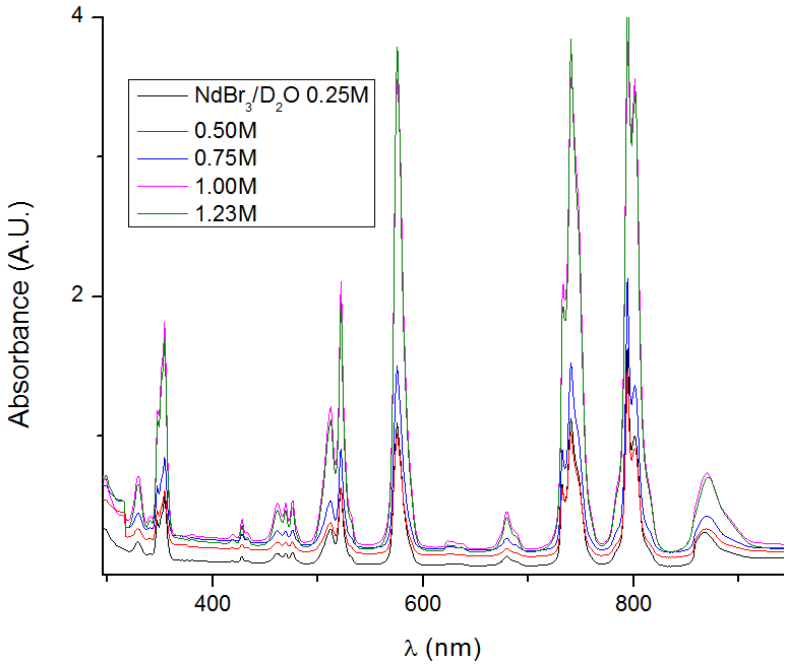

Figure B.15 Absorbance spectrum of $NdBr_3/D_2O$ solutions at varying concentrations.

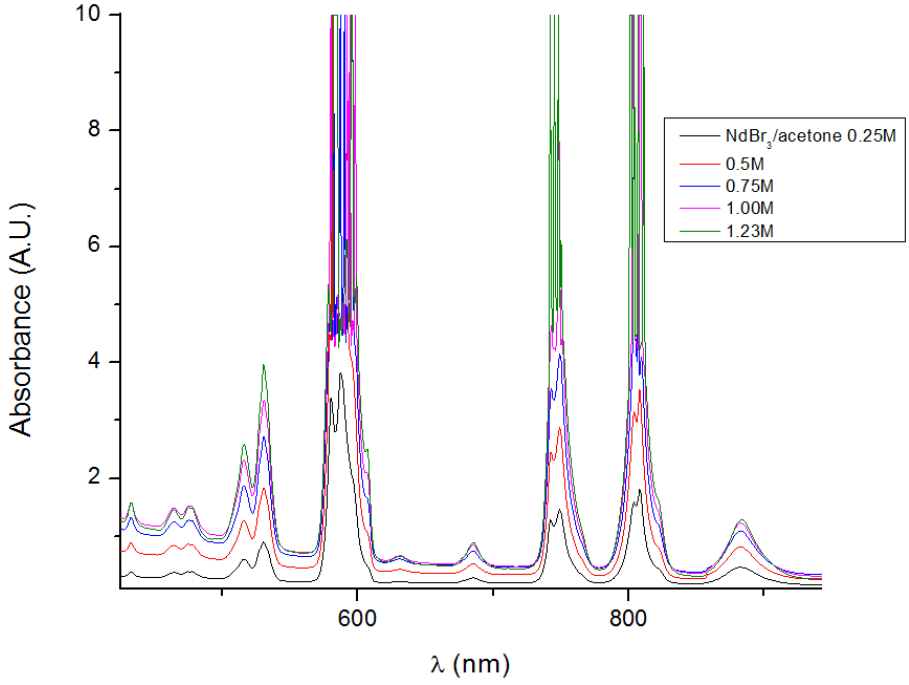

Figure B.16 Absorbance spectrum of $NdBr_3$/acetone solutions at varying concentrations.

Chapter 3: Ar*+He Potential Energy Curves Computation

3.1 Introduction

I. Rare Gas Lasers

Within the past decade, diode pumped alkali lasers (DPALs) have been of interest. The first DPAL, created by Krupke *et. al*. in 2003, was a Rubidium (Rb) laser, lasing at the 795 nm on the $^2P_{1/2} \rightarrow {}^2S_{1/2}$ transition[1]. DPALs use an alkali gas, along with a buffer gas to increase the rates of collisional spin-orbit transitions. Alkali gases have been chosen for lasing systems due to their high quantum efficiency, high power, and simplicity[2]. However, due to an unpaired electron in the valence *s* orbital, alkali gases are also highly reactive[3], leading to damage to the laser system. Recently, rare gas (Rg) lasers have been employed, due to efficiency and power similarities to DPALS and due to the non-reactivity of the rare gas, minimizing damage to the laser optics.

DPALs and rare gas lasers are three level laser systems. Pumping occurs, carrying the electrons to a higher energy level, which then collisionally relaxes down to a lower energy level[3]. From that level, lasing then occurs, bringing the medium to starting level. The first step in modeling a laser system is to study the energy levels of the active medium. Different labeling schemes are used for the energy levels that are involved in the pumping and lasing processes of the alkali gases. The most commonly used notations for atomic states are term symbols, Racah notation, and Paschen notation. These will now be described.

II. Atomic Term Symbols

Russel-Sanders Coupling Term Symbols

The energy state of an atom can be defined in terms of its electronic or orbital angular momentum, electronic spin angular momentum, and total angular momentum[4]. The orbital angular momentum of each electron is represented by the azimuthal quantum number *l* where the total electronic angular momentum *L* is a vector summation of the orbital angular momentum of each electron, represented by l_i, due to the coupling between the different electrons. For an atom with two unpaired electrons the total electronic angular momentum quantum number is given by $L = l_1 + l_2,\quad l_1 + l_2 - 1,\quad \cdots,\quad |l_1 - l_2|$, and the magnitude of the total electronic angular momentum is $|L| = \sqrt{L(L+1)} \cdot \hbar$. In the same way, the total electron spin angular momentum *S* of the atom is a vector summation of the individual spins s_i of electrons, resulting from coupling between s_i values. For an atom with two unpaired electrons the total electron spin angular momentum quantum number is $S = s_1 + s_2,\quad s_1 + s_2 - 1,\ \cdots,\ |s_1 - s_2|$ and the magnitude of the total spin angular momentum is $|S| = \sqrt{S(S+1)} \cdot \hbar$. Coupling of the resultant total spin angular momentum, *S*, and the resultant total electronic angular momentum, *L*, is known as Russell-Saunders coupling, and the vector summation of *L* and *S* yields the total angular momentum quantum number, *J*, according to Eq. (1) below.[4]

$$J = (L+S), (L+S-1), (L+S-2), \ldots, |L-S| \qquad (1)$$

A term symbol that takes into account Russel-Saunders coupling is written as

$$^{2S+1}L_J \quad (2)$$

where the quantity (2*S*+1) is referred to as the spin multiplicity. The electronic angular momentum symbol *L* is written as *S*,*P*,*D*,*F*… based on its corresponding numeric value *L* = 0,1,2,3…, respectively. Based on the value of the spin multiplicity, the atomic state is referred to as a singlet, doublet, triplet, etc[4]. For example, the term symbol of a singlet state (S=0) with L=1 and J=1 is written as $^1P_1$.

Paschen and Racah Notation

Atoms do not remain in their ground states but are often excited to high energy levels and configurations. Typically, an asterisk is used with an element notation to convey that the atom is in an excited state (i.e. X*).Term symbols can also be used to denote excited states but Racah and Paschen notation are more commonly used in laser physics to describe these excited states. In Racah notation, the excited state is described in terms of the "parent ion core" and the excited electron. The parent ion core is simply the electronic configuration of the non-excited electrons; that is, it is the ground state configuration without one electron[5]. For example, neon (Ne) has the ground state configuration $1s^2 2s^2 2p^6$. When one electron from the 2p orbital is excited to the 3s orbital, Ne has the configuration $1s^2 2s^2 2p^5 3s^1$. For this excited configuration, the parent ion core would contain all electrons except the electron in the 3s orbital. Therefore, the parent ion core would have a configuration of $1s^2 2s^2 2p^5$. Excited electron configurations are written in Racah notation as[5]

$$(^{2S+1}L_J)nl[K]_J \quad (3)$$

where ($^{2S+1}L_J$) denotes the parent ion, while the excited electronic configuration is given by nl[K]$_J$, where n is the principal quantum number of the excited electron, and l is the orbital angular momentum of the excited electron given by *s,p,d,f*… Russell-Saunders notation is used for the parent ion, due to large spin-orbit interaction[6]. The electrostatic interaction between the excited electron and the core is strong compared to the coupling of the spin of the electron to the core. This results in a new vector, K, occurring from the coupling of the total angular momentum J_{core} of the parent ion and the orbital angular momentum l of the excited electron[6]. K is given by[5]

$$K = (J_{core} + l_{excited}) + (J_{core} + l_{excited} - 1) \dots |J_{core} - l_{excited}| \quad (4)$$

The subscript J of the bracket does not refer to the same J of the parent ion but rather a new J that arises from the coupling of K to the spin s of the outer electron[6]. Since the outer electron always has a spin of ½, the subscript J can be defined as[5]

$$J = K \pm \frac{1}{2} \quad (5)$$

Typically, *j-l* coupling which results in K, differs from *j-j* coupling but when the excited electron occupies an *s* orbital, the *j-l* and *j-j* coupling are identical[5].

II. Excited Electron Configurations

Ne* Configurations

The ground state of Ne, $1s^2 2s^2 2p^6$, results in a term symbol of $^1S_0$, due to no orbital angular momentum ($L = 0$), no unpaired electrons ($S = 0$), and a lack of total angular momentum ($J = 0$). In Ne, the parent ion has one *p* electron missing from a closed shell and so the term diagram of the ion is the same as if it had only one *p* electron

except that terms will be inverted in energy. The parent ion core thus has levels $^2P_{1/2}$ and $^2P_{3/2}$. According to Hund's rules (#3), for atoms with less than half-filled shells, the level with the lowest value of *J* lies lowest in energy. When the shell is more than half full, the opposite rule holds (highest *J* lies lowest), i.e., term symbols with higher *J* values lie lower in energy[4]. Therefore, the $^2P_{3/2}$ level will lie deeper than the $^2P_{1/2}$ level. When an electron from *2p* is excited into the *3s* orbital ($2p^5 3s^1$ electronic configuration) the $^2P_{3/2}$ parent ion core state has a total angular momentum $J = {}^3/_2$ and the outer electron has an orbital angular momentum $l = 0$. Therefore $K = {}^3/_2$. Since $J = K \pm ½$, a *K* value of $^3/_2$ corresponds to *J* values of 2 and 1. This can also be seen with the parent ion core state of $^2P_{1/2}$. *K* has a value of ½ since the ion core has a *J* value of ½ and the excited electron has no angular momentum *l*. The resulting *J* values for *K* are 1 and 0. Therefore, four states arise from this configuration, as is shown in Table 3.1.1.

Table 3.1.1 Racah term values for the $1s^2 2s^2 2p^5 3s^1$ configuration of Ne*.

$(^{2S+1}L_J)$	$(^{2S+1}L_J)nl$	[K]	J
$(^2P_{3/2})$	$(^2P_{3/2})3s$	3/2	2,1
$(^2P_{1/2})$	$(^2P_{1/2})3s$	1/2	1,0

For an excited p electron in Ne*, there are 10 states, six for the parent ion in the $^2P_{3/2}$ state and four for the parent in the $^2P_{1/2}$ state. For the parent ion in the $^2P_{3/2}$ state, $J = {}^3/_2$ and l=1. Using Eqn. (4), $K = {}^5/_2$, $^3/_2$, and $^1/_2$ which gives rise to *J* values of 3, 2, 2, 1, 1 and 0. This results in term designations of $np[5/2, 3/2, 1/2]_{3, 2, 2, 1, 1, 0}$. For the parent ion in the $^2P_{1/2}$ state, the four excited states are $np[3/2,1/2]_{2,1,1,0}$. Table 3.1.2 shows the elements of Racah notation for a Ne* electron configuration of $1s^2 2s^2 2p^5 3p^1$.

Table 3.1.2 Racah term values for the $1s^2 2s^2 2p^5 3p^1$ configuration of Ne*.

$(^{2S+1}L_J)$	$(^{2S+1}L_J)nl$	[K]	J
$(^2P_{3/2})$	$(^2P_{3/2})3p$	5/2, 3/2, 1/2	3,2,2,1,1,0
$(^2P_{1/2})$	$(^2P_{1/2})3p$	3/2, 1/2	2,1,1,0

Typically, Racah notations are written without the parent ion core term symbol, only writing the principal quantum number *n*, orbital angular momentum *l*, [*K*], and *J* values of the excited electron[2]. Also, the lower energy levels are denoted by *nl*'..

In Paschen notation, excited electron states are also labeled as ns_m, np_m, nd_m, and nf_m states but these labels do not necessarily refer to orbital angular momentum *l* values principal quantum numbers *n* of the energy state[77]. The subscript *m* refers to the number of the energy level within its *ns*, *np*, *nd*, or *nf* group. There are four energy levels in an *ns* group and these energy levels are numbered ns_2 through ns_5, with ns_2 having the highest energy and ns_5 having the lowest energy. The ns_1 notation is not used to denote an excited sate as it is reserved for the ground state. The *np*, *nd*, and *nf* levels have 10, 10, and 14 sublevels, respectively.

The first excited available energy level is denoted *1s*, with the *np*, *nd*, and *nf* orbitals that are filled after the first *ns* excited level denoted as *2p*, *3d*, and *4f*. The next excited *ns* series is labelled as *2s*, with its following *np*, *nd*, and *nf* orbitals *3p*, *4d*, and *5f* and so on. Generally, p→s and s→p transitions are allowed but s→s and p→p transitions are forbidden[8]. Figure 3.1.1 is an energy diagram, showing different excited energy levels[9,10] of Ne*, with their corresponding Paschen notation.

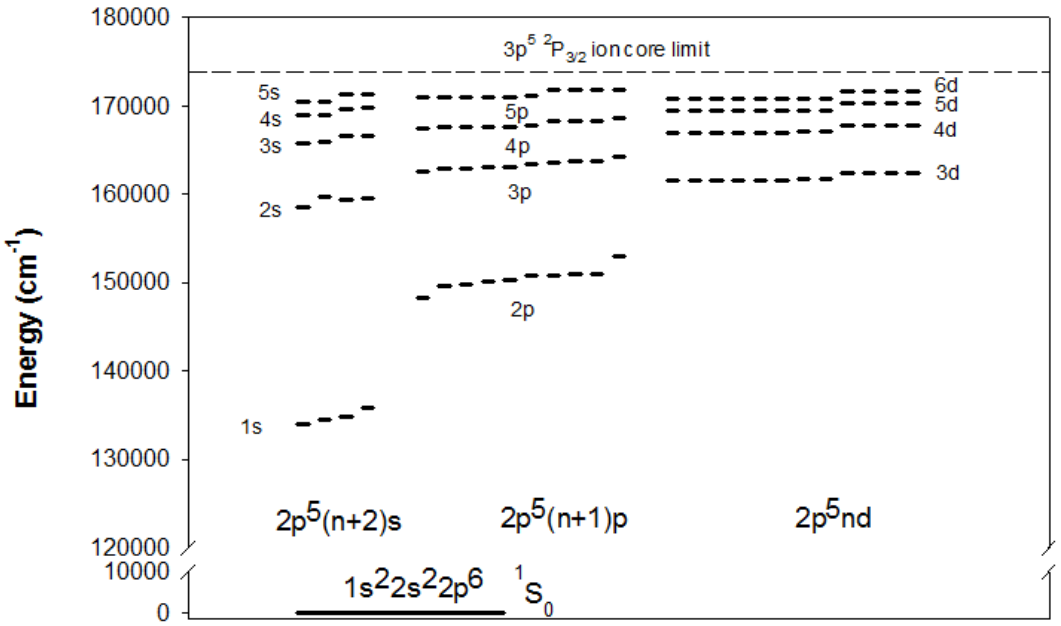

Figure 3.1.1 Energy level diagram of Ne*.

Table 3.1.3 gives the term symbols, Racah, and Paschen notation for two configurations of Ne*.

Table 3.1.3 Term symbols, inner core terms, Paschen, and Racah notation for the $3s^1$ and $3p^1$ configurations of Ne*. Term symbols do not directly correspond to Racah/Paschen notations in same row.

Configuration	Term Symbol ($^{2S+1}L_J$)	Inner Core Term Symbol ($^{2S+1}L_J$)	Paschen Notation	Racah Notation
$1s^2 2s^2 2p^5 3s^1$	$^1P_{1,u}$	($^2P_{1/2}$)	$1s_2$	$3s'[1/2]_0$
	$^3P_{0,u}$		$1s_3$	$3s'[1/2]_1$
	$^3P_{1,u}$	($^2P_{3/2}$)	$1s_4$	$3s[3/2]_1$
	$^3P_{2,u}$		$1s_5$	$3s[3/2]_2$
$1s^2 2s^2 2p^5 3p^1$	$^1S_{0,g}$	($^2P_{1/2}$)	$2p_1$	$3p'[1/2]_0$
	$^1P_{1,g}$		$2p_2$	$3p'[1/2]_1$
	$^1D_{2,g}$		$2p_3$	$3p'[3/2]_1$
	$^3S_{1,g}$		$2p_4$	$3p'[3/2]_2$
	$^3P_{2,g}$	($^2P_{3/2}$)	$2p_5$	$3p[1/2]_0$
	$^3P_{1,g}$		$2p_6$	$3p[1/2]_1$
	$^3P_{0,g}$		$2p_7$	$3p[3/2]_1$
	$^3D_{3,g}$		$2p_8$	$3p[3/2]_2$
	$^3D_{2,g}$		$2p_9$	$3p[5/2]_2$
	$^3D_{1,g}$		$2p_{10}$	$3p[5/2]_3$

Ar* Configurations

Argon (Ar) is a noble gas with a $1s^2 2s^2 2p^6 3s^2 3p^6$ ground state configuration. Like Ne, the ground state term symbol is $^1S_0$, due to a lack of unpaired electrons ($S = 0$), orbital angular momentum ($L = 0$), and total angular momentum ($J = 0$). The first configuration of Ar* is $1s^2 2s^2 2p^6 3s^2 3p^5 4s^1$, with the parent ion core having a $1s^2 2s^2 2p^6 3p^5$ configuration. The parent ion core of Ar* has the same term symbols ($^2P_{3/2}$, $^2P_{1/2}$) as Ne*, as the only different in the parent ion cores of these two excited noble gas is the outermost principal quantum number. Therefore, the only difference in the Racah notation between Ne* and Ar* will be the *nl* values of the excited electron.

Table 3.1.4 Racah term values for the $1s^2 2s^2 2p^6 3s^2 3p^5 4s^1$ configuration of Ar*.

$(^{2S+1}L_J)$	$(^{2S+1}L_J)nl$	[K]	J
$(^2P_{3/2})$	$(^2P_{3/2})4s$	3/2	2,1
$(^2P_{1/2})$	$(^2P_{1/2})4s$	1/2	1,0

Table 3.1.5 Racah tern values for the $1s^2 2s^2 2p^6 3s^2 3p^5 4p^1$ configuration of Ar*.

$(^{2S+1}L_J)$	$(^{2S+1}L_J)nl$	[K]	J
$(^2P_{3/2})$	$(^2P_{3/2})4p$	5/2,3/2,1/2	3,2,2,1,1,0
$(^2P_{1/2})$	$(^2P_{1/2})4p$	3/2,1/2	2,1,1,0

Figure 3.1.2 shows the energy diagram of Ar* with energy states[11,12] with their Paschen notation.

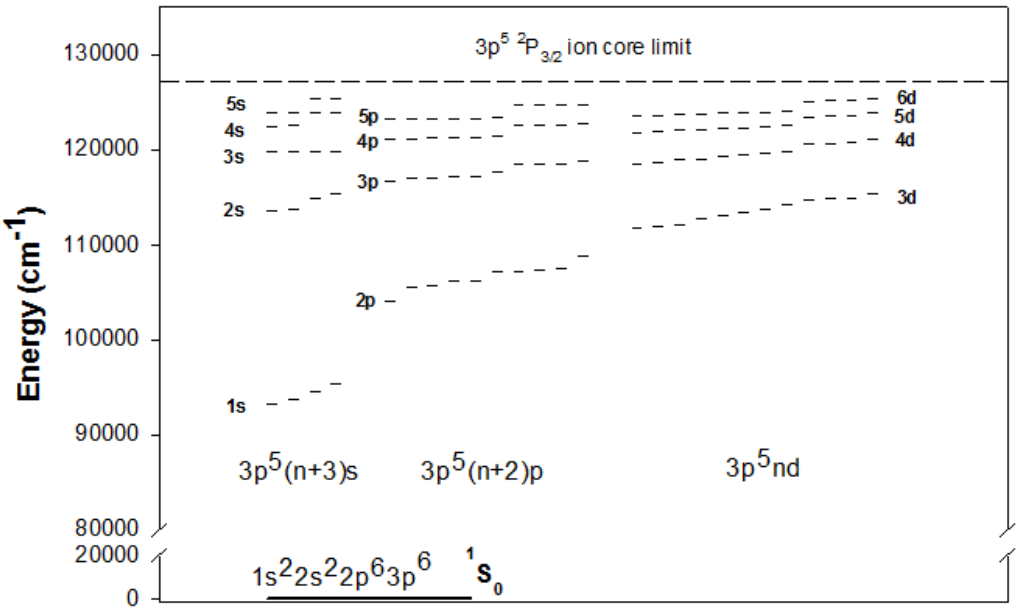

Figure 3.1.2 Energy level diagram of Ar*.

Table 3.1.6 gives the term symbols, Paschen, and Racah notation for three Ar* configurations.

Table 3.1.6 Term symbols, inner core terms, Paschen, and Racah notation for the $4s^1$, $4p^1$, and $3d^1$ configurations of Ar*. Term symbols do not directly correspond to Racah/Paschen notations in same row.

Configuration	Term Symbol ($^{2S+1}L_J$)	Inner Core Term Symbol ($^{2S+1}L_J$)	Paschen Notation	Racah Notation
$1s^2 2s^2 2p^6 3s^2 3p^5 4s^1$	$^1P_{1,u}$	($^2P_{1/2}$)	$1s_2$	$4s'[1/2]_0$
	$^3P_{0,u}$		$1s_3$	$4s'[1/2]_1$
	$^3P_{1,u}$	($^2P_{3/2}$)	$1s_4$	$4s[3/2]_1$
	$^3P_{2,u}$		$1s_5$	$4s[3/2]_2$
$1s^2 2s^2 2p^6 3s^2 3p^5 4p^1$	$^1S_{0,g}$	($^2P_{1/2}$)	$2p_1$	$4p'[1/2]_0$
	$^1P_{1,g}$		$2p_2$	$4p'[1/2]_1$
	$^1D_{2,g}$		$2p_3$	$4p'[3/2]_1$
	$^3S_{1,g}$		$2p_4$	$4p'[3/2]_2$
	$^3P_{2,g}$	($^2P_{3/2}$)	$2p_5$	$4p[1/2]_0$
	$^3P_{1,g}$		$2p_6$	$4p[1/2]_1$
	$^3P_{0,g}$		$2p_7$	$4p[3/2]_1$
	$^3D_{3,g}$		$2p_8$	$4p[3/2]_2$
	$^3D_{2,g}$		$2p_9$	$4p[5/2]_2$
	$^3D_{1,g}$		$2p_{10}$	$4p[5/2]_3$

Helium

In DPAL and Rg laser systems, often the active medium is accompanied by a buffer gas. Rare gases are common choices for buffer gases since they are inert. Due to being the simplest rare gas, helium is the predominant choice as a buffer gas. Helium (He) is a two electron atom with a ground-state electronic configuration of $1s^2$. Due to a lack of orbital angular momentum and no unpaired electrons, resulting in a total electronic spin of zero, the ground-state term symbol for He is $^1S_0$. An electron can be excited to the 2s orbital, giving He* an electronic configuration of $1s^1 2s^1$. The orbital

angular momentum *l* of both orbitals is zero and the total spin can be zero or one. This results in term symbols of $^3S_1$ and $^1S_0$.

Table 3.1.7 Term symbols of He and He*.

Configuration	Term Symbol ($^{2S+1}L_J$)
$1s^2$	$^1S_0$
$1s^12s^1$	$^3S_1$
	$^1S_0$

IV. Molecular Term Symbols and Molecular States

As with atomic states, term symbols can be written also for molecular states. In the case of diatomics, the chemical system has two nuclei, which introduce two new quantum numbers [13], Λ and Σ. The orbital angular momentum quantum number, Λ, corresponds to the orbital angular momentum projected along the internuclear axis. Λ can have values of 0,1,2… which correspond to symbols Σ, Π, Δ, etc., which are written in place of Λ. The spin angular momentum quantum number Σ corresponds to the spin angular momentum vector projected along the internuclear axis. Σ values of 0, ½ and 1 are associated with singlet, doublet and triplet molecular states. The following is a general form for molecular term symbols,

$$^{2\Sigma+1}\Lambda_{g/u} \tag{6}$$

The *g/u* notation refers to the symmetry of the wavefunction with respect to the inversion of the center of the molecule, also known as the parity of the molecule. If the wavefunction is symmetric with respect to the center of inversion, *gerad* (*g*) is used. If the wavefunction is antisymmetric, *ungerad* (*u*) is used[13]. The parity[14], P, can be determined by the sum of the angular momentum l_i of each electron,

$$P = -1^{\sum_i l_i} \quad (7)$$

Odd summations correspond to *u* parity where even summations correspond to *g* parity.

Atomic states can combine together to form molecular states. Orbital angular momentum (L) and spin multiplicities (2S+1) of atomic states dictate what molecular states arise from the combination. States with no internuclear axial angular momentum, $\Lambda = 0$ (Σ states), always arise in odd numbers. Herzberg details the resulting molecular term symbols from the addition of atomic term symbol combinations. For example, two S atomic states form a Σ molecular state while an S and D atomic states form Σ, Π, and Δ molecular states[15]. Spin multiplicities of molecular states arise from spin multiplicities of atomic states. The resulting combinations are shown in Table 3.1.8.

Table 3.1.8 Multiplicities of molecular electron states for given multiplicities of the separated atoms.

Separated Atoms	**Molecule**
Singlet + Singlet	Singlet
Singlet + Doublet	Doublet
Singlet + Triplet	Triplet
Doublet + Doublet	Singlet, Triplet
Doublet + Triplet	Doublet, Quartet
Doublet + Quartet	Triplet, Quintet
Triplet + Triplet	Singlet, Triplet, Quintet
Triplet + Quartet	Doublet, Quartet, Sextet
Quartet + Quartet	Singlet, Triplet, Quintet, Septet

Looking at a system with He and Ne*, it is apparent that the ground state He atom will combine with the excited Ne atom to form multiple molecular states, depending on the configuration of Ne*. These possibilities are listed in Table 3.1.9.

Table 3.1.9 Molecular states formed from He and Ne*.

He Atomic State	Ne* Electronic Configuration	Ne* Atomic State	Molecular Multiplicities	Molecular Term Symbols
$^1S_{0,g}$	$1s^2 2s^2 2p^5 3s^1$	$^1P_{1,u}$	Singlet	$^1\Sigma^+$, $^1\Pi$
		$^3P_{2,1,0,u}$	Triplet	$^3\Sigma^+$, $^3\Pi$
	$1s^2 2s^2 2p^5 3p^1$	$^1S_{0,g}$	Singlet	$^1\Sigma^+$
		$^1P_{1,g}$	Singlet	$^1\Sigma^-$, $^1\Pi$
		$^1D_{2,g}$	Singlet	$^1\Sigma^+$, $^1\Pi$, $^1\Delta$
		$^3S_{1,g}$	Triplet	$^3\Sigma^+$
		$^3P_{2,1,0,g}$	Triplet	$^3\Sigma^-$, $^3\Pi$
		$^3D_{3,2,1,g}$	Triplet	$^3\Sigma^+$, $^3\Pi$, $^3\Delta$
	$1s^2 2s^2 2p^5 3d^1$	$^1P_{1,u}$	Singlet	$^1\Sigma^+$, $^1\Pi$
		$^1D_{2,u}$	Singlet	$^1\Sigma^+$- $^1\Pi$, $^1\Delta$
		$^1F_{3,u}$	Singlet	$^1\Sigma^+$, $^1\Pi$, $^1\Delta$, $^1\Phi$
		$^3P_{2,1,0,u}$	Triplet	$^3\Sigma^+$, $^3\Pi$
		$^3D_{3,2,1,u}$	Triplet	$^3\Sigma^-$, $^3\Pi$, $^3\Delta$
		$^3F_{4,3,2,u}$	Triplet	$^3\Sigma^+$, $^3\Pi$, $^3\Delta$, $^3\Phi$

The aim of this research is to determine the energy levels of the *s* and *p* excited states of Ar*, along with the potential energy curves of the ground, *s*, and *p* states of Ar*+He. These calculations will be carried out by employing various basis sets and levels of theory, along with basis set corrections.

3.2 Experimental

I. Description of Computational Program

The $3p^5 4s^1$ and $3p^5 4p^1$ atomic energy levels of excited argon (Ar*) and molecular potential energy curves of Ar*-He were determined computationally using the software program Molpro®. To calculate energy levels, Molpro® requires a wavefunction "card" which defines the energy level in terms of the number of electrons, the group symmetry of the unpaired electrons, and the spin of the excited electron. Molpro® uses the highest possible group symmetry for the orbital occupations; D_{2h} and C_{2v} group symmetries are used for atomic and molecular systems, respectively. Each orbital is associated with an irreducible representation of the appropriate group symmetry. With D_{2h} symmetry, there are eight irreducible representations: A_g, B_{3u}, B_{2u}, B_{1g}, B_{1u}, B_{2g}, B_{3g}, and A_u. When expressing the symmetry in Molpro®, the numbers one through eight are used for the D_{2h} irreducible representations, starting with one for A_g and ending with eight for A_u. For atomic systems, *s* orbitals are represented by A_g, p_x with B_{3u}, p_y with B_{2u}, and p_z with B_{1u} and in Molpro® as 1, 2, 3, and 5, respectively. The symmetry of the system is determined by the product of the irreducible representations of the unpaired electrons. These products were determined by referring to group symmetry multiplication tables. For example, if an electron is excited from an *s* orbital into a p_x orbital, the wavefunction card uses the B_{3u} representation and therefore the number two to express the symmetry of the excited electron, as the product of A_g and B_{3u} is B_{3u}. The wavefunction card must also include the

spin of the excited unpaired electrons, in the form of "2*S*" where *S* is the total spin of the unpaired electrons. For triplet states, "2" is used to for the spin in the wavefunction card while "0" is used for singlet states. An example of a wavefunction card for a triplet state of Ar* in which an electron is excited from the $3p_x$ orbital into the 4s orbital is "wf, 20, 2, 2".

II. Computational Methods

Multiple basis sets and levels of theory were used in determining the energy levels of Ar*. The calculations used a Hartree-Fock (HF) determination of the triplet states. Then, the calculation was improved by using a multi configurational self-consistent field (mcscf) basis set, expressed in Molpro® as "multi", along with the wavefunction card. When using the mcscf level of theory, it was necessary to use an occupation card; without it, the calculation would include the singlet ground state energy with the excited state energies and this resulted in greatly lowered values for the Ar* energy levels. The occupation cards used expressed the number of occupied orbitals in terms of their irreducible representations. For the Ar* calculation, an occupation card of "occ,4,3,3,0,3,0,0,0" was used. After the mcscf calculation, one using configuration interaction (ci) theory was used, improving the values of the desired energy levels. Finally, a spin orbit (so) calculation was performed in the highest level of theory used. Energy values were converted from Hartree units to wavenumbers and reported along with their respective experimental values.

The first basis set employed was a double zeta (vdz) basis set. As this is a highly inaccurate basis set, triple, quadruple, and five zeta (vtz, vqz, v5z) basis sets were then employed. After this, all-valence double, triple, quadruple, and 5 zeta (avdz, adtz, adqz,

av5z) basis sets were used to increase the accuracy of the obtained energy levels. Finally, an extrapolation to the complete basis set limit (CBS) and a relativist correction using Douglas Kroll theory were employed to obtain the highest basis set accuracy possible. These basis sets and levels of theory were used to determine the ground state, the four *s* states, and ten *p* states of Ar*.

Originally, separate calculations were employed when determining the energies of the *s* singlet and triple states of Ar*. However, it was found that when determined in a single calculation, the *s* states energy values were closer to those of literature. A single calculation was used to determine all triplet and singlet *s* and *p* states. It was also determined that when increasing the active space of the electron configuration, higher accuracy was obtained. Previously, when occupied orbitals were specified, only the 3s, 3p, 4s, and 4p orbitals were open for occupation. This resulted in four A_g, three B_{3u}, three B_{2u}, and three B_{1u} orbitals. Therefore the occupation card was written as "occ, 4,3,3,0,3,0,0,0". However, when adding 5s and 5p orbitals to the occupied orbitals, the number of A_g, B_{3u}, B_{2u}, and B_{1u} orbitals increased by one, resulting in an occupation card of "occ, 5,4,4,0,4,0,0,0". By increasing the active space, the calculated values improved by 300-50 cm^{-1}, although the calculation itself was more expensive.

Molecular states energies of Ar*-He were calculated in the same way in which the Ar* energy levels were calculated. A wavefunction card with 20 electrons (2 accounting for He) was used with HF and mcscf calculations for all of the molecular potential curves arising from the ground state, s states, and p states of Ar*. Energies values were determined for an equilibrium bond length range of 0-20 Å.

3.3 Results and Discussion

I. Determined Ar* Energy Levels

Originally, separate calculations were used to determine the singlet and triplet *s* states of Ar*. The calculated energies, along with their respective literature values[11,12], are shown in Table 3.3.1.

Table 3.3.1 Calculated energy levels of the $3p^5 4s^1$ configuration of Ar*, using two separate calculations for the singlet and triplet energies.

Experimental Ground State Energy = 0.000 cm^{-1}								
	Transition	Method	Basis Set Energy (cm^{-1})					Experimental (cm^{-1})[11,12]
			AVDZ	AVTZ	AVQZ	CBS	Rel. Correction	
$3p^5 4s^1$	$^1S_0 \rightarrow {}^3P$	mrci	100876.60	100911.74	10022484	--	--	
		mrcid	98940.88	97730.91	96756.60	--	--	
		so	99783.17	98580.68	97610.96	96996.58	96717.67	95399.8329
			99362.02	98155.79	97183.78	96361.05	96064.50	94553.6705
			98772.41	97560.94	96329.42	95709.15	95401.14	93143.7653
	$^1S_0 \rightarrow {}^1P$	mrci	104091.80	103547.13	102432.19	98274.52	97998.23	95399.8329
		mrcid	102130.27	100330.67	98943.89			
		so	102130.27	100330.67	98943.89			

A single calculation was then used to determine all *s* and *p* Ar* states. The obtained energy values are shown in Table 3.3.2

Table 3.3.2 Calculated energy levels of the $3p^5 4s^1$ and $3p^5 4p^1$ configurations of Ar*, using a single calculation.

Experimental Ground State Energy = 0.00 cm^{-1}								
	Energy level	AVDZ	AVTZ	AVQZ	AV5Z	CBS	Rel Correction	Experimental (cm^{-1})[11,12] 93143.7653
$3p^5 4s^1$	s_5	98819.60	93143.7653	96481.16	95340.28	95232.25	94936.28	93750.6031
	s_4	99542.24	93750.6031	97147.05	95982.46	95869.18	95584.13	94553.6705
	s_3	100083.30	94553.6705	97762.05	96629.35	96522.04	96254.92	95399.8329
	s_2	102532.96	95399.8329	99245.07	97876.65	97687.73	97423.45	104102.1043
$3p^5 4p^1$	p_{10}	106397.64	104102.1043	105503.25	105273.27	105278.86	105149.05	105462.7649
	p_9	109733.87	105462.7649	107657.66	107241.85	107173.68	107034.05	105617.2753
	p_8	110020.26	105617.2753	107873.30	107443.28	107369.80	107230.21	106087.2651
	p_7	110562.37	106087.2651	108406.41	107970.90	107897.40	107765.28	106237.5571
	p_6	111246.32	106237.5571	108756.80	108266.85	108165.05	108029.46	107054.2773
	p_5	112095.20	107054.2773	109490.60	109011.54	108913.93	108794.19	107131.7139
	p_4	112252.81	107131.7139	109700.67	109210.30	109108.44	108990.90	107289.7054
	p_3	112537.00	107289.7054	109858.50	109329.08	109217.52	109090.03	107496.4219
	p_2	112682.33	107496.4219	110031.23	109524.87	109418.72	109301.34	108722.6247
	p_1	117690.31	108722.6247	113198.71	112249.86	111895.51	111776.57	93143.7653

After the single calculation was performed, the active space was increased and the following results were obtained.

Table 3.3.3 Calculated energy levels of the $3p^5 4s^1$ and $3p^5 4p^1$ configurations of Ar*, using a larger active space by opening 5s and 5p orbitals in the calculation.

Experimental Ground State Energy = 0.00 cm^{-1}								
	Energy Level	AVDZ	AVTZ	AVQZ	AV5Z	CBS	Rel Correction	Experimental (cm^{-1})[11,12]
$3p^5 4s^1$	s_5	98515.75	97402.74	96459.42	95357.46	95254.05	94956.74	93143.7653
	s_4	99238.43	98100.57	97128.87	96005.13	95896.63	95611.20	93750.6031
	s_3	99777.37	98677.19	97739.20	96645.45	96542.20	96274.97	94553.6705
	s_2	102246.78	100583.08	99257.22	97934.06	97753.73	97484.07	95399.8329
$3p^5 4p^1$	p_{10}	106186.21	105720.47	105619.09	105415.29	105423.75	105296.24	104102.1043
	p_9	109487.94	108215.08	107760.62	107380.95	107318.76	107177.35	105462.7649
	p_8	109772.35	108458.31	107981.54	107589.90	107523.23	107383.31	105617.2753
	p_7	110312.83	108991.17	108507.93	108109.95	108042.37	107906.484	106087.2651
	p_6	111005.42	109484.55	108879.08	108428.80	108334.04	108196.18	106237.5571
	p_5	111849.61	110196.11	109597.26	109156.57	109064.56	108936.45	107054.2773
	p_4	112005.23	110419.96	109810.72	109361.09	109266.09	109144.26	107131.7139
	p_3	112287.18	110624.64	109960.61	109472.30	109367.39	109237.44	107289.7054
	p_2	112435.39	110774.64	110137.63	109671.86	109571.87	109448.11	107496.4219
	p_1	117643.17	115078.48	113349.38	112419.30	112061.52	111934.09	108722.6247

Differences between experimental and CBS and relativist correction energy values were determined and are shown in Table 3.3.4. It was noted that the CBS extrapolation energy values differed from the experimental values by a constant 2008 cm^{-1} and the relativistic corrections by roughly 1792 cm^{-1}. Subtracting these differences from their respective calculations yielded values closer to experimental energies.

Table 3.3.4 Differences between various experimental, CBS extrapolation, and relativistic corrections energy level values.

Energy Level	Expt'l-CBS (cm^{-1})	CBS-Rel (cm^{-1})	Exp-Rel (cm^{-1})	CBS-2088 cm^{-1} (cm^{-1})	Exp-(CBS-2008 cm^{-1}) (cm^{-1})	Rel-1792 cm^{-1} (cm^{-1})	Exp-(Rel-1792 cm^{-1}) (cm^{-1})
s_5	-2088.4847	-295.97	-1792.5147	93144.25	-0.4847	93144.28	-0.5147
s_4	-2118.5769	-285.05	-1833.5269	93781.18	-30.5769	93792.13	-41.5269
s_3	-1968.3695	-267.12	-1701.2495	94434.04	119.6305	94462.92	90.7505
s_2	-2287.8971	-264.28	-2023.6171	95599.73	-199.8971	95631.45	-231.6171
p_{10}	-1176.7557	-129.81	-1046.9457	103190.86	911.2443	103357.05	745.0543
p_9	-1710.9151	-139.63	-1571.2851	105085.68	377.0849	105242.05	220.7149
p_8	-1752.5247	-139.59	-1612.9347	105281.8	335.4753	105438.21	179.0653
p_7	-1810.1349	-132.12	-1678.0149	105809.4	277.8651	105973.28	113.9851
p_6	-1927.4929	-135.59	-1791.9029	106077.05	160.5071	106237.46	0.0971
p_5	-1859.6527	-119.74	-1739.9127	106825.93	228.3473	107002.19	52.0873
p_4	-1976.7261	-117.54	-1859.1861	107020.44	111.2739	107198.9	-67.1861
p_3	-1927.8146	-127.49	-1800.3246	107129.52	160.1854	107298.03	-8.3246
p_2	-1922.2981	-117.38	-1804.9181	107330.72	165.7019	107509.34	-12.9181
p_1	-3172.8853	-118.94	-3053.9453	109807.51	-1084.8853	109984.57	-1261.9453

The pumping (s_5-p_9), collisional relaxation (p_9-p_{10}), and lasing (p_{10}-s_5) energies involved in Ar* laser systems were also determined and are reported in Table 3.3.5

Table 3.3.5 Calculated differences of interested energy levels in Ar* laser systems.

Energy Transition	Calculated Energy (cm^{-1})	Experimental Energy (cm^{1})[11,12]
s_5-p_9	12097.77	12318.9996
p_9-p_{10}	1885.00	1360.6606
p_{10}-s_5	10212.77	10958.339

II. Ar*+He Potential Energy Curves

Potential energy curves of Ar*+He were determined for the ground, *s*, and *p* states of Ar*, using mcscf theory and an all-valence double zeta basis set. A total of 17 potential energy curves were calculated, one for ground state, four arises from the Ar* *s* states, and twelve arising from the Ar* *p* states.

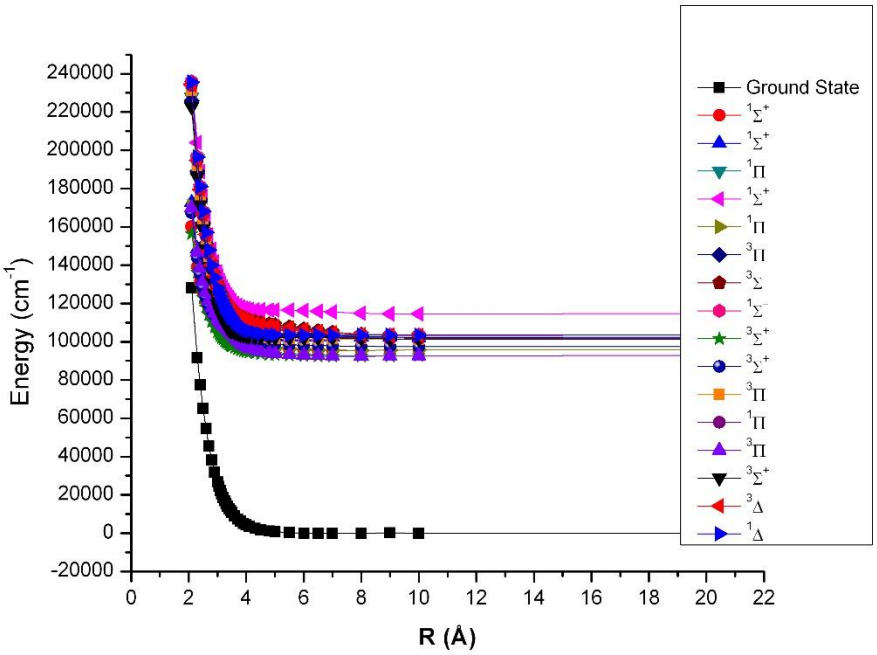

Figure 3.3.1 Potential energy curves of the molecular states of Ar*+ He arising from the ground state, s states, and p states of Ar*.

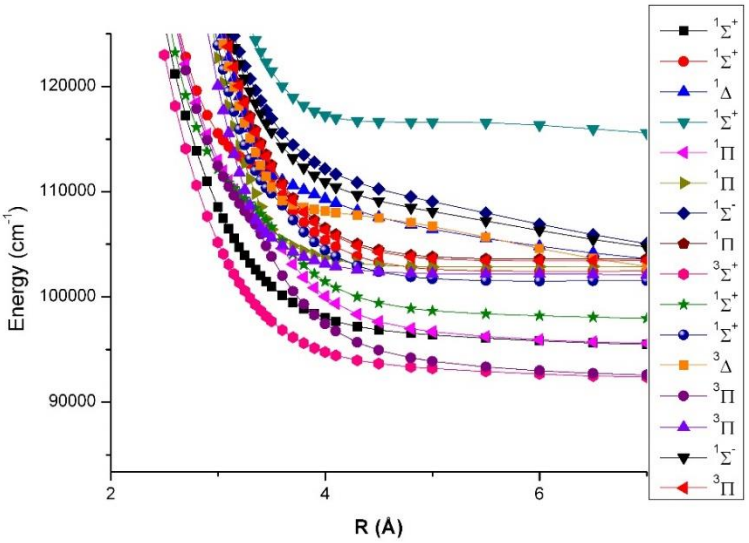

Figure 3.3.2 Zoomed region of potential energy curves of the molecular states of Ar* + He arising from the s states and p states of Ar*.

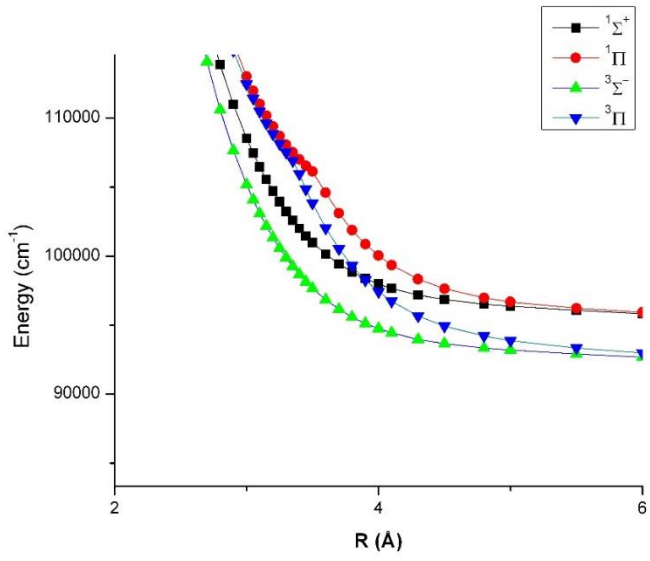

Figure 3.3.3 Zoomed region of potential energy curves of the molecular states of Ar* + He arising from the s states of Ar*.

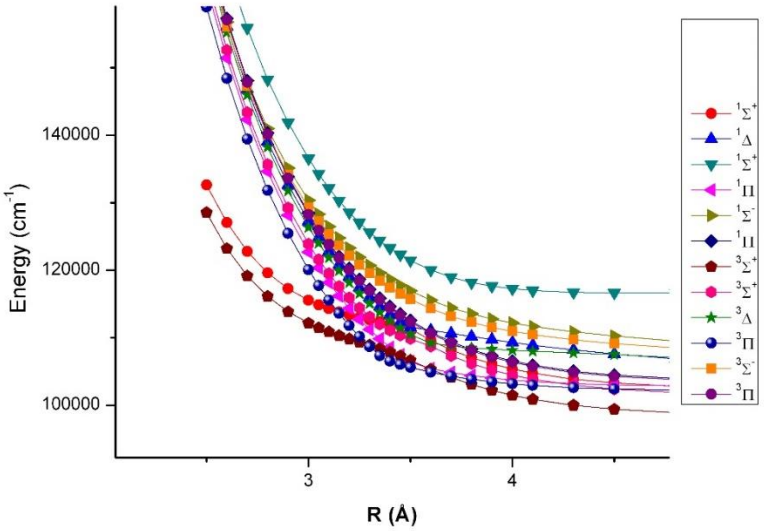

Figure 3.3.4 Zoomed region of potential energy curves of the molecular states of Ar* + He arising from the p states of Ar*.

3.4 References

1. Krupke, W. F.; Beach, R. J.; Kanz, V. K.; Payne, S. A. Resonance transition 795-nm rubidium laser. *Opt. Lett.* **2003**, *28*, 2336-2338.

2. Krupke, W. F. Diode pumped alkali lasers (DPALs)-A review (rev 1). *Progress in Quantum Electronics* **2012**, *36*, 4-28.

3. Han, J.; Glebov, L.; Venus, G.; Heaven, M. C. Demonstration of a diode-pumped metastable Ar laser. *Opt. Lett.* **2013**, *38*, 5458-5461.

4. Herzberg, G. *Atomic Spectra and Atomic Structure;* Dover: New York, 1994; pp 38-96,135.

5. University of Toronto Appendix 1: Coupling Schemes and Notation. **2011**.

6. Raju, G. G. *Gaseous Electronics: Theory and Practice;* Taylor & Francis Group: Boca Raton, 2006; pp 643-653.

7. Thakur, S. N.; Rai, D. K. *Atom, Laser, and Spectroscopy;* PHI Learning Private Limited: New Delhi, 2010; pp 346-348.

8. Csele, M. *Fundamentals of Light Sources and Lasers;* John Wiley & Sons: Hoboken, 2004; pp 49-79.

9. Saloman, E. B.; Sansonetti, C. J. Wavelengths, energy level classifications, and energy levels for the spectrum of neutral neon. *Journal of Physical and Chemical Reference Data* **2004**, *33*, 1113-1158.

10. Kaufman, V.; Minnhage.L Accurate Ground-Term Combinations in Ne-i. *J. Opt. Soc. Am.* **1972**, *62*, 92.

11. Velchev, I.; Hogervorst, W.; Ubachs, W. Precision VUV spectroscopy of Ar I at 105 nm. *J. Phys. B: At. Mol. Opt. Phys.* **1999**, *32*, L511-L516.

12. Minnhagen, L. Spectrum and the energy levels of neutral argon, Ar I. *J. Opt. Soc. Am.* **1973**, *63*, 1185-1198.

13. Hollas, J. M. *Basic Atomic and Molecular Spectroscopy;* John Wiley & Sons: New York, 2002; pp 60-62.

14. Silbey, R. J.; Alberty, R. A.; Bawendi, M. G. *Physical Chemistry;* John Wiley & Sons: Hoboken, 2005; pp 388.

15. Herzberg, G. *Molecular Spectra and Molecular Structure;* D. Van Nostrand Company Inc.: New York, 1965; pp 317-322.

Appendix C

File C.1 Calculation for Ar* ground state, $3p^5 4s^1$, and $3p^5 4p^1$ energy levels

```
***,Ar* atom
memory,200,m
gprint,orbitals,civector
!gprint,orbitals,civector,pspace
dkroll=1
!$my_basis=[avdz,avtz,avqz,av5z]
$my_basis=[avdz-dk,avtz-dk,avqz-dk,av5z-dk]

do i=1,#my_basis
basis=my_basis(i)

geometry={Ar};

text,3p54s1 and 3p54p1 state

{multi
occ,4,3,3,0,3,0,0,0;
wf,18,2,0
wf,18,3,0
wf,18,5,0
wf,18,1,0;state,4
wf,18,4,0;state,2     ! px py product
wf,18,6,0;state,2     ! px pz product
wf,18,7,0;state,2     ! py pz product
wf,18,2,2
wf,18,3,2
wf,18,5,2
wf,18,1,2;state,3
wf,18,4,2;state,2     ! px py product
wf,18,6,2;state,2     ! px pz product
wf,18,7,2;state,2     ! py pz product
}

{ci;wf,18,2,0;save,3020.2;noexc}
{ci;wf,18,3,0;save,3030.2;noexc}
{ci;wf,18,5,0;save,3050.2;noexc}
{ci;wf,18,1,0;state,4;save,3010.2;noexc}
{ci;wf,18,4,0;state,2;save,3040.2;noexc}
{ci;wf,18,6,0;state,2;save,3060.2;noexc}
```

```
{ci;wf,18,7,0;state,2;save,3070.2;noexc}

{ci;wf,18,2,2;save,3022.2;noexc}
{ci;wf,18,3,2;save,3032.2;noexc}
{ci;wf,18,5,2;save,3052.2;noexc}
{ci;wf,18,1,2;state,3;save,3012.2;noexc}
{ci;wf,18,4,2;state,2;save,3042.2;noexc}
{ci;wf,18,6,2;state,2;save,3062.2;noexc}
{ci;wf,18,7,2;state,2;save,3072.2;noexc}


{ci;wf,18,2,0;save,4020.2}; e4=energd
{ci;wf,18,3,0;save,4030.2}; e5=energd
{ci;wf,18,5,0;save,4050.2}; e6=energd
{ci;wf,18,1,0;state,4;save,4010.2}; p5=energd
{ci;wf,18,4,0;state,2;save,4040.2}; p6=energd
{ci;wf,18,6,0;state,2;save,4060.2}; p7=energd
{ci;wf,18,7,0;state,2;save,4070.2}; p8=energd

{ci;wf,18,2,2;save,4022.2}; e1=energd
{ci;wf,18,3,2;save,4032.2}; e2=energd
{ci;wf,18,5,2;save,4052.2}; e3=energd

{ci;wf,18,1,2;state,3;save,4012.2}; p1=energd
{ci;wf,18,4,2;state,2;save,4042.2}; p2=energd
{ci;wf,18,6,2;state,2;save,4062.2}; p3=energd
{ci;wf,18,7,2;state,2;save,4072.2}; p4=energd



lsint
!{ci;hlsmat,ls,3022.2,3032.2,3052.2,3012.2,3042.2,3062.2,3072.2,3020.2,
3030.2,3050.2,3010.2,3040.2,3060.2,3070.2;print,hls=2}
!{ci;hlsmat,ls,4022.2,4032.2,4052.2,4012.2,4042.2,4062.2,4072.2,4020.2,
4030.2,4050.2,4010.2,4040.2,4060.2,4070.2;print,hls=2}
hlsdiag=[e1,e2,e3,p1,p2,p3,p4,e4,e5,e6,p5,p6,p7,p8]
{ci;hlsmat,ls,4022.2,4032.2,4052.2,4012.2,4042.2,4062.2,4072.2,4020.2,4
030.2,4050.2,4010.2,4040.2,4060.2,4070.2;print,hls=2}

e_so=energy
s5(i)=(e_so(11)+e_so(14)+e_so(26)+e_so(47)+e_so(48))/5
s4(i)=(e_so(12)+e_so(15)+e_so(27))/3
s3(i)=e_so(49)
s2(i)=(e_so(13)+e_so(16)+e_so(28))/3
ep10(i)=(e_so(17)+e_so(29)+e_so(38))/3
ep9(i)=(e_so(2)+e_so(30)+e_so(18)+e_so(39)+e_so(19)+e_so(31)+e_so(40))/
7
ep8(i)=(e_so(3)+e_so(4)+e_so(20)+e_so(32)+e_so(41))/5
ep7(i)=(e_so(21)+e_so(33)+e_so(42))/3
ep6(i)=(e_so(5)+e_so(6)+e_so(22)+e_so(34)+e_so(43))/5
```

```
ep5(i)=(e_so(23)+e_so(35)+e_so(44))/3
ep4(i)=(e_so(7)+e_so(8)+e_so(24)+e_so(36)+e_so(45))/5
ep3(i)=e_so(9)
ep2(i)=(e_so(25)+e_so(37)+e_so(46))/3
ep1(i)=e_so(10)
ed_ar_gs(i)=e_so(1)
!e_ar_gs_avdz=-526.96134076
!e_ar_gs_avtz=-527.03217055
!e_ar_gs_avqz=-527.05590300
!
ed_ar_gs_avdz=-526.97022534
ed_ar_gs_avtz=-527.04671919
ed_ar_gs_avqz=-527.07243843
ed_ar_gs_av5z=-527.08040879

!e1_diff=(p1-ed_ar_gs_av5z)*tocm
!e2_diff=(p7(2)-ed_ar_gs_avtz)*tocm
!e3_diff=(p7(3)-ed_ar_gs_avqz)*tocm
!e4_diff=(p7(4)-ed_ar_gs_av5z)*tocm

enddo

extrapolate,basis=avdz-dk:avtz-dk:avqz-dk:av5z-
dk,etot=ed_ar_gs,method=ex2
ed_gs_cbs(1:5)=energy(1:5)

extrapolate,basis=avdz-dk:avtz-dk:avqz-dk:av5z-dk,etot=s5,method=ex2
e_s5(1:5)=energy(1:5)
es5_diff=(e_s5-ed_gs_cbs)*tocm

extrapolate,basis=avdz-dk:avtz-dk:avqz-dk:av5z-dk,etot=s4,method=ex2
e_s4(1:5)=energy(1:5)
es4_diff=(e_s4-ed_gs_cbs)*tocm

extrapolate,basis=avdz-dk:avtz-dk:avqz-dk:av5z-dk,etot=s3,method=ex2
e_s3(1:5)=energy(1:5)
es3_diff=(e_s3-ed_gs_cbs)*tocm

extrapolate,basis=avdz-dk:avtz-dk:avqz-dk:av5z-dk,etot=s2,method=ex2
e_s2(1:5)=energy(1:5)
es2_diff=(e_s2-ed_gs_cbs)*tocm

extrapolate,basis=avdz-dk:avtz-dk:avqz-dk:av5z-dk,etot=ep10,method=ex2
e_p10(1:5)=energy(1:5)
ep10_diff=(e_p10-ed_gs_cbs)*tocm

extrapolate,basis=avdz-dk:avtz-dk:avqz-dk:av5z-dk,etot=ep9,method=ex2
e_p9(1:5)=energy(1:5)
ep9_diff=(e_p9-ed_gs_cbs)*tocm
```

```
extrapolate,basis=avdz-dk:avtz-dk:avqz-dk:av5z-dk,etot=ep8,method=ex2
e_p8(1:5)=energy(1:5)
ep8_diff=(e_p8-ed_gs_cbs)*tocm

extrapolate,basis=avdz-dk:avtz-dk:avqz-dk:av5z-dk,etot=ep7,method=ex2
e_p7(1:5)=energy(1:5)
ep7_diff=(e_p7-ed_gs_cbs)*tocm

extrapolate,basis=avdz-dk:avtz-dk:avqz-dk:av5z-dk,etot=ep6,method=ex2
e_p6(1:5)=energy(1:5)
ep6_diff=(e_p6-ed_gs_cbs)*tocm

extrapolate,basis=avdz-dk:avtz-dk:avqz-dk:av5z-dk,etot=ep5,method=ex2
e_p5(1:5)=energy(1:5)
ep5_diff=(e_p5-ed_gs_cbs)*tocm

extrapolate,basis=avdz-dk:avtz-dk:avqz-dk:av5z-dk,etot=ep4,method=ex2
e_p4(1:5)=energy(1:5)
ep4_diff=(e_p4-ed_gs_cbs)*tocm

extrapolate,basis=avdz-dk:avtz-dk:avqz-dk:av5z-dk,etot=ep3,method=ex2
e_p3(1:5)=energy(1:5)
ep3_diff=(e_p3-ed_gs_cbs)*tocm

extrapolate,basis=avdz-dk:avtz-dk:avqz-dk:av5z-dk,etot=ep2,method=ex2
e_p2(1:5)=energy(1:5)
ep2_diff=(e_p2-ed_gs_cbs)*tocm

extrapolate,basis=avdz-dk:avtz-dk:avqz-dk:av5z-dk,etot=ep1,method=ex2
e_p1(1:5)=energy(1:5)
ep1_diff=(e_p1-ed_gs_cbs)*tocm
```

File C.2 Calcation for Ar*+He molecular potential energy curves.

```
***,Ar* atom
memory,200,m
gprint,orbitals,civector

r=[20.0,10.0,9.0,8.0,7.0,6.5,6.0,5.5,5.0,4.8,4.5,4.3,4.1,4.0,3.9,3.8,3.
7,3.6,3.5,3.45,3.4,3.35,3.3,3.25,3.2,3.15,3.1,3.05,3.0,2.9,2.8,2.5,2.2,
2.0]

do i=1,#r

basis=avdz

geometry={Ar
He Ar Rx
};
Rx=r(i)
```

```
text,3p54s1 and 3p54p1 state

{multi
occ,10,4,4,0;
wf,20,1,0;state,5
wf,20,2,0;state,3     ! px pz product
wf,20,3,0;state,3     ! py pz product
wf,20,4,0;state,2     ! px py product
}
wf,20,1,2;state,4
wf,20,2,2;state,3     ! px pz product
wf,20,3,2;state,3     ! py pz product
wf,20,4,2;state,2     ! px py product
}
e1(i)=energy(1)*tocm
e2(i)=energy(2)*tocm
e3(i)=energy(3)*tocm
e4(i)=energy(4)*tocm
e5(i)=energy(5)*tocm
e6(i)=energy(6)*tocm
e7(i)=energy(7)*tocm
e8(i)=energy(8)*tocm
e9(i)=energy(9)*tocm
e10(i)=energy(10)*tocm
e11(i)=energy(11)*tocm
e12(i)=energy(12)*tocm
e13(i)=energy(13)*tocm
e14(i)=energy(14)*tocm
e15(i)=energy(15)*tocm
e16(i)=energy(16)*tocm
e17(i)=energy(17)*tocm
e18(i)=energy(18)*tocm
e19(i)=energy(19)*tocm
e20(i)=energy(20)*tocm
e21(i)=energy(21)*tocm
e22(i)=energy(22)*tocm
e23(i)=energy(23)*tocm
e24(i)=energy(24)*tocm
e25(i)=energy(25)*tocm

enddo
table, r, e1, e2, e3, e4, e5, e6, e7, e8, e9, e10, e11, e12, e13, e14,
e15, e16, e17, e18, e19, e20, e21, e22, e23, e24, e25
save,arhe.dat
```

Chapter 4: Relaxation Kinetics of Nitrosyl Bromide (BrNO)

4.1 Introduction

I. Motivation

The chemical kinetics of the formation of bromide nitrosyl (BrNO) have been of interest to the laser community within the past decade. In efforts to produce a tunable laser in the infrared for counter-defense applications, the 5.4 μm transition of nitric oxide (NO) has been investigated as a potential lasing transition. In this system, molecular bromine (Br_2) is photolyzed to produce electronically excited atomic bromine (Br*). Br* then undergoes a collisional energy transfer to vibrationally excited NO (v=2), which then lases down to NO (v=1). Complication arise due to the reactivity of Br_2 with NO, producing BrNO. This reaction inhibits the Br*→NO (v=2) energy transfer, in turn inhibiting NO lasing. This work attempts to understand the formation kinetics of BrNO, in order to improve the NO laser system.

Previous works have sought to understand the formation of nitrosyl bromide. Hisatsune *et al.*[1] studied the formation of nitrosyl bromide with the concentration of nitric oxide in excess, in order to minimize the reverse reaction. Pressures were monitored through infrared spectroscopy of the NO and BrNO absorption bands around 1600 cm^{-1} and 530 cm^{-1}, respectively. Houel *et al.*[2] as well monitored the formation reaction with excess bromine but also looked at the ultraviolet absorption band of BrNO at chemical equilibrium. Thermodynamics properties, such as activation energy, entropy of the reaction, and enthalpy of the reaction, were also determined by Houel. Hippler[3] photolyzed Br_2 in the presence of varying pressures of He, in an investigation of the

recombination of Br atoms after photolysis. Nitric oxide was also added in excess to Br after photolysis and the formation of BrNO was monitored in the presence of He. Motivated by interest in the Br* pumped NO(v=2→1) laser, kinetics of the BrNO formation reaction were the subject of two more recent studies at the Air Force Institute of Technology (AFIT) at nearby Wright-Patterson Air Force Base (WPAFB).

Godfrey[4] investigated the gas phase BrNO equilibrium reactions, starting with reactants Br_2 and NO and integrated the full rate equation, casting all partial pressures in terms of starting values. This approach yields a differential equation in a fraction completion variable *x*,

$$\frac{dx}{dt} = a + bx + cx^2 + dx^3 \tag{1}$$

The solution, obtained with Mathematic is rather complicated; however, a curious choice was made to avoid casting the integrated rate solution in the form $f(x)=k_f t$, and choosing an unusual representation in which time becomes the dependent variable in Godfrey's expression,

$$t(x) - t_0 = \frac{1}{k_f} f(x, [BrNO]_0, [Br_2]_0, [NO]_0 K_{eq}) \tag{2}$$

Since the experimental data were fitted in a nonlinear regression perhaps it is of little matter which form the integrated solution is used. Godfrey[4] also spectroscopically determined vibrational and rotational constants for the infrared fundamental and various overtone combinations of various isotopologues of BrNO. This part of Godfrey's Ph.D. dissertation also represents a significant contribution to BrNO spectroscopy.

Mahoney[5] used time-resolved infrared spectroscopy to monitor the formation of BrNO from Br_2 and NO following laser photolysis to drive the equilibrium mixture fully back to reactants. Using the same analysis method as Godfrey, excesses of NO and Br_2 were also independently employed to monitor the pseudo-first and pseudo-second order reactions.

This work focuses on determining the forward and reverse rate coefficients of the formation reaction of BrNO through relaxation kinetics, in which the chemical system at equilibrium will be perturbed and the rate of return to equilibrium will be monitored. Espenson[6] claims that the relaxation kinetics method can be used not only for perturbations from equilibrium but also for any chemical reaction that starts completely on one side of the reaction. This research will test Espenson's claim applied to the BrNO formation reaction and will employ both laser photolysis and volume expansions as chemical perturbations. The rate of the return to equilibrium will be monitored and used to determine the forward and reverse rate coefficients. In the case of a photolytic perturbation the equilibrium position will be the same as before the perturbation, so long as the temperature is not changed. In the volume expansion perturbation, the equilibrium position will be a new one. Equilibrium constants will be determined from partial pressures, which are derived from initial compositions, total equilibrium pressure and the reaction stoichiometry.

II. Thermodynamics and Equilibrium Constant

The equilibrium constant of the formation of nitrosyl bromide can be calculated from thermodynamic properties, such as the standard enthalpy of formation and the standard molar entropy at a specific temperature. The standard enthalpy and entropy of

the formation of nitrosyl bromide can be determined by using the standard enthalpy of formation and the standard molar entropy of the reactants and product.

$$\Delta_r H^0 = 2\Delta_f H^0(BrNO(g)) - 2\Delta_f H^0(NO(g)) - \Delta_f H^0(Br_2(g)) \quad (3)$$

$$\Delta S^0 = 2\Delta S^0(BrNO(g)) - 2\Delta S^0(NO(g)) - \Delta S^0(Br_2(g)) \quad (4)$$

The standard Gibb's energy of the formation of nitrosyl bromide can then be calculated as

$$\Delta_f G^0 = \Delta_r H^0 - \Delta_r S^0 T \quad (5)$$

where T is the temperature in units of Kelvin. The equilibrium constant K_{eq} can be determined from the following relationship

$$K_{eq} = e^{-\frac{\Delta_r G^0}{RT}} \quad (6)$$

where R is the universal gas constants with units of *J/mol*K*.

The following literature values [7] of the standard enthalpy of formation and standard molar entropy of Br_2, NO, and BrNO were used in determining the standard enthalpy and entropy of the formation of nitrosyl bromide.

Table 4.1.1 Literature values used to determine the standard entropy and molar entropy of the formation of nitrosyl bromide.

Chemical Species	$\Delta_f H^0$ (kJ/mol)	ΔS^0(J/mol*K)
Br_2 (g)	30.91	245.38
NO (g)	90.29	210.76
BrNO (g)	82.13	273.53

Using a room temperature of 298.15K, the enthalpy, entropy and Gibb's energy of the formation of nitrosyl bromide, along with the equilibrium constant, were calculated using Equations (3-6) and are reported in Table 4.1.2.

Table 4.1.2 Determined thermodynamic properties of the formation of nitrosyl bromide at 298.15K.

$\Delta_r H^0$ (kJ/mol)	$\Delta_r S^0$ (J/mol)	$\Delta_f G^0$ (kJ/mol)	K_{eq} (unitless)	K_{eq} ($torr^{-1}$)
-47.23	-119.8	-11.5	103.43	0.138

A plot of K_{eq} vs. $T\ (K)$ showed that at 294K, the average temperature of the experimentation in this research, the $\partial K/\partial T$ tangential slope has a value of -.0115 K^{-1}. This indicates that at 294K, a 0.01 change in K_{eq} corresponds to a temperature change of 1K.

III. Determination of Rate Coefficients

Relaxation Methods

Typically, chemical formation reactions are monitored through their forward reactions, as simplified integrated rate equations can be used to determine forward rate coefficients. When reverse reactions are important, the integrated rate equation takes a more complex form and can be difficult to form into a linear relationship to determine the desired rate coefficients graphically. One method of studying equilibrium reactions is the *relaxation method* [6]. This method begins with a system at equilibrium and imposes a perturbation, such as a rapid change in temperature or change in concentration, and monitors the return back to equilibrium. Common perturbations include photolysis and

solvent dilution. Names such as “concentration jump”, “temperature jump”, and “pH jump” often are associated with the relaxation kinetics methods.

Espenson[6] proposes that the relaxation analysis methodology is *not* restricted to equilibrium kinetics but may be used also for all chemical reactions that start on one side of the reaction. In his book, Espenson[6] develops the analysis equations for application of the relaxation kinetics method for the reaction,

$$A \rightleftarrows 2P \tag{7}$$

in which a chemical perturbation is imposed, causing an instantaneous shift δ_0 from equilibrium, the concentrations at any time can be written in terms of their concentrations at equilibrium and the shift from equilibrium, taking into account reaction stoichiometry.

$$[A]_t = [A]_e + \delta \tag{8}$$

$$[P]_t = [P]_e - 2\delta \tag{9}$$

The extent of the shift from the new equilibrium caused by perturbation δ is defined to be always positive. Therefore, time-dependent concentrations of chemical species that decrease in pressure as the system returns to equilibrium will be defined as the sum of their equilibrium pressures and δ while concentrations of species being formed are defined as the difference between the equilibrium pressure and δ.

For the formation of nitrosyl bromide,

$$Br_2 + 2NO \underset{k_r}{\overset{k_f}{\rightleftarrows}} 2BrNO \tag{10}$$

the concentrations of Br_2, NO, and BrNO at any time can be defined as

$$P_{Br_2,t} = P_{Br_2,e} + \delta_f \tag{11}$$

$$P_{NO,t} = P_{NO,e} + 2\delta_f \tag{12}$$

$$P_{BrNO,t} = P_{BrNO,e} - 2\delta_f \tag{13}$$

where δ_f is the δ observed for formation data. Equations (11-13) are also true for pressures after laser photolysis. The reaction rate can be defined as

$$Rate = -\frac{dP_{Br_2}}{dt} = -\frac{d\delta_f}{dt} = k_f P_{Br_2}(P_{NO})^2 - k_r(P_{BrNO})^2 \tag{14}$$

Equations (11-13) can be substituted into Eqn. (10) to write the reaction rate in terms of the equilibrium pressures.

$$-\frac{d\delta_f}{dt} = k_f\left(P_{Br2,e} + \delta_f\right)\left(P_{NO,e} + 2\delta_f\right)^2 - k_r(P_{BrNO,e} - 2\delta_f)^2 \tag{15}$$

Multiplying out the terms results in

$$\frac{d\delta_f}{dt} = -\left(4k_f P_{Br2,e}P_{NO,e} + k_f {P_{NO,e}}^2 + 4k_f K^{-1}P_{BrNO,e}\right)\delta_f$$

$$-4k_f\left[\left(P_{Br2,e} + P_{NO,e}\right) - K^{-1}\right]{\delta_f}^2 - 4k_f {\delta_f}^3 \tag{16}$$

resulting in a third-order polynomial in δ_f. Equation (16) can be rearranged in the form where

$$\frac{d\delta_f}{dt} = k_f(a\delta_f + b{\delta_f}^2 + c{\delta_f}^3) \tag{17}$$

where

$$a = -\left(4P_{Br2,e}P_{NO,e} + {P_{NO,e}}^2 + 4K^{-1}P_{BrNO,e}\right) \tag{18}$$

$$b = -4\left[\left(P_{Br2,e} + P_{NO,e}\right) - K^{-1}\right] \tag{19}$$

$$c = -4 \tag{20}$$

Wolfram Mathematica® was used to integrate Eqn. (17) and achieve the following solution

$$g(\delta_f) = \frac{\frac{-2btan^{-1}\left(\frac{b+2c\delta_f}{\sqrt{4ac-b^2}}\right)}{\sqrt{4ac-b^2}} + \frac{2btan^{-1}\left(\frac{b+2c\delta_{f,0}}{\sqrt{4ac-b^2}}\right)}{\sqrt{4ac-b^2}} + ln\left(\frac{a+\delta_{f,0}\left(b+c\delta_{f,0}\right)}{a+\delta_f\left(b+c\delta_f\right)}\right) + 2\,ln\left(\frac{\delta_f}{\delta_{f,0}}\right)}{2a} = k_f t \tag{21}$$

Equation (21) can be plotted as $g(\delta_f)$ vs. time to afford a slope equal to k_f. The reverse rate coefficient k_r can be determined from k_f and the measured K_{eq}. This method can be applied to data taken from formation trials and laser photolysis of BrNO. Laser photolysis of BrNO pushes the reaction (fully in some cases) back to the reactants and the return of the reaction back to equilibrium can be monitored to determine the rate coefficients, using the perturbation analysis previously described.

For an expansion into an evacuated volume, time-dependent pressures can be defined as

$$P_{Br_2,t} = P_{Br_2,e} - \delta_e \tag{22}$$

$$P_{NO,t} = P_{NO,e} - 2\delta_e \tag{23}$$

$$P_{BrNO,t} = P_{BrNO,e} + 2\delta_e \tag{24}$$

where δ_e is the δ observed in an expansion. Le Châtelier's principle states that, upon a perturbation, a chemical equilibrium will move to counteract the applied change[8]. When a gas phase chemical system expands into a larger evacuated volume, causing a decrease in pressure, Le Châtelier's principle predicts that the chemical equilibrium will move to the side with the greater amount of moles (the greatest pressure). In the case of the formation

of BrNO, upon a volume expansion, the equilibrium will move towards the left, resulting in the following rate.

$$Rate = \frac{dP_{Br_2}}{dt} = -\frac{d\delta_e}{dt} = -k_f P_{Br_2}(P_{NO})^2 + k_r(P_{BrNO})^2 \tag{25}$$

Equations (22-24) can be substituted into Eqn. (25) writing the reaction rate in terms of the equilibrium pressures.

$$\frac{d\delta_e}{dt} = k_f\left(P_{Br2,e} - \delta_e\right)\left(P_{NO,e} - 2\delta_e\right)^2 - k_r(P_{BrNO,e} + 2\delta_e)^2 \tag{26}$$

Multiplying out the terms results in

$$\frac{d\delta_e}{dt} = -\left(4k_f P_{Br2,e}P_{NO,e} + k_f {P_{NO,e}}^2 + 4k_f K^{-1}P_{BrNO,e}\right)\delta_e$$

$$+4k_f\left[\left(P_{Br2,e} + P_{NO,e}\right) - K^{-1}\right]{\delta_e}^2 - 4k_f {\delta_e}^3 \tag{27}$$

resulting in a third-order polynomial in δ_e.

$$\frac{d\delta_e}{dt} = k_f(a\delta_e + b{\delta_e}^2 + c{\delta_e}^3) \tag{28}$$

$$a = -\left(4P_{Br2,e}P_{NO,e} + {P_{NO,e}}^2 + 4K^{-1}P_{BrNO,e}\right) \tag{29}$$

$$b = 4\left[\left(P_{Br2,e} + P_{NO,e}\right) - K^{-1}\right] \tag{30}$$

$$c = -4 \tag{31}$$

The integration of $\frac{d\delta_e}{dt}$ results in the same solution as the integration of $\frac{d\delta_f}{dt}$, the only difference being the sign in the quadratic *b* term.

$$g(\delta_e) = \frac{\frac{-2btan^{-1}\left(\frac{b+2c\delta_e}{\sqrt{4ac-b^2}}\right)}{\sqrt{4ac-b^2}} + \frac{2btan^{-1}\left(\frac{b+2c\delta_{e,0}}{\sqrt{4ac-b^2}}\right)}{\sqrt{4ac-b^2}} + ln\left(\frac{a+\delta_{e,0}(b+c\delta_{e,0})}{a+\delta_e(b+c\delta_e)}\right) + 2\,ln\left(\frac{\delta_e}{\delta_{e,0}}\right)}{2a} = k_f t \tag{32}$$

Equation (32) can be plotted as $g(\delta_e)$ vs. time to afford a slope equal to k_f and the reverse rate coefficient k_r can be determined from k_f from and measured K_{eq}. This method is specific to expansion data.

Third-Order Integrated Rate Law for k_f Determination

Beginning with Br_2 and NO reactants, at early times in the development of the equilibrium, the rate expression is dominated by the forward reaction such that

$$\lim_{t\to 0}\left(-\frac{dP_{Br_2}}{dt}\right) = k_f P_{Br_2} {P_{NO}}^2 \tag{33}$$

This third-order rate equation has an integrated solution, reported in Benson's kinetics text[9], to which the early time-dependent reactant partial pressures may be fitted to obtained an experimental measurement of k_f. Benson[9] defines a parameter Δ as the stoichiometric difference between initial concentrations of reactants.

$$\Delta = 2P_{Br_2,0} - P_{NO,0} \tag{34}$$

As only forward reaction the considered, the change in the concentration of NO can be written in terms of the forward rate.

$$-\frac{dP_{NO}}{dt} = 2k_f {P_{NO}}^2 P_{Br_2} \tag{35}$$

The concentration of Br_2 at any time can be defined as the difference between the initial pressure of bromine and the stoichiometric change in NO.

$$P_{Br_2} = P_{Br_2.0} - \frac{1}{2}(P_{NO.0} - P_{NO}) \tag{36}$$

Factoring out a factor of ½ yields

$$P_{Br_2} = \frac{1}{2}\left(P_{NO} + 2P_{Br_2,0} - P_{NO,0}\right) \quad (37)$$

which can be further defined as

$$P_{Br_2} = \frac{1}{2}\left(P_{NO} + \Delta\right) \quad (38)$$

Equation (38) can then be substituted into Eqn. (31)

$$\frac{dP_{NO}}{dt} = -k_f {P_{NO}}^2 (P_{NO} + \Delta) \quad (39)$$

which can be rearranged into

$$dP_{NO}\left(\frac{\Delta}{{P_{NO}}^2} + \frac{1}{P_{NO}+\Delta} - \frac{1}{P_{NO}}\right) = -\Delta^2 k_f dt \quad (40)$$

After integration between the limits of $P_{NO,0}$ at t = 0 and P_{NO} at t, Eqn. (40) yields

$$\Delta\left(\frac{1}{P_{NO}} - \frac{1}{P_{NO,0}}\right) + \ln\left(\frac{P_{NO}}{P_{NO,0}}\frac{P_{NO,0}+\Delta}{P_{NO}+\Delta}\right) = \Delta^2 k_f t \quad (41)$$

Substitution of Eqn. (34) in Eqn. (41) affords

$$\Delta\left(\frac{1}{P_{NO}} - \frac{1}{P_{NO,0}}\right) + \ln\left(\frac{P_{NO}}{P_{NO,0}}\frac{P_{Br_2,0}}{P_{Br_2}}\right) = \Delta^2 k_f t \quad (42)$$

In order for $k_f t$ to be isolated, Δ can be replaced by its definition in Eqn. (34) and each side divided by Δ^2.

$$\frac{-1}{(P_{NO,0}-2P_{Br_2,0})}\left(\frac{1}{P_{NO}} - \frac{1}{P_{NO,0}}\right) + \frac{1}{(P_{NO,0}-2P_{Br_2,0})^2} ln\left(\frac{P_{NO}P_{Br_2,0}}{P_{NO,0}P_{Br_2}}\right) = k_f t \quad (43)$$

A plot of the LHS of Eqn. (43) vs. time will result in a slope equal to k_f. Again, the reverse rate coefficient k_r can be determined from K_{eq}. As this analysis only takes into account the forward reaction, it can only be applied to formation data at early times, as

the reverse rate grows at later times. As implemented in the formation kinetics of this thesis, plots of LHS Eqn. (43) vs. time were fitted to a quadratic equation at early time and the linear coefficients were taken as k_f values.

Approximation of k_f from Expansion Data

This research will employ volume expansion, as well as laser photolysis, as perturbations upon the BrNO formation equilibrium. Therefore, the reverse rate may dominate the reaction rate at early times after the expansion.

This research found that at early times the forward rate was approximately 20% of the reverse rate for the 1:5 volume ratio expansions and 50% of the reverse rate for the 1:2 volume ratio expansions. For the 1:5 expansions, Eqn. (14) can be approximated as

$$Rate = -\frac{1}{2}\frac{dP_{BrNO}}{dt} = -k_f P_{Br_2} {P_{NO}}^2 + k_r {P_{BrNO}}^2 \approx 0.8 k_r {P_{BrNO}}^2 \quad (44)$$

In terms of the decreasing pressure of BrNO with respect to time,

$$-\frac{dP_{BrNO}}{dt} \approx 1.6 k_r {P_{BrNO}}^2 \quad (45)$$

As Eqn. (45) shows a second order rate, the integrated rate law for Eqn. (45) is

$$\frac{1}{P_{BrNO,t}} \approx \frac{1}{P_{BrNO,0}} + 1.6 k_r t \quad (46)$$

A plot of $1/P_{BrNO,t}$ vs. t at early times following an expansion perturbation will yield a slope of approximately $1.6k_r$ for 1:5 volume expansions and the slope will be approximately equal to k_r for 1:2 volume expansions. The forward rate coefficient can be determined then from the equilibrium constant K_{eq} and the reverse rate coefficient k_f. The

method, however, only gives an *approximation* of the rate coefficients and is therefore only to be used as an initial approximate of the desired rate coefficients.

Data Fitting Using Kintecus®

Kintecus® is a computational program operating on a Microsoft Excel® interface that can be used to determine kinetic parameters in chemical reactions. Written by James Ianni[10], Kintecus® has the five individual fitting algorithms (Mead & Nelder, Powerll, Simulated Annealing, Levenberg-Marquardt, and Complex) along with three comparison operators (relative least squares, standard least squares, and an author-devised proprietary function) that can be used to fit kinetic data. For an individual chemical reaction, time and concentration of chemical species are input requirements, as well as initial values of parameters to be fit. After the required iterations of the data, Kintecus® will provide an output file with the desired parameters and their standard deviations, as well as predicted concentration values at time intervals. These predicted values can be used to determined absolute average and maximum residuals of the fit. Kintecus® will be employed as another method to determine rate coefficients and equilibrium constants from the BrNO formation and perturbation data.

IV. Purpose

This research will employ relaxation kinetics to determine the rate coefficients and the equilibrium constant for the formation of nitrosyl bromide. The formation reaction of nitrosyl bromide will be monitored, using various initial pressures of Br_2 and NO. These formation trials will be analyzed using the integrated $g(\delta_f)$ solution, as well as the integrated third-order rate equation, in order to directly determine the forward rate

coefficient k_f, which in turn will allow k_r determination from the measured K_{eq}. Once the system is at equilibrium, perturbations of either laser photolysis or volume expansion (1:2 or 1:5 volume ratios) will be employed. The integrated $g(\delta_f)$ solution will be applied to the laser photolysis perturbation while the integrated $g(\delta_e)$ solution and the second-order k_r approximation will be applied to the volume expansion perturbations. Fitting methods using Kintecus® will also be applied to all formation and expansion trials to determine k_f, k_r, and K_{eq}.

4.2 Experimental

1. Theoretical Simulation

To predict the feasibility of relaxation kinetics analysis and the time extent of the formation and expansion reactions, a theoretical simulation was constructed before experiments were planned. Using an equilibrium constant K_{eq} literature value[4] of 0.214 $torr^{-1}$, equilibrium pressures of bromine, nitric oxide, and nitrosyl bromide were determined using initial bromine, nitric oxide, and nitrosyl bromide pressures of 20 torr, 40 torr, and 0 torr, respectively. The change x in the equilibrium pressure P_{eq} from the initial total pressure $P_{T,0}$ was then determined from the expression for the equilibrium constant, using a third order polynomial solution. Literature values[4] of the forward and reverse rate coeffients (k_f = 1.47 x 10^{-5} and k_r = 6.65 x 10^{-5}) were used to calculate the reaction rate at one second time intervals from 0 to 5400 seconds. After multiply the rate by the change in time (Δt = 1s) to obtained the change in pressure (Δx), the pressure of the chemical species at each time value were determined by subtracting the change in pressure from the initial pressure, taking into account the stoichiometric ratios. Finally, the pressures of the reactants and product as well as the total pressure were plotted as a function of time. Figure 4.2.1 shows the simulated total pressure as a function of time for initial bromine and nitric oxide pressures of 20 and 40 torr, respectively.

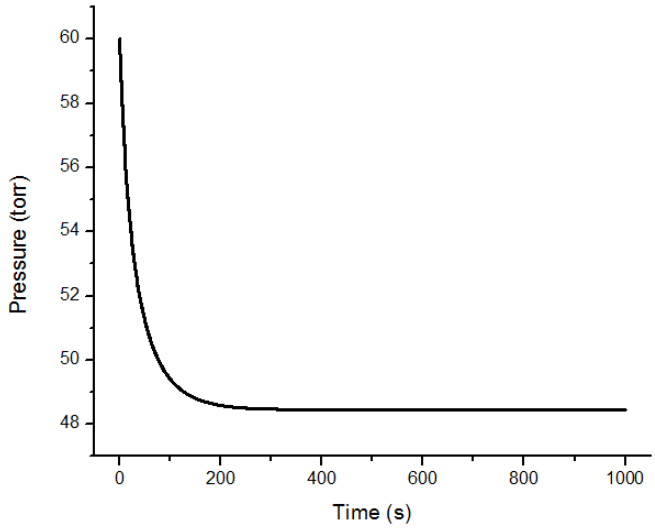

Figure 4.2.1. Simulated total pressure as a function of time from initial bromine and nitric oxide pressures of 20 and 40 torr, respectively.

To create a simulation of the expansion data, the equilibrium pressures were multiplied by the ratio of the two volumes in which the expansion was to take place to obtain the pressures at t = 0. Again, using literature values for the forward and reverse rate coefficients, rates at individual time values were calculated from which the total pressure and the pressures of the chemical species were calculated. Figure 4.2.2 shows a simulated 1:5 volume ratio expansion from the equilibrium position in Figure 4.2.11 with $P_{Br_2} : P_{NO} : P_{BrNO}$ = 8.450 torr :16.901 torr :23.099 torr. In time span of 200s. the pressure rise reached approximately 75% of its final value.

Ultimately, these simulations served to illustrate that the formation of nitrosyl bromide and its subsequent expansion could be monitored by the time-dependent total pressure of the system. It was therefore decided that experimental trials would be

monitored by the total pressure of the system and all data analysis would be done with theses recorded total pressures and initial reactant partial pressures.

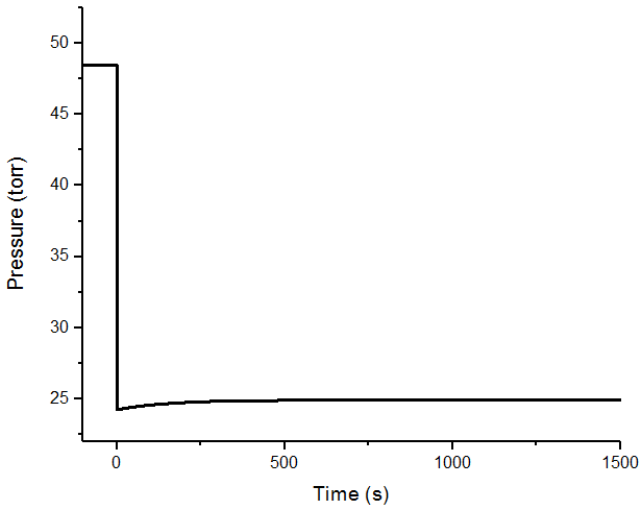

Figure 4.2.2 Expansion simulation using a 1:5 volume ratio and previous equilibrium conditions in **Figure 4.2.1**.

II. Experimental Designs

` Three spherical reaction vessels and a spectroscopic cell were glass blown by Timothy Henthorn at Ohio State University. Two of the reaction vessels had approximate volumes of 0.5 L and the other had an approximate volume of 2 L. The absorption cell was approximately 4.5 in length and allowed for spectroscopic windows to be attached at both ends of the cell.

For early laser photolysis work, one 0.5 L vessel was connected to one end of a 74 cm stainless steel laser tube (0.38 L) and to both the Br_2 and NO reservoirs. The reaction vessel was with Br_2 from a Br_2 reservoir, which was then transferred to the laser tube. After the reaction vessel was evacuated, it was filled with NO from the NO reservoir and

was then transferred to the laser tube for mixing. The second harmonic (532 nm) of a Nd:YAG was passed through the tube, pushing the equilibrium to the left. The return to chemical equilibrium was then monitored. Figure 4.2.3 shows a schematic for the experimental setup for the experiments involving the laser tube.

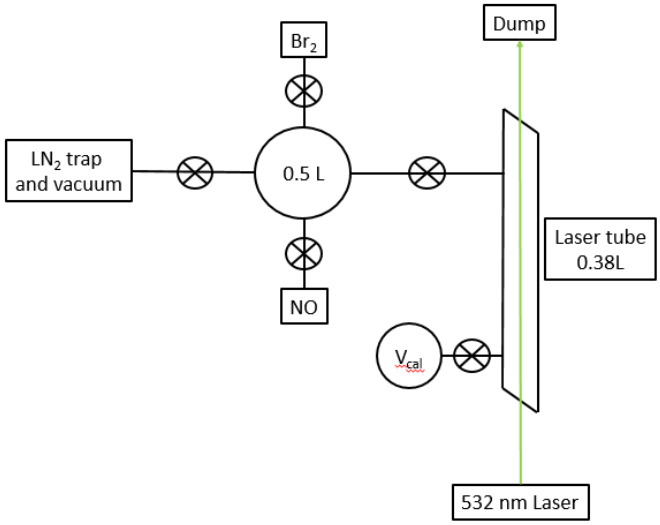

Figure 4.2.3 Experimental design for early laser photolysis experiments.

For other formation and expansion reactions, the three reaction vessels were connected in series. Each 0.5 L vessel was connected to either the Br_2 or NO reservoir. The first vessel would be filled with desired pressure of NO that when quickly released into the second vessel with Br_2 would ensure a desired pressure ratio of Br_2:NO. This allowed for the formation reaction to occur in the second 0.5 L vessel. Upon reaching equilibrium, the chemical system could then be expanded either back into the evacuated first 0.5 L reaction vessel for a 1:2 volume ratio expansion or into the 2 L reaction vessel for a 1:5 volume ratio expansion. An absorption cell was attached to the 2 L reaction vessel to allow for time-resolved spectroscopic data to be taken for the 1:5 volume ratio

expansions. Figure 4.2.4 shows the experimental design for these experiments. Each of the 0.5L vessels were fitted with 100 torr (full scale value) pressure gauge and the 2L vessel was fitted with a 10 torr gauge. All three pressure gauges were capacitance manometers with 10 volt output at the full scale pressure value. The 10 torr gauge and one of the 100 torr gauges (on the reaction vessel) were purchased for his project. The older 100 torr gauge (on the NO vessel) was calibrated against the newer 100 torr gauge. All three gauges were designed for ±0.15% accuracy of the measured pressure. All connections to the spherical reactors were via ½" stainless steel Cajon® fittings. All spherical reaction vessels were covered in black felt and the room lights were kept off during all experimentation to prevent unwanted photolysis of bromine by room lights.

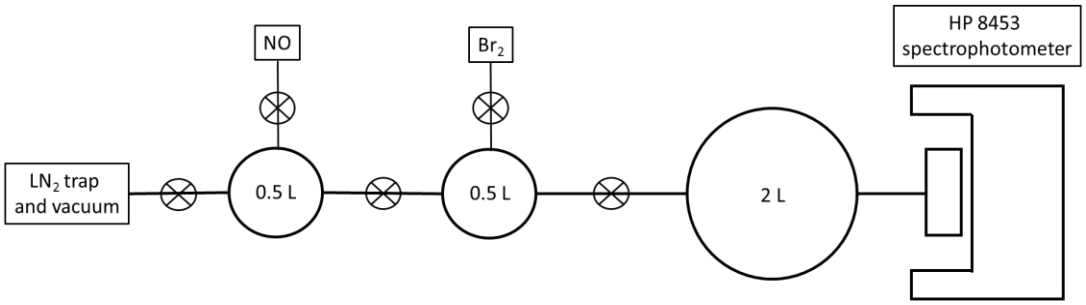

Figure 4.2.4 Experimental design for formation and expansion experiments.

III. Reactant Reservoir Preparations

To prepare the Br_2 reservoir, 20 mL of liquid Br_2 (Sigma Aldrich, 99.5+%) was placed in an Erlenmeyer beaker. The tip of a pre-evacuated 12-L gas bulb was placed in the flask and the bromine was transferred to the bulb under vacuum and allowed to vaporize. The filled 12 L bulb underwent several "freeze-pump-thaw" cycles to purify the bromine and rid the bulb of any air.

A 12 L bulb was filled with nitric oxide (Matheson, 99.5+%) and then connected to a silica gel (8 mesh) molecular sieve. Before filling a 0.5 L reaction vessel with NO, the NO was passed through the silica gel trap, submerged in an acetone/dry ice bath, in order to purify the NO of any oxidized impurities. This purification was performed for each formation trial.

IV. Experimental Procedure

In the preliminary laser photolysis runs, the laser tube was filled with the desired initial pressure of bromine. The desired initial pressure of nitric oxide was the added to the tube and the formation of BrNO was allowed to reach equilibrium. The 532 nm second harmonic of a Nd:YAG was then used to push the equilibrium back to the reactants. Once the laser was turned off, the return to equilibrium was monitored and recorded along with the temperature of the laser tube.

BrNO formation reactions were performed with approximate initial $P_{Br_2} : P_{NO}$ ratios of 1:1 or 1:2. For the formation trials, the first 0.5L reaction vessel was filled with the desired NO pressure, that upon release into the second 0.5L reaction vessel would provide an initial NO pressure nominally equal to or double the initial pressure of Br_2. The data collection using 100 torr pressure gauges, 3.39 Hz low pass filters, and an oscilloscope used to record reaction vessel pressure readings was started and the second 0.5L reaction vessel was filled with approximately the desired initial pressure of Br_2. The valve connecting the two vessels was quickly opened and closed, after which the remaining pressure of NO in the first vessel was recorded manually. The reaction was allowed to reach equilibrium and the final equilibrium pressure, along with the room

temperature, was recorded. The final equilibrium value was taken as the average of the 500 data points corresponding to the last 100 seconds.

In the expansion trials, the data collection was started before the valve connecting either the two 0.5L vessels (for 1:2 volume expansion) or the second 0.5L vessel and the 2L vessel (for 1:5 volume expansion) was opened. In these experiments, the valve was opened quickly and remained open. For 1:2 expansions, data was collected using the 100 torr pressure gauges attached to the reaction vessel and to the evacuated 0.5L vessel while for the 1:5 expansions, data was collected using the 100 torr pressure gauge connected to the reaction vessel and the 10 torr pressure gauge connected to the 2L vessel. The reaction was allowed to reach equilibrium after expansion and the room temperature and equilibrium pressure were recorded.

V. Safety Precautions

Liquid bromine is extremely toxic and can cause severe skin burns, eye damage, and can be fatal if inhaled. Extreme caution was used when handling liquid bromine and the 12L Br_2 reservoir was filled inside a safety hood with proper protective personal equipment (PPE). Colorless nitric oxide is a strong oxidizer, oxidizing to brown NO_2 and other N_xO_y species upon reaction with O_2. Nitric oxide is fatal when inhaled and can cause severe skin burns and eye damage upon contact. Nitric oxide should be kept away from all flammable material and extreme caution should be used when handling nitric oxide.

4.3 Results

I. Preliminary Laser Photolysis Experiments

Three preliminary laser photolysis trials were performed on equilibrium gas mixtures in the laser tube following BrNO formation trials. Figure 4.3.1 shows the total pressure as a function of time from a laser photolysis trial following a formation reaction with initial bromine and nitric oxide pressures of 8.40 and 15.98 torr at a temperature of 294.4K.

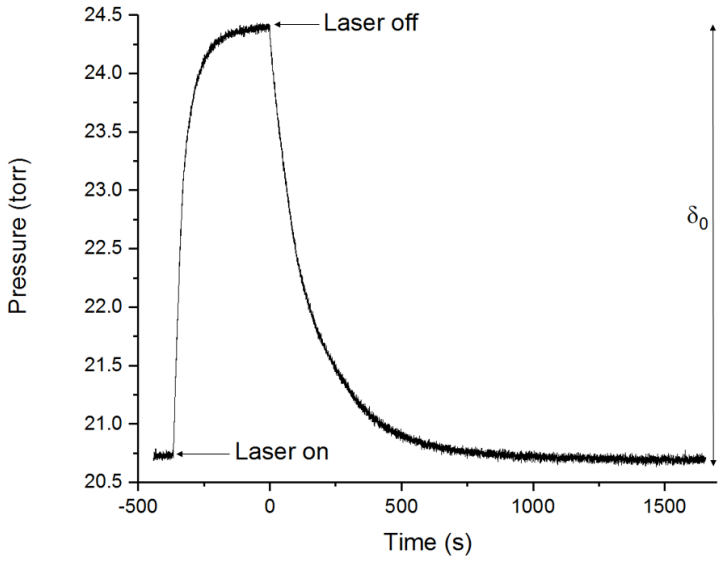

Figure 4.3.1 Laser photolysis of the equilibrium gas mixture following the formation of BrNO from 8.40 torr of Br_2 and 15.98 torr of NO. The equilibrium pressure was 20.72 torr.

For the laser photolysis trials, δ_0 was defined as the difference between the total pressure when the laser was turned off (t=0) and the total pressure at equilibrium. The integrated $g(\delta_f)$ solution in Eqn. (17) was then applied to the data to determine k_f, k_r, and K_{eq}. Figure 4.3.2 shows the integrated $g(\delta_f)$ solution in Eqn. (21) plot for the above photolysis trial.

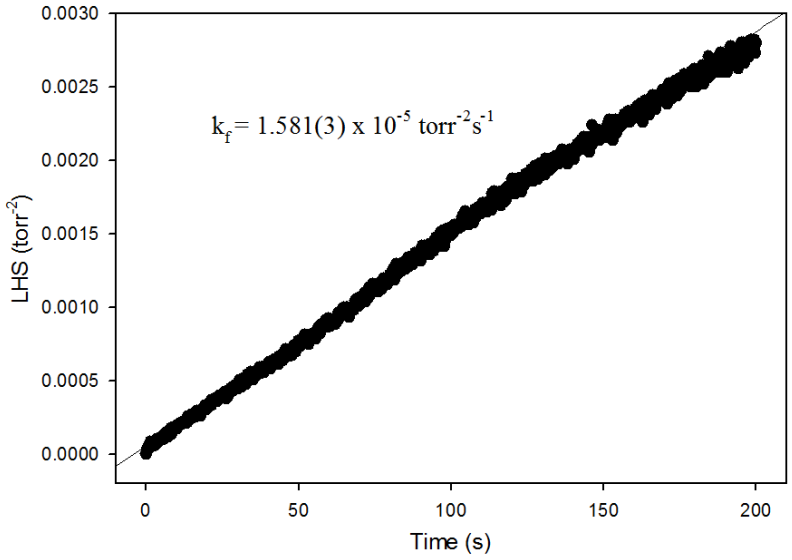

Figure 4.3.2 Integrated solution plot for the laser photolysis of the equilibrium gas mixture following the formation of BrNO from 8.40 torr of Br_2 and 15.98 torr of NO.

Table 4.3.1 shows the determined parameters from the three preliminary laser photolysis trails.

Table 4.3.1 Determined rate coefficients and equilibrium constant from the three preliminary laser photolysis trials.

$P_{Br2,0}$ (torr)	$P_{NO,0}$ (torr)	k_f (10^{-5} $torr^{-2}s^{-1}$)	K_{eq} ($torr^{-1}$)	k_r (10^{-5} $torr^{-1}s^{-1}$)	T (K)
8.40	15.98	1.581(3)	0.124	10.17(2)	294.4
20.23	41.47	1.781(5)	0.281	6.34(2)	294.7
21.09	43.41	1.271(6)	0.172	7.40(3)	295.4

While these results demonstrate the feasibility of the photolysis perturbation method, the poor reproducibility evidenced in Table 4.3.1 led to the suspicion that when nitric oxide was added to the tube, the bromine was pushed down to the far end of the tube, making uniform mixing difficult. After these preliminary laser photolysis results, it was decided to conduct all formation reactions in spherical reaction vessels to ensure proper mixing of the reactants. Future photolysis perturbation reactions should prepare equilibrium gas mixtures of known composition, which will be expanded into the laser tube and allowed to reach a new equilibrium (after expansion) before beginning photolysis perturbation observations.

II. BrNO Formation

Figure 4.3.3 shows the total pressure as a function of time from one of the formation trials in the apparatus of Figure 4.2.4 at a temperature of 294.9K. The data collection was initially started before the addition of Br_2 to the second reaction volume and upon addition of Br_2, the valve connecting the two reaction vessels was quickly opened and closed to allow the desired concentration of NO to react with the initial pressure of Br_2.

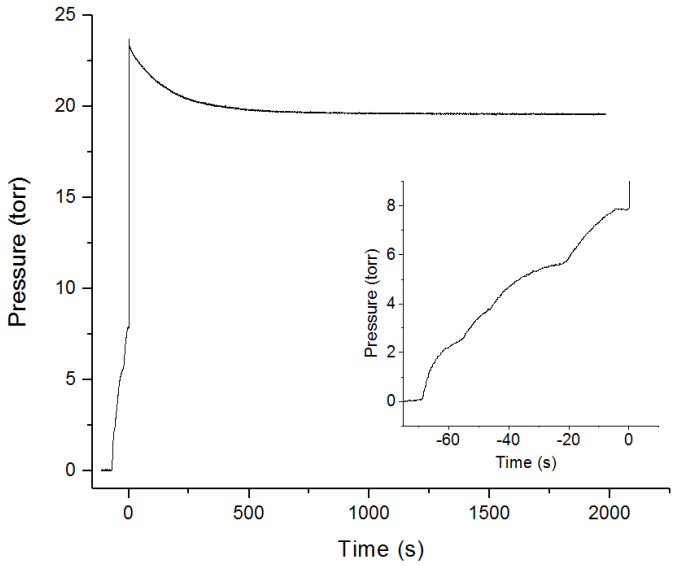

Figure 4.3.3 Formation trial using $P_{Br2,0}$ = 8.03 torr and $P_{NO,0}$ = 15.38 torr. Early times at which bromine and nitric oxide were added are shown in the inset.

The initial pressure of NO was determined from the product of the difference in NO pressure in the first vessel and the volume ratio of the first vessel and the reaction vessel.

$$P_{NO,0} = \frac{\Delta P_{NO} V_1}{V_2} \tag{47}$$

The total pressure was determined by extrapolating the experimental pressure back to t=0, the last pressure value corresponding to the initial bromine pressure before the addition of nitric oxide. It was also considered to use the pressure value at the halfway point between the initial pressure and the maximum increase in pressure but the differences between these two total pressure values was negligible (less than 20 millitorr) so the time point before the addition of nitric oxide was used at t=0.Upon the initial opening and closing of the value between the reaction vessels containing NO and Br_2, a sharp initial increase of pressure was observed. The extrapolation back to t=0 ignored this

overshoot and fitted a linear or low-order polynomial function to the data after the overshoot to determine the total pressure. The initial pressure of Br_2 was then calculated from the difference of extrapolated total pressure and the initial NO pressure.

$$P_{Br_2,0} = P_{T,0} - P_{NO,0} \tag{48}$$

Figure 4.3.4 shows an example of the total pressure extrapolation for a $P_{Br2,0}$ = 8.03 torr and $P_{NO,0}$ = 15.38 torr mix, as determined by the method described, with the extrapolated pressure at t=0 marked with a cross.

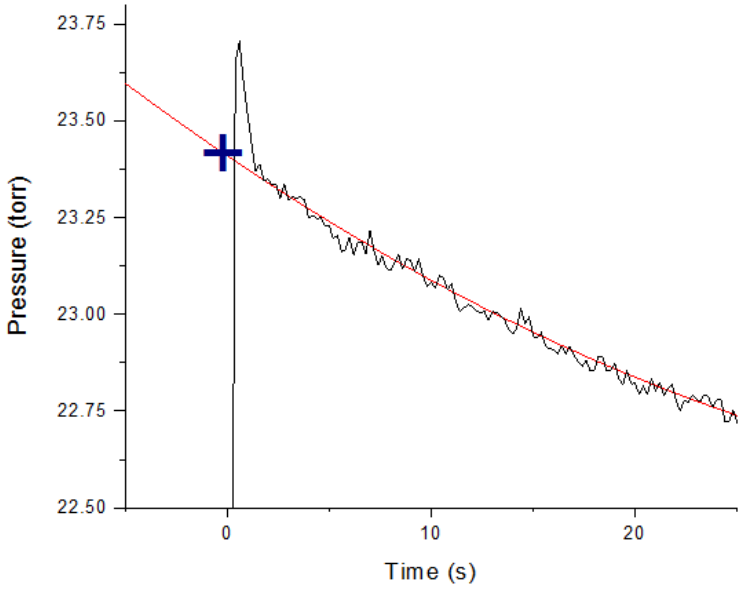

Figure 4.3.4 Experimental pressure with extrapolation fit used to determine P_T at t=0. The overshoot in pressure immediately after t =0 was not used in the extrapolation fit. Presumably this results from the initial gas rush into the reaction vessel.

The integrated $g(\delta_f)$ solution in Eqn. (17) and the integrated third-order solution in Eqn. (43) were both applied to each formation trial to determine k_f, k_r, and K_{eq}. Figures 4.3.5 and 4.3.6 show plots of the LHS vs. time of the integrated $g(\delta_f)$ solution and the

integrated third order rate equation analysis, respectively, from the formation trial shown in Figure 4.3.3 at a temperature of 294.9K.

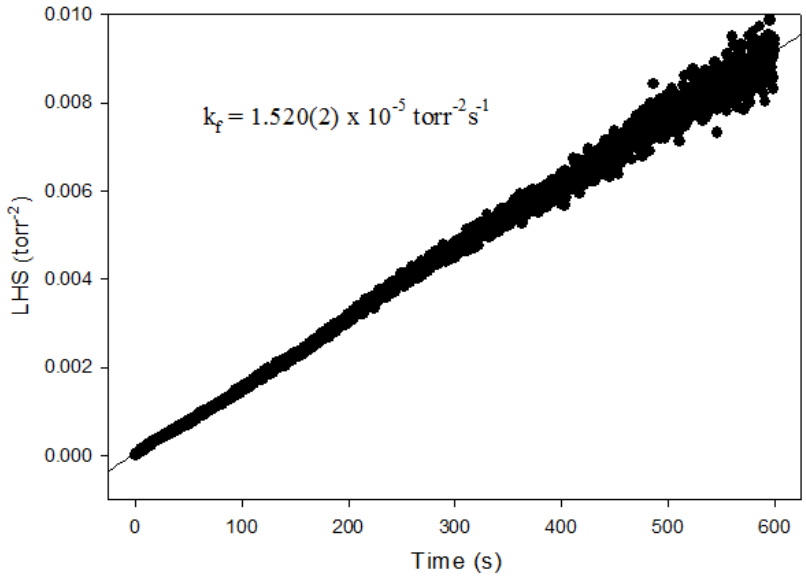

Figure 4.3.5 Integrated $g(\delta_f)$ solution for formation of BrNO from $P_{Br2,0}$ = 8.03 torr and $P_{NO,0}$ = 15.38 torr.

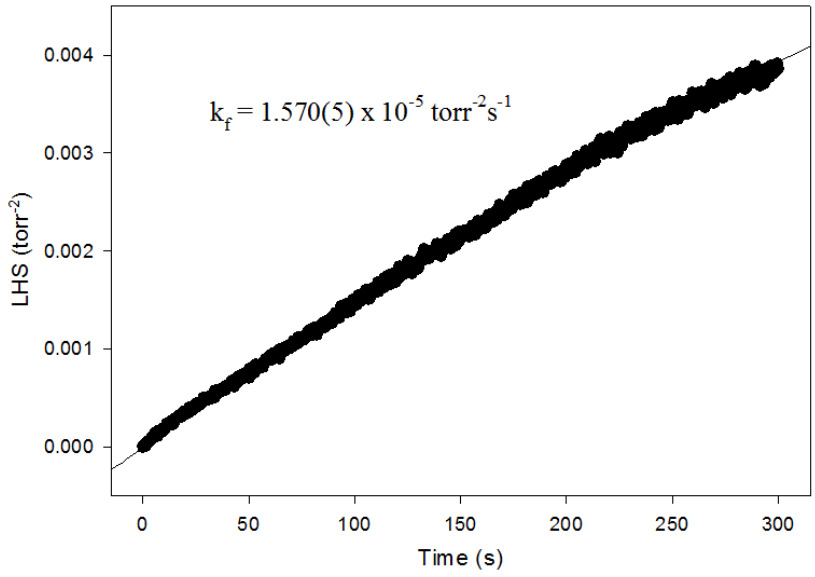

Figure 4.3.6 Third-order integrated rate solution plot for formation of BrNO from $P_{Br2,0}$ = 8.03 torr and $P_{NO,0}$ = 15.38 torr.

In the case of the integrated $g(\delta_f)$ solution, the error in the slope determined by a least-squares fitting was attributed as the error in k_f and the relative error in k_f was taken as the relative error in k_r. For Benson's method, the limiting slope was used to determine k_f, as Benson's solution only holds at early times when the reverse rate is negligible. The error in the limiting slope was used for the error in k_f and the relative error in k_f was used for the relative error in k_r. The error for individual K_{eq} measurements was propagated using the relative error in the pressure gauges and the noise level in the equilibrium pressure and was determined to be less than 0.5% (1×10^{-3} torr^{-1}). Taking the temperature fluctuations over the course of an experiment to be ±1K propagates to an uncertainty in K_{eq} of ±0.002 torr^{-1}. The observed range of experimental K_{eq} values determined in this work is much larger than either of these estimated uncertainties. Accordingly, a K_{eq} value is reported with its standard deviation about the mean.

Table 4.3.2 Determined values of k_f, k_r, and K_{eq} from the formation trials along with average values and their standard deviations.

$P_{Br2,0}$ (torr)	$P_{NO,0}$ (torr)	Integrated $g(\delta_f)$ Solution		Integrated Third-Order Solution		K_{eq} ($torr^{-1}$)	T (K)
		k_f (10^{-5} $torr^{-2}s^{-1}$)	k_r (10^{-5} $torr^{-1}s^{-1}$)	k_f (10^{-5} $torr^{-2}s^{-1}$)	k_r (10^{-5} $torr^{-1}s^{-1}$)		
8.03	15.38	1.520(2)	6.531(8)	1.570(5)	6.746(22)	0.233	294.9
8.07	15.51	1.473(2)	6.458(2)	1.532(4)	6.719(18)	0.228	294.8
7.91	15.55	1.466(2)	7.294(9)	1.488(8)	7.402(39)	0.201	294.7
12.36	18.06	1.429(3)	6.052(11)	1.524(11)	6.453(48)	0.236	295.0
10.13	19.08	1.570(2)	6.299(9)	1.560(5)	6.261(22)	0.249	296.4
10.07	9.73	1.510(3)	5.405(10)	1.652(6)	5.913(22)	0.279	295.1
7.99	15.46	1.512(2)	7.115(9)	1.597(5)	7.514(24)	0.213	295.2
10.06	9.60	1.472(2)	5.743(7)	1.624(9)	6.337(34)	0.256	295.1
10.17	19.06	1.372(5)	5.476(2)	1.491(11)	5.950(44)	0.250	295.5
10.02	9.65	1.491(4)	5.488(13)	1.563(5)	5.753(17)	0.272	294.6
8.01	15.47	1.499(7)	6.384(28)	1.577(14)	6.717(53)	0.235	295.1
10.00	9.70	1.443(7)	5.674(26)	1.481(12)	5.824(49)	0.255	295.3
9.91	19.28	1.435(2)	5.707(8)	1.520(6)	6.048(25)	0.251	295.3
7.86	15.51	1.533(3)	6.111(12)	1.618(6)	6.448(23)	0.251	295.1
9.99	9.62	1.467(5)	5.451(24)	1.489(13)	5.532(48)	0.269	295.2
10.05	19.15	1.441(2)	6.137(8)	1.509(6)	6.426(24)	0.235	295.1
average		1.48(5)	6.2(8)	1.55(5)	6.4(6)	0.25(3)	295.2(4)

III. Perturbation of Equilibrium Br_2/NO/BrNO Mixtures by Expansion

For the expansion trials, it was ensured that the chemical system reached equilibrium before the end of the data collection. Some trials were rejected when it was determined that the system had not reach equilibrium by the end of the trial observations as the observed total pressure was still increasing. Data for expansions trials were taken from two pressure gauge readings, one from the initial reaction vessel and the other from the second reaction vessel. In the case of 1:2 ratio volume expansions, pressure readings

were taken from two 100 torr pressure gauges connected to the two 0.5L reaction vessels. For 1:5 ratio volume expansions, pressure readings from taken from a 100 torr pressure gauge connected to the initial 0.5L reaction vessel and a 10 torr gauge connected the 2L reaction vessel, into which the chemical system was expanded.

Because the formation of BrNO from reactants Br_2 and NO results in an equilibrium and the relaxation experiments perturb this (first) equilibrium such that system finds a new (second) equilibrium, we must be clear whether we refer to the first (e1) or the second (e2) equilibrium and whether we refer to the t=0 of the formation reaction or to t=0 of the perturbation, which begins the approach to the second equilibrium. Figure 4.3.7 shows a 1:5 ratio volume expansion of a gas mixture at a new equilibrium pressure of $P_{T,e1}$ = 19.27 torr taken with a 100 torr gauge reading from the initial 0.5L reaction vessel.

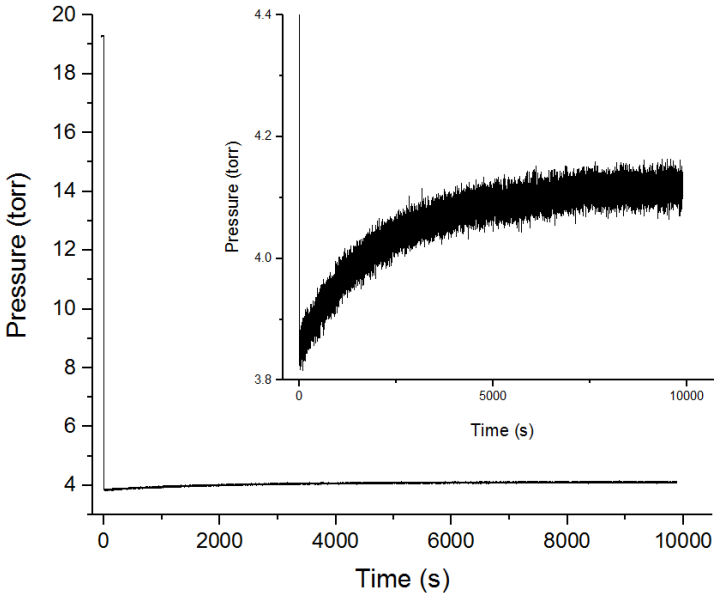

Figure 4.3.7 Total pressure in the reaction vessel during a volume expansion of a gas mixture at a first equilibrium pressure of $P_{T,e1}$ = 19.27 torr. The t=0 point here is the moment of valve opening, which begins the approach to the new (second) equilibrium.

Data was taken in the same expansion trial from a 10 torr gauge connected to the 2L reaction vessel and is presented in Figure 4.3.8.

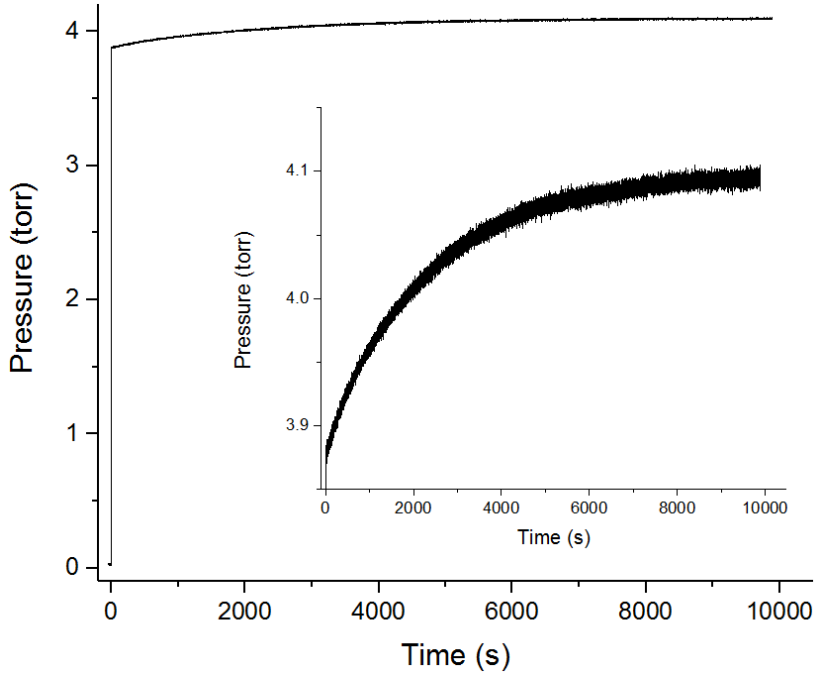

Figure 4.3.8 Total pressure in the second (2L) vessel during the volume expansion of **Figure 4.3.7**. After expansion, this gas mixture reaches a new equilibrium pressure of $P_{T,e2}$ = 4.10 torr. The t=0 point of the plot is as described in the caption of **Figure 4.3.7**.

As can be seen from the above figures, the pressure readings from the 10 torr gauge have substantially less noise than those from the 100 torr pressure gauge, and using data from the 10 torr gauge for kinetic parameter determination is preferable. Due to the noise level on the 100 pressure gauges, most expansion trials were executed with 1:5 volume ratios. Except for the noise level on the pressure gauges, there was no distinct difference between the rate coefficients determined from the 1:2 volume expansions than those determined from the 1:5 volume expansions. The surface-to-volume (SVR) ratio of a sphere is $SVR=(3r)^{-1}$, and in the 1:2 expansions (gases in one 0.5L vessel expanded into a

second 0.5L vessel) there is no change in the SVR upon expansion. In the 1:5 expansions (gases in one 0.5L vessel expanded into a second 2.0L vessel), the SVR decreases to 70% of its initial value in the 0.5L vessel as the total 2.5L volume becomes available upon expansion. That there is no discernable difference between k_f results in the two expansion ratios suggests that there is no significant heterogenous contribution to experimental observations and that this reaction is predominantly a homogeneous gas phase reaction.

The first equilibrium pressure before the volume expansion was determined by taking the total pressure at t=0 from the 100 torr gauge on the 0.5L reaction. To determine the t=0 pressure of the volume expansion, $P_{T,0}$, the P_T data from the gauge on the expansions volume was back extrapolated to t=0, again defining t=0 as the last point before the pressure drop in the reaction vessel and the last point before the pressure rise in the expansion vessel. For the 1:2 expansions, all data were collected from the 100 torr gauge on the reaction vessel. For the 1:5 volume expansions, the data from the 100 torr gauge on the 0.5L reaction vessel was used to determine $P_{T,e1}$ while data from the 10 torr gauge was used for post $P_T(t)$ values leading finally to $P_{T,e2}$. Figure 4.3.9 shows an extrapolation of post-expansion $P_T(t)$ with the extrapolated pressure at t=0 marked with a cross.

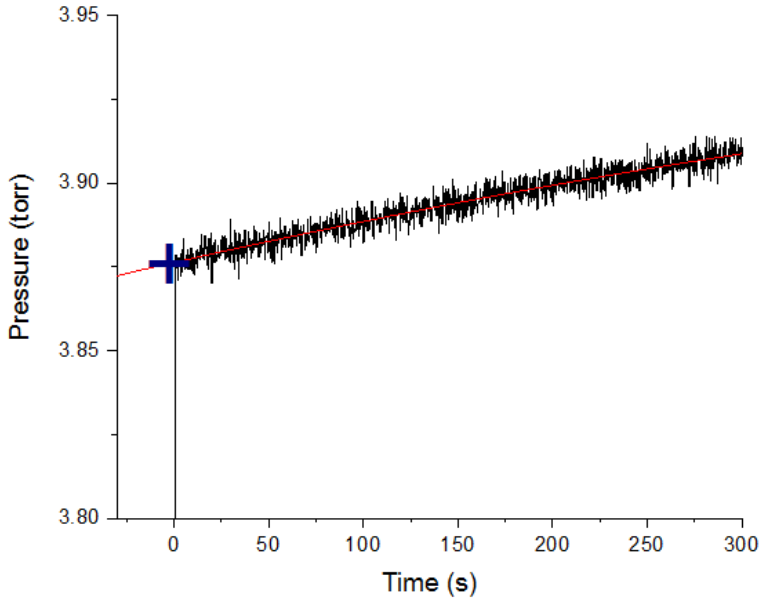

Figure 4.3.9 Extrapolation of post-expansion $P_T(t)$.

The integrated $g(\delta_e)$ solution was used with the post-expansion data to determine k_f taking the error in the slope to be the error in k_f and the relative error in k_f to be the relative error in k_r. Due to reduced noise in the 10 torr pressure gauge, the integrated $g(\delta_e)$ solution was able to be taken to longer times for the 1:5 volume expansions than for the 1:2 volume expansions and the formation trials.

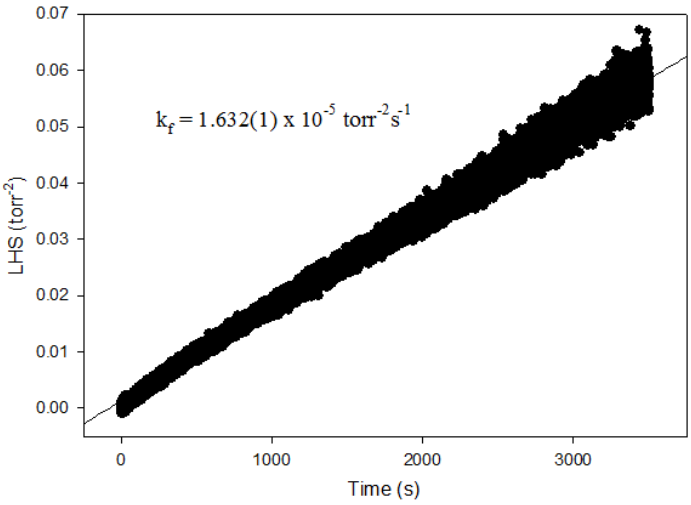

Figure 4.3.10 Integrated $g(\delta_e)$ solution for a 1:5 volume expansion for the expansion trials in **Figures 4.3.7-4.3.8**.

A second-order approximation was also used to approximate k_r using (46). The limiting slope was used to determine k_r and the error in k_r was determined to be the error of the slope for 1:2 expansions or the error in the slope divided by 1.6 for 1:5 expansions.

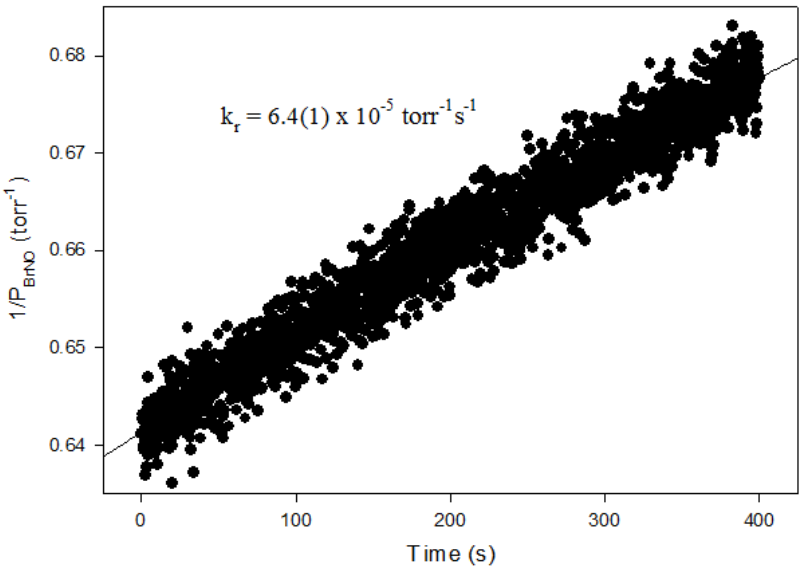

Figure 4.3.11 Second-order approximation of k_r plot from the expansion trail in **Figures 4.3.7-4.3.8**.

As with the formation trials, the uncertainty in K_{eq} individual values was of the order of ≈1%, whereas the standard deviation of 12 determinations were nearer to 11%.

Table 4.3.3 Determined values of k_f, k_r, and K_{eq} from expansion data using the integrated $g(\delta_e)$ solution and the 2nd-order approximation.

$P_{1,e}$ (torr)	P_2 (torr)	$P_{e,2}$ (torr)	Integrated $g(\delta_e)$ Solution		2nd-Order Approximation	K_{eq} ($torr^{-1}$)	T (K)
			k_f (10^{-5} $torr^{-2}s^{-1}$)	k_r (10^{-5} $torr^{-1}s^{-1}$)	k_r (10^{-5} $torr^{-1}s^{-1}$)		
19.39	9.65	9.93	1.798(11)	7.817(48)	8.4(3)	0.230	294.7
19.34	3.90	4.120	1.523(3)	6.610(12)	7.1(1)	0.230	295.4
25.21	5.042	5.325	1.647(2)	5.919(9)	6.9(2)	0.278	294.9
23.95	11.81	12.15	1.410(6)	5.623(25)	6.1(1)	0.251	295.4
16.77	3.347	3.542	1.708(1)	7.044(5)	9.1(1)	0.243	295.2
16.77	8.34	8.50	1.787(16)	6.163(56)	4.5(2)	0.290	295.3
23.78	4.733	5.041	1.814(1)	7.065(5)	7.1(4)	0.257	294.8
16.69	3.342	3.513	1.656(2)	5.723(7)	7.2(4)	0.289	295.1
23.95	4.775	5.058	1.477(1)	5.036(4)	6.1(2)	0.293	295.2
19.27	3.876	4.096	1.632(1)	5.296(3)	6.4(1)	0.308	295.5
16.71	3.332	3.505	1.827(1)	6.506(4)	7.8(1)	0.281	295.6
23.97	4.767	5.047	1.549(1)	5.570(5)	6.0(1)	0.278	295.5
average			1.7(1)	6.2(8)	7(1)	0.27(3)	295.2(3)

IV. Limitations of Solutions and Final Kinetic Parameter Values

For the expansions, the 2nd-order approximation was not very consistent in providing k_r estimates, resulting in standard deviations of ≈20% This method was only employed as an approximation and it should only be used as such.

Kintecus® was used to determined rate coefficients from both formation and expansion trials. However, our use of this program was beset with problems. We were never successful in any attempts to use the Levenberg-Marquardt fitting algorithm within the program. The fitting method "2.3" was used in Kintecus®, which employs a Powell

optimization algorithm [11] with an author-defined comparison operator [10]. It seemed to return reasonable k_f values, but often with unreasonably large uncertainties. Regardless of the input value of the fitted parameter k_r, Kintecus® would always return the provided input value of k_r as the fitted value. Even if the provided value of k_r was more than two standard deviations from the literature value, Kintecus® still would return the initial value of k_r as the determined value. Also, standard deviations for the parameters were not consistent or in some cases reasonable. Standard deviations were given for the parameters anywhere from over 1000% down to less than a percent and given standard deviations for rate coefficients of formation trials with similar starting pressures differed greatly. It was therefore decided that Kintecus® was not a reliable method in our hands to determine kinetic parameters and was abandoned.

Separate averages of determinations of rate coefficients from the integrated $g(\delta_f)$ and the integrated $g(\delta_e)$ solutions and the third-order integrated rate solution were taken as the final reported values, along with their standard deviations. Rate coefficients from the integrated $g(\delta_f)$ solution agreed with those determined from the third-order integrated rate solution within limits of one standard deviation. An average of K_{eq} values from formation and expansion data was calculated along with a standard deviation. These values, along with the average temperature, are reported in Table 4.3.4.

Table 4.3.4 Final k_f, k_r, and K_{eq} values determined from both formation and expansion data.

Integrated $g(\delta_f)$ Solution		Integrated $g(\delta_e)$ Solution		Integrated Third-Order Rate Equation		K_{eq} ($torr^{-1}$)	T (K)
k_f (10^{-5} $torr^{-2}s^{-1}$)	k_r (10^{-5} $torr^{-1}s^{-1}$)	k_f (10^{-5} $torr^{-2}s^{-1}$)	k_r (10^{-5} $torr^{-1}s^{-1}$)	k_f (10^{-5} $torr^{-2}s^{-1}$)	k_r (10^{-5} $torr^{-1}s^{-1}$)		
1.48(5)	6.1(6)	1.7(1)	6.2(8)	1.55(5)	6.4(6)	0.26(3)	295.2(4)

All the determined rate coefficients and equilibrium constants agree within error of the literature values, save Hisatune's k_r value, which are reported in Table 4.3.5. Disagreement with Hisatsune *et al.*[1]may be due to the higher temperature at which they conducted their experiment.

Table 4.3.5 Values of k_f, k_r, and K_{eq} from this work and the literature.

	k_f (10^{-5} $torr^{-2}s^{-1}$)	k_r (10^{-5} $torr^{-1}s^{-1}$)	K_{eq} ($torr^{-1}$)	T (K)
This Work: Integrated $g(\delta_f)$ Solution	1.48(5)	6.1(6)	0.26(3)	295.2(4)
This Work: Integrated $g(\delta_e)$ Solution	1.7(1)	6.2(8)		
This Work: Integrated Third-Order Rate Equation	1.55(5)	6.4(6)		
Mahoney[5]	1.6(2)	7(1)	0.23(2)	293(1)
Godfrey[4]	1.5(6)	7(2)	0.22(3)	293(1)
Hippler *et al.*[3]	1.8(1)	---	---	298
Houel *et al.*[2]	1.7(2)	8.5(2.7)	0.20(6)	303.0(5)
Hisatsune *et al.*[1]	1.4(1)	12.0	0.117	303

A weighted average of the twenty-eight integrated $g(\delta_f)$ and $g(\delta_e)$ k_f values was calculated to report a final k_f value of 1.5(6) x 10^{-5} $torr^{-2}s^{-1}$. With K_{eq} = 0.26(3) $torr^{-1}$, a final value of k_r = 5.8(8) x 10^{-5} $torr^{-1}s^{-1}$ is produced.

In conclusion, a room temperature investigation of the equilibrium kinetics of BrNO formation from Br_2 and NO has been conducted. Relaxation kinetic observations of total pressure were made following perturbation by expansion of and by photolysis of equilibrium gas mixtures. Analyses of these observations were made from linear plots of the integrated solution of the full rate equation where in partial pressures were stated relative to their final (post-perturbation) equilibrium values. Formation reactions, beginning only with Br_2 and NO, were analyzed also using the relaxation kinetics methodology and with a third-order integrated rate solution of the forward reaction, which was applied to the initial reaction rate. This study has shown that Espenson's claim that relaxation kinetics methodology can be applied to reactions that start fully on one side is valid. Stricter temperature control should be enforced to limit the temperature variance of the equilibrium constant.

4.4 References

1. Hisatsune, I. C.; Zafonte, L. A Kinetic Study of Some Third-Order Reactions of Nitric Oxide. *J. Phys. Chem.* **1969**, *73*, 2980.

2. Houel, N.; Van Den Bergh, H. BrNO-Thermodynamic Properties, the Ultraviolet/Vis Spectrum, and the Kinetics of Its Formation. *Int. J. Chem. Kinet.* **1977**, *9*, 867.

3. Hippler, H.; Luu, S. H.; Teitlerbaum, H.; Troe, J. Flash Photolysis Study of the NO-Catalyzed Recombination of Bromie Atoms. *Int. J. Chem. Kinet.* **1978**, *10*, 155.

4. Godfrey, P. Kinetics and Spectroscopy of BrNO, Air Force Institute of Technology, Wright Patterson Air Force Base, Ohio, 1997.

5. Mahoney, L. A. The Kinetics Following Photolysis of Nitrosyl Bromide, Air Force Institute of Technology, Wright Patterson Air Force Base, Ohio, 2004.

6. Espenson, J. H. Concentration-Jump Methods for Opposing Reactions. In *Chemical Kinetics and Reaction Mechanisms, Second Edition*; McGraw-Hill, Inc.: New York, 1995; pp 52.

7. Chase, M. W., Jr. NIST-JANAF Thermodynamic Tables, Fourth Edition. *J. Phys. Chem. Ref. Data*, *Monograph 9* **1998**, 1.

8. Silbey, R. J.; Alberty, R. A.; Bawendi, M. G. Effect of Temperature on the Equilibrium Constant. In *Physical Chemistry, 4th Edition* John Wiley & Sons, Inc.: 2005; pp 145.

9. Benson, S. W. Third-Order Reactions. In *The foundation of chemical kinetics* McGraw-Hill: New York, 1960; pp 21.

10. Ianni, J. C. A Comparison of the Bader-Deuflhard and the Cash-Karp Runge-Kutta Integrators for the GRI-MECH3.0 Model Base on the Chemical Kinetics Code Kintecus. In *Computational Fluid and Solid Mechanics*; Bathe, K. J., Ed.; Elsevier Science Ltd.: Oxford, 2003; pp 1369.

11. Vetterling, W. T.; Flannery, B. P.; Teukolsky, S. A.; Press, W. H. *Numerical Recipes in FORTRAN, Second Edition;* Cambridge University Press: Cambridge, 1992.